SCIENCE AND TECHNOLOGY OF ADVANCED MATERIALS
2025, VOL. 26, NO. 1, 2436347
https://doi.org/10.1080/14686996.2024.2436347

Taylor & Francis
Taylor & Francis Group

FOCUS ISSUE REVIEW

Integrating machine learning with advanced processing and characterization for polycrystalline materials: a methodology review and application to iron-based superconductors

Akiyasu Yamamoto [a,b], Akinori Yamanaka [b,c], Kazumasa Iida [b,d], Yusuke Shimada [b,e] and Satoshi Hata [b,e,f]

[a]Department of Applied Physics, Tokyo University of Agriculture and Technology, Tokyo, Japan;
[b]JST-CREST, Saitama, Japan;
[c]Department of Mechanical System Engineering, Tokyo University of Agriculture and Technology, Tokyo, Japan;
[d]College of Industrial Technology, Nihon University, Chiba, Japan;
[e]Department of Advanced Materials Science and Engineering, Kyushu University, Fukuoka, Japan;
[f]The Ultramicroscopy Research Center, Kyushu University, Fukuoka, Japan

ABSTRACT

In this review, we present a new set of machine learning-based materials research methodologies for polycrystalline materials developed through the Core Research for Evolutionary Science and Technology project of the Japan Science and Technology Agency. We focus on the constituents of polycrystalline materials (i.e. grains, grain boundaries [GBs], and microstructures) and summarize their various aspects (experimental synthesis, artificial single GBs, multiscale experimental data acquisition via electron microscopy, formation process modeling, property description modeling, 3D reconstruction, and data-driven design methods). Specifically, we discuss a mechanochemical process involving high-energy milling, in situ observation of microstructural formation using 3D scanning transmission electron microscopy, phase-field modeling coupled with Bayesian data assimilation, nano-orientation analysis via scanning precession electron diffraction, semantic segmentation using neural network models, and the Bayesian-optimization-based process design using BOXVIA software. As a proof of concept, a researcher- and data-driven process design methodology is applied to a polycrystalline iron-based superconductor to evaluate its bulk magnet properties. Finally, future challenges and prospects for data-driven material development and iron-based superconductors are discussed.

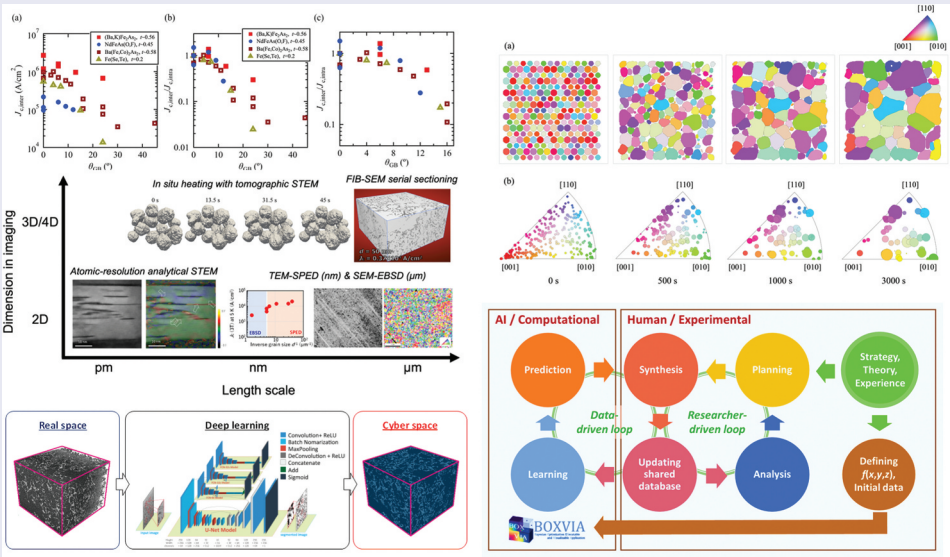

ARTICLE HISTORY
Received 21 August 2024
Revised 22 November 2024
Accepted 26 November 2024

KEYWORDS
Bayesian optimization; BOXVIA; data assimilation; data-driven process design; deep learning; DFT; electron microscopy; fully convolutional neural networks; grain boundaries; high-energy milling process; Iron-based superconductor; machine learning; magnet; multiscale observation; phase-field modeling; polycrystalline materials; processing; researcher-driven process design; scanning precession electron diffraction; superconductor; thin films; trapped field; 3D reconstruction; 4D STEM

IMPACT STATEMENT

We present a new set of machine learning-based materials research methodologies for polycrystalline materials, such as a mechanochemical process involving high-energy milling, in situ

CONTACT Akiyasu Yamamoto akiyasu@cc.tuat.ac.jp Department of Applied Physics, Tokyo University of Agriculture and Technology, Tokyo, Japan

observation of microstructural formation using 3D scanning transmission electron microscopy, phase-field modeling coupled with Bayesian data assimilation, nano-orientation analysis via scanning precession electron diffraction, semantic segmentation using neural network models, and the Bayesian-optimization-based process design using the BOXVIA software.

1. Introduction

In recent years, efforts have been made to improve the efficiency of material research, including by accelerating the search for optimal conditions for materials fabrication using machine learning methods [1–5] and high-throughput microstructure characterization using automated large-scale data acquisition systems [6–8]. The evolution of materials characterization techniques is related to the improved efficiency of material research. For example, the spatial resolution ranges covered by electron microscopy and X-ray microscopy have increased and overlapped, allowing researchers to choose an appropriate imaging method for their specific materials research problems [9–11]. In addition, the development of novel instruments that integrate different material characterization methods (e.g. a fully functional atom probe integrated in an aberration-corrected transmission electron microscope [12]) and the common formatting of microscopy and microanalysis data from various instruments are recent trends that will enhance materials research efficiency [6,13].

This study focuses on polycrystalline iron-based superconductors (IBSs) [14] as target materials and aims to establish an efficient research method to improve the superconducting properties and optimize the fabrication of IBSs. This efficient research method is called μ-Ex-datarial design, where μ stands for microstructural characterization and Ex means experimental material fabrication and property measurement. The term 'datarial design' refers to data-driven material design in which material fabrication is guided by computational analyses and simulations of material microstructures and properties using experimental data obtained through material fabrication and characterization (μ-Ex).

The experimental and computational components of the proposed method, μ-Ex-datarial design, should be optimized for target materials. We examined the selection of experimental and computational methods and their effective interconnection for polycrystalline IBSs. For microstructural characterization (μ), electron microscopy and laboratory-scale X-ray diffraction (XRD) were selected to characterize both local and average microstructures. Here, three-dimensional (3D) image data and in situ time-dependent imaging data were acquired via electron microscopy observation [15–17]. These microscopy image data can be directly incorporated into the modeling and simulation of microstructural evolutions and superconducting current flows (data assimilation), which can be as effective as virtual experiments [18]. The other featured experimental method (Ex) involves fabricating bicrystal thin films to examine their superconducting properties and microstructures [19]. This method is effective for observing microstructural components comprising polycrystalline microstructures, such as grain boundaries (GBs), and evaluating their effects on superconducting properties. Through the close interplay of microstructural characterization, experimentation, and modeling, the μ-Ex-datarial design approach has been used to fabricate a world-class high-performance polycrystalline IBS magnet [20]. The following sections detail μ-Ex-datarial design and its application to IBSs.

The contents of this paper are briefly described as follows. Section 2 reviews the fabrication methods of various types of IBSs and the notable properties of the fabricated materials with three types of sample forms, i.e. single crystal thin films, bicrystal thin films, and polycrystalline bulks. Section 3 describes the multiscale and multidimensional electron microscopy imaging platform for the present study. Section 4 describes the computational methods for realizing the modeling of microstructures and material properties of IBSs. Specifically, we describe the following: 3D microstructures of Ba122 bulk analyzed using deep learning and their linkage to superconducting properties; phase field (PF) modeling and data assimilation to reproduce an experimentally observed sintering process of metal nanoparticles; and another PF modeling approach to a polycrystalline structure formation process using first-principles calculations based on the density functional theory (DFT). Section 5 introduces BOXVIA, a Bayesian optimization software developed for data-driven material processing design. Section 6 describes the properties of a Ba122 bulk superconducting magnet fabricated by utilizing all the knowledge about the IBSs and their processing and the characterization methods presented in Sections 2 to 5. Section 7 summarizes the results of the present study and discusses the remaining challenges and prospects.

2. Advanced processing

2.1. Introduction to processing of iron-based superconducting materials

Microstructures, such as grains, grain orientations, and defects, strongly influence the transport properties of

superconducting materials. In general, a microstructure should be carefully optimized for the transport of superconducting currents and flux pinning to exploit the performance of superconducting materials. For example, cuprate high-temperature superconductors, such as $REBa_2Cu_3O_{7-\delta}$ (REBCO, where RE means a rare earth metal), have the weak-link problem, where the transport of superconducting currents is suppressed at GBs, depending on the misorientation angle between neighboring grains [21]. A coated conductor with a biaxially aligned REBCO thin film on a textured substrate has been developed for wire applications to overcome the weak-link problem [22–30]. For $Bi_2Sr_2CaCu_2O_{8+\delta}$ and $Bi_2Sr_2Ca_2Cu_3O_{10+}$, the powder-in-tube (PIT) process has been combined with high-pressure sintering to obtain *c*-axis-aligned wires and tapes [31–48]. For bulk materials, a melt-growth process has been developed to grow single-domain bulks using a seed crystal as a nucleus [49–53]. For quasi-single-crystal materials, nanoprecipitates and artificial pinning centers have been introduced to improve the pinning efficiency of quantized magnetic fluxes. In Nb-Ti wires, the flux pinning strength has been greatly enhanced by generating nanometer-scale nonsuperconducting precipitates through cold working, taking advantage of the long coherence length and workability of the alloy [54,55].

IBSs exhibit high-temperature superconductivity in layered compounds with a square lattice of iron, showing a superconducting transition temperature (T_c) of up to 56 K [56]. Representative parent compounds include the 1111 (REFeAsO) [56], 122 ($AEFe_2As_2$, where AE means an alkaline earth metal) [57], 11 (FeSe) [58] and 1144 ($AEAFe_2As_2$, where A means an alkaline metal) [59] phases. With the recent discovery of topological superconductivity, the potential applications of IBSs include Majorana platforms, Josephson devices, and powerful magnets [14,60]. The high upper critical field (H_{c2}) of more than 100 T [61] in 1111 systems and more than 50 T [62–65] in 122 systems with small electromagnetic anisotropy is attracting attention in terms of high-magnetic-field applications. This has enhanced research on wires, tapes, and bulk conductors as materials for high-field magnets [14,66,67]. The advantage of IBSs in terms of conductors is that the weak-link problem at GBs is less pronounced than that in cuprates [68,69]. Katase *et al.* reported that Co-doped Ba122 bicrystalline thin films fabricated via pulsed laser deposition (PLD) showed no transport intergrain critical-current-density decay up to a misorientation angle of 5°–9°, which is larger than the critical angle of 2°–3° for REBCO [69]. Thus, high critical currents are anticipated in IBSs in the form of polycrystalline materials without needing a high degree of texturing as in cuprates. Two approaches have been considered for fabricating IBSs.

- *Toward perfect crystals*: improving the degree of crystalline orientation (as in cuprates) and including biaxially oriented 11-phase coated conductors [70–72] and uniaxially oriented 122-phase flat tapes [73–78]
- *Toward random polycrystals*: not intentionally pursuing texturing, and including 122- and 1144-phase randomly oriented bulk materials [79,80] and PIT-processed 122-phase round wires [81–84]

Higher critical current density (J_c) can be easily obtained through the former, though coated conductors are technologically more complex and expensive to realize, but the latter can more easily produce larger bulks and longer wires. The latter approach differs from that for cuprates and workable metallic superconductors and is similar to the synthesis method of intermetallic, weak-link-free MgB_2 superconductors [85,86].

Single-crystal and bicrystalline thin-film processing are reviewed in Sections 2.2 and 2.3, respectively. Subsequently, advanced processes for polycrystalline materials, which fall under the latter approach, are reviewed in Section 2.4.

2.2. Thin-film growth

We have focused on three main classes of IBSs, namely, NdFeAs(O,F), NdFeAs(O,H), $(Ba,K)Fe_2As_2$, and Fe(Se,Te), which are potential materials for conductor applications. NdFeAs(O,F), NdFeAs(O,H), and $(Ba,K)Fe_2As_2$ were fabricated using molecular-beam epitaxy (MBE), whereas Fe(Se,Te) was grown using PLD. Each compound poses challenges in growing epitaxial thin films with high crystalline quality. Furthermore, selecting suitable substrates is difficult, as commercially available bicrystal substrates are limited to $SrTiO_3$, $(LaAlO_3)_{0.3}(Sr_2TaAlO_6)_{0.7}$, and MgO. Nonetheless, epitaxial thin films have been grown on these substrates, enabling bicrystal experiments. This section concisely describes the deposition techniques for each compound on standard substrates.

2.2.1. NdFeAs(O,F) and NdFeAs(O,H)

For both NdFeAs(O,F) and NdFeAs(O,H), one-step fluorination and hydrogenation during film growth are challenging. Therefore, a two-step process is used: the parent compound, NdFeAsO, is prepared on MgO(001) via MBE [87], and topotactic chemical reactions are induced to substitute O partially with F or H [88–90]. Despite a substantial in-plane lattice mismatch of ~ 6% between NdFeAsO and MgO at room temperature, the 003 rocking curve and the ϕ scan of the 200 reflection show a sharp full width at half maximum of 0.6°–0.8°. These values remain unchanged after fluorination or hydrogenation [90]. Misfit dislocations even compensate for the large mismatch [91]. The epitaxial relationship is (001)[100] NdFeAs(O, F or H)||(001)[100]MgO. Although the

superconducting transition temperatures (T_c) of both compounds are nearly identical (~50 K), NdFeAs(O, H) exhibits a lower electromagnetic anisotropy (~3.2) and a high critical current density (J_c) of ~17 MA/cm^2 at 4 K in a zero magnetic field [90], compared to NdFeAs(O,F), which has an anisotropy of ~ 5 and a self-field J_c of ~7.6 MA/cm^2 at 4.2 K [92]. Note that NdFeAs(O,H) exhibits the highest values among IBS thin films. This low anisotropy is mainly due to the more 3D Fermi surface resulting from H doping [93], and the high J_c is from an increase in condensation energy [90,91,94].

2.2.2. (Ba,K)Fe_2As_2

Unlike epitaxial thin films of Ba(Fe,Co)$_2$As$_2$ and BaFe$_2$(As,P)$_2$, those of (Ba,K)Fe_2As_2 have not been successfully produced using PLD due to difficulties in controlling the volatile potassium (K). This challenge is similar to that encountered with $CaFe_2As_2$, where calcium (Ca) exhibits high vapor pressures [95]. For compounds containing volatile elements, MBE is effective for realizing epitaxial thin films. In particular, epitaxial (Ba,K)Fe_2As_2 thin films [(001)[110](Ba,K)Fe_2As_2||(001)[100]CaF_2] with a high self-field critical current density (J_c) of ~14 MA/cm^2 at 4 K have been achieved at low-growth temperatures using fluoride substrates [96,97]. Microstructural analyses conducted via transmission electron microscopy (TEM) revealed that columnar grains, which grow nearly perpendicular to the substrate, formed a slightly misoriented, anisotropic thin-film microstructure. The small inclined GBs created in this manner act as strong pinning centers, leading to a higher flux pinning force density (~200 GN/m^3 at 4 K and 6 T) compared with that in heavy ion-irradiated (Ba,K)Fe_2As_2 single crystals below 5 T [98].

Although epitaxial (Ba,K)Fe_2As_2 thin films with good superconducting properties have been achieved, they require fluoride substrates, which are not commercially available as bicrystal substrates. Thin films must be grown on oxide substrates to create well-defined artificial single GBs in (Ba,K)Fe_2As_2. However, the epitaxial growth of (Ba,K)Fe_2As_2 on oxide substrates poses challenges [94]. Thus, we utilized the parent compound, $BaFe_2As_2$, as a buffer layer [99], which is chemically and structurally compatible with (Ba,K)Fe_2As_2. The resultant (Ba,K)Fe_2As_2 film grown on a $BaFe_2As_2$-buffered MgO substrate exhibited a relatively high T_c of 39.8 K, likely due to epitaxial strain [99]. Structural analysis via XRD and TEM confirmed the orientation (001)[100](Ba,K)Fe_2As_2||(001)[100]$BaFe_2As_2$||(001)[100]MgO. Due to the similarity of its microstructure to that of (Ba,K)Fe_2As_2 grown on CaF_2, the field dependence of the J_c characteristics of (Ba,K)Fe_2As_2/$BaFe_2As_2$-buffered MgO mirrors that of (Ba,K)Fe_2As_2/CaF_2.

2.2.3. Fe(Se,Te)

Similar to (Ba,K)Fe_2As_2, Fe(Se,Te) has been successfully grown on CeO_2-buffered $SrTiO_3$. The crystal structure of CeO_2 is of a fluorite-type akin to CaF_2, making it an effective template for various IBSs, such as Fe(Se,Te) [100]; $BaFe_2As_2$ [101]; and *Ln*FeAs(O,F), where *Ln* includes Nd [102] and Sm [103]. Notably, $FeSe_{0.5}Te_{0.5}$ grown on CeO_2-buffered Y-stabilized ZrO_2 and $SrTiO_3$ exhibited a T_c of ~ 20 K [104,105]. Fe(Se,Te) is primarily grown using PLD. We also synthesized $FeSe_{0.5}Te_{0.5}$ thin films on CeO_2-buffered $SrTiO_3$(001) through PLD. $FeSe_{0.5}Te_{0.5}$ represents the nominal composition of the PLD target, which was prepared through ball milling [106] and then spark plasma sintering (SPS) [79].

Our $FeSe_{0.5}Te_{0.5}$ samples contained excess iron, which led to charge carrier localization and thus a lower T_c. To mitigate this issue, we annealed $FeSe_{0.5}Te_{0.5}$ at 200°C at an oxygen partial pressure (p_{O2}) of 1 Pa for 10 min. This post-annealing process proved highly effective in removing the excess iron [107]. Structural analysis via XRD confirmed that $FeSe_{0.5}Te_{0.5}$ was grown epitaxially with the orientation relationship (001)[100]$FeSe_{0.5}Te_{0.5}$||(001)[110]CeO_2||(001)[100]$SrTiO_3$. A self-field J_c of ~ 1.7×10^5 A/cm^2 was recorded at 4 K.

2.3. Bicrystal experiments

To date, IBSs have only been studied at [001]-tilt GBs. Considering polycrystalline applications, GBs other than [001]-tilt GBs should be fabricated and investigated. Therefore, [010]-tilt roof-type GBs of Fe(Se,Te) and K-doped Ba122 were fabricated as well.

To conduct bicrystal experiments, we fabricated epitaxial thin films of NdFeAs(O,F), (Ba,K)Fe_2As_2, and $FeSe_{0.5}Te_{0.5}$ on bicrystal substrates. For NdFeAs(O,F) and (Ba,K)Fe_2As_2, [001]-tilt symmetric MgO substrates were used, whereas [010]-tilt roof-type symmetric $SrTiO_3$ substrates were selected for $FeSe_{0.5}Te_{0.5}$. The growth conditions except the fluorination temperature were consistent with those described in Section 2.2. The fluorination temperature was reduced by 100°C due to the tendency of fluorine to diffuse preferentially along the GB, eroding both the superconducting NdFeAs(O,F) layer and the MgO substrate [108]. Further information about GBs in IBSs are available in several review articles [109–111].

2.3.1. [001]-tilt symmetric bicrystal NdFeAs(O,F) and (Ba,K)Fe_2As_2

Figure 1a summarizes the misorientation angle (θ_{GB}) dependence of the intergrain J_c of NdFeAs(O,F) and (Ba,K)Fe_2As_2. The measured temperatures for NdFeAs(O,F) and (Ba,K)Fe_2As_2 were 20.2 K ($t \approx T/T_{c,onset} \approx 0.45$) [108] and 20 K ($t \approx$ ~ 0.56), respectively [19]. For comparison, the data for Ba(Fe,Co)$_2$As$_2$ at 12

K ($t \approx 0.58$) [69] and Fe(Se,Te) at 4 K ($t \approx 0.2$) [112] are superimposed. The intergrain and intragrain J_c of (Ba,K)Fe_2As_2 were the highest among the various IBSs. Additionally, the decay of intergrain J_c against the misorientation angle was not significant among the IBSs.

Figure 1b,c shows the ratio of the intergrain J_c to the intragrain J_c ($J_{c,inter}/J_{c,intra}$) as a function of θ_{GB}. The intergrain J_c started to decrease exponentially at approximately 8°–9°. This characteristic angle is the critical angle, θ_c. For (Ba,K)Fe_2As_2, θ_c is constant regardless of the applied magnetic field (Figure 1d), whereas the θ_c of Ba(Fe,Co)$_2As_2$ was reduced by the applied magnetic field.

The superior GB characteristics of (Ba,K)Fe_2As_2 were not due to the measurement temperature, as the reduced temperature of (Ba,K)Fe_2As_2 and Ba(Fe,Co)$_2As_2$ was higher than those of NdFeAs(O,F) and Fe(Se,Te). (Ba,K)Fe_2As_2 possessed the highest depairing current density among the IBSs. Additionally, microstructural analyses revealed that the misorientation angle changed gradually within a 20 nm region to reach the nominal GB angle [19]. These two factors are reflected in Figures 1a,d, which indicate that the GB properties of (Ba,K)Fe_2As_2 were superior to those of the other IBSs. Therefore, from section 2.4 onwards, we focus on Ba122 rather than other IBSs.

2.3.2. [010]-tilt symmetric bicrystal $FeSe_{0.5}Te_{0.5}$

Bicrystal experiments using IBSs have been conducted using [001]-tilt symmetric bicrystalline substrates. Because polycrystalline samples contain many types of GBs, how the intergrain J_c is affected by GBs other than [001]-tilt GBs should be studied. Therefore, we explored the structural and superconducting properties of $FeSe_{0.5}Te_{0.5}$ [010]-tilt bicrystal films.

Structural analyses revealed that the GB angles of $FeSe_{0.5}Te_{0.5}$ (θ_{GB}^{FST}) grown on a $SrTiO_3$ bicrystal substrate with GB angles (θ_{GB}^{STO}) of 8° and 12° were smaller than the nominal values. On the contrary, the GB angle of the CeO_2 buffer layer (θ_{GB}^{CeO2}) was always larger than θ_{GB}^{STO}. These observations could be explained by the geometrical coherence model developed by Budai *et al* [114]. For $\theta_{GB}^{STO} \geq 24°$, no GBs formed in $FeSe_{0.5}Te_{0.5}$, whereas $\sum^{9}[110]/(221)2$ GBs formed in the CeO_2 buffer

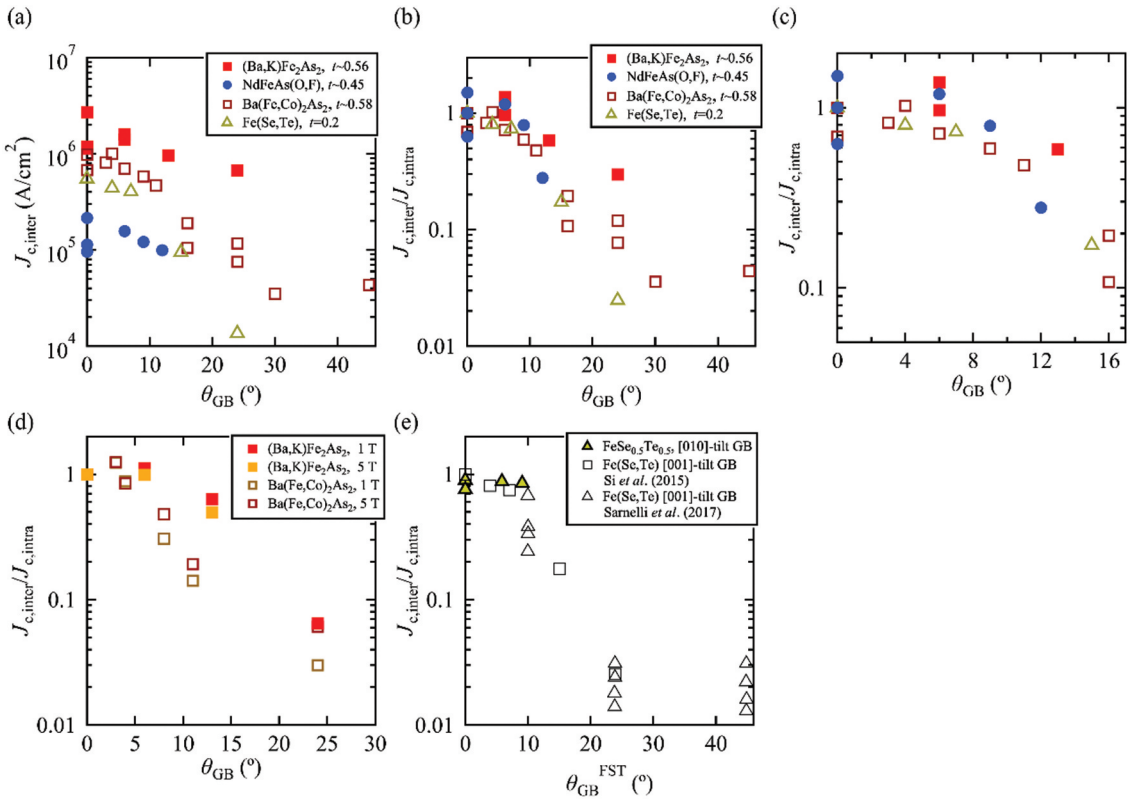

Figure 1. Grain boundary (GB) properties of various iron-based superconductors. (a) Intergrain critical current density (J_c) of [001]-tilt GBs for (Ba,K)Fe_2As_2 [19], NdFeAs(O,F) [108], Ba(Fe,Co)$_2As_2$ [69], and Fe(Se,Te) [112] as function of GB angle. The measured reduced temperatures are shown in the panel. (b) Ratio of intergrain J_c ($J_{c,inter}$) to intragrain J_c ($J_{c,intra}$) as function of GB angle shown in (a). (c) Enlarged view of (b) at $0° \leq \theta_{GB} \leq 16°$. (d) Ratio of intergrain J_c to intragrain J_c of (Ba,K)Fe_2As_2 at 12 K. Applied magnetic fields of 1 and 5 T for H||c. For comparison, the data of Ba(Fe,Co)$_2As_2$ at 4 K are shown [69]. (e) $J_{c,inter}/J_{c,intra}$ of $FeSe_{0.5}Te_{0.5}$ [010]-tilt GB as function of GB angle of $FeSe_{0.5}Te_{0.5}$ (θ_{GB}^{FST}). For comparison, the data of Fe(Se,Te) for [001]-tilt GB at 4 and 4.2 K are superimposed [104,113].

layer [107]. The epitaxial relation was confirmed to be (001)[100] $FeSe_{0.5}Te_{0.5}$||(114)[22$\bar{1}$]CeO_2. Hence, domain wall boundaries rather than GBs formed in weak-link-free $FeSe_{0.5}Te_{0.5}$. These results have some implications for mitigating the weak-link problem inherent in high-T_c superconductors, as CeO_2 is commonly utilized as a buffer layer.

Figure 1e shows the ratio of the intergrain J_c to the intragrain J_c as a function of θ_{GB}^{FST}. The ratio in the former subfigure is constant at approximately θ_{GB}^{FST} ~9°, indicating the absence of weak links. However, how the intergrain J_c changes with θ_{GB}^{FST} beyond 10° remains unclear. This issue should be addressed by fabricating [010]-tilt bicrystal films of $FeSe_{0.5}Te_{0.5}$ having $\theta_{GB}^{FST} \geq 12°$, which is the direction of our future studies.

2.3.3. Device fabrication

Possible device applications using IBS thin films include superconducting quantum interference device (SQUID) magnetic sensor systems and single-photon detectors (SPDs). A SQUID consists of a ring-shaped superconductor separated by two Josephson junctions (S/I/S, where S denotes a superconductor and I means an insulator). Because suitable insulators have not been explored for IBSs, Co-doped Ba122 [115] and Fe(Se,Te) [116] have been deposited on bicrystalline substrates to fabricate Josephson junctions using the weak coupling at GBs. The artificial GBs of these thin films are metallic, and the normal-state resistance R_n of the junctions is small, resulting in a low I_cR_n product (typically tens of microvolts). Therefore, suppression of flux noise is a challenge for the dc-SQUIDs made from Co-doped Ba122 and Fe(Se,Te).

A superconducting SPD is an electronic device for detecting single photons, which are the bearers of information in quantum cryptographic signaling. The wavelength of a single photon is 1.55 nm (0.83 eV in energy), which is sufficiently large relative to the maximum superconducting energy gap of IBSs, which is a few tens of meV. Therefore, when the superconducting nano-wires in a superconducting SPD are irradiated by a single photon, the wire section transitions from the superconducting state to the normal-conducting state, generating a voltage. This voltage becomes the detection signal of the single photon. Here, a bias current (I_B) of approximately 80–90% of the critical current (I_c), at which superconductivity is destroyed, is applied to the superconducting wires. The photon detection efficiency of a superconducting SPD is proportional to I_B, so the larger the I_c of the superconductor, the higher its detection efficiency. An important aspect of SPDs is fine wire processing, and Co-doped Ba122 [117] with a 500 nm line width and NdFeAs(O,F) [118] with a 0.84 μm line width have been reported. Recently, a thin line with a width of 0.9 μm was reported for NdFeAs(O,H) [119]; its T_c is 15% lower than the unprocessed film and a J_c of 4 MA/cm^2 at 4 K was obtained.

2.4. Polycrystalline bulk materials

2.4.1. Synthesis of 122-type polycrystalline materials

In this section, we briefly review the synthesis process of bulk polycrystalline materials of 122-type IBSs, which have the chemical composition $AEFe_2As_2$. Here, superconductivity is induced via hole doping due to alkali metal substitution at AE sites, electron doping due to transition metal substitution (e.g. Co and Ni) at Fe sites, and chemical pressure via isovalent doping (e.g. P) at As sites. Research and development for applications is particularly active on K-doped Ba122 systems [57] and the analogous stoichiometric 1144 systems [59,120]. 122-type polycrystalline materials (nonoxide ceramics) are typically synthesized using glove box equipment. Elemental metals, such as Ba, K, Fe, and As [121–123], or arsenide compounds, such as BaAs and FeAs [124], are weighed to achieve a designated chemical composition and mixed under an inert atmosphere. In this process, mechanochemical reactions may be induced using a ball-milling apparatus [79,81,106,125,126]. The resulting mixed powder is then sealed in a metal or ceramic container and heat-treated to synthesize 122-phase samples (one-step process [79]). In the case of the two-step process, the as-obtained 122 sample is ground again, followed by a second heat treatment [81,127]. The two-step process achieves 122 phases with high purity and crystallinity. Heat treatment is conducted in an inert atmosphere, such as a vacuum or Ar, to prevent oxygen contamination. Hot isostatic pressing (HIP) can effectively synthesize dense 122-phase samples at high pressures [80,128–131]. Weiss *et al* reported $(Ba_{0.6}K_{0.4})Fe_2As_2$ bulks and round wires with high transport critical current densities exceeding 0.1 MA/cm^2 (self-field, 4.2 K) through HIP at 192 MPa and 600°C [81].

The superconducting properties of IBSs are sensitive to the doping level [123,132–136]. Control of chemical composition and elemental substitution and impurity doping [89,137–150] effectively improve critical current properties. As critical current properties are also strongly influenced by microstructures, approaches to improving the synthesis process [151–167], including cold working [168–173], heat treatment conditions [83,127,174–177], high-pressure HIP [80,131,178–182], and hot pressing [183]. At more microscopic scales, GB and interface modification [109,111,122,184–190] significantly affects the transport of superconducting currents. In recent years, controlling nanostructures for more efficient

magnetic flux pinning [191–202], such as by introducing strains [203,204] and defects [121,205–207] into the grains and particle irradiation [208–211], has attracted considerable attention. Moreover, attempts have been initiated to introduce machine learning into the design of synthesis processes [17,212–215].

2.4.2. High-energy milling

A one-step process combining high-energy milling and SPS has been developed as an advanced process for Ba122 polycrystalline bulk materials with high critical current densities. Tokuta *et al* investigated the dependence of the milling energy on the superconducting properties of Co-doped Ba122 by quantifying and controlling the ball-milling conditions during planetary ball milling using elemental metals as starting materials [106]. The ball-milling energy (E_{BM}), which is the energy imposed on the powder per mass, was systematically changed. Changing the ball-milling time and precursor powders yielded different E_{BM}, which was estimated as

$$E_{BM} = c\beta \frac{(\omega_p r_p)^3}{r_v} t, \quad (1)$$

where c is a dimensionless constant on the order of 0.1, β is the mass ratio of the balls to the powder, ω_p is the angular frequency, r_p is the revolution radius, r_v is the rotation radius, and t is the ball-milling time [216,217].

With an increase in E_{BM}, the intensity distribution of the Ba122 diffraction peak broadened and the grain size of Ba122 decreased. The magnetically measured T_c (T_c^{mag}) reached its maximum value at ~60 MJ/kg and decreased by ~30% at 600 MJ/kg. The T_c value measured from resistivity (T_c^{res}) also slightly decreased with an increase in E_{BM}. The difference between T_c^{res} and T_c^{mag} could be attributed to the fact that the onset of the resistive transition corresponds to intragranular transition, whereas susceptibility transition can be attributed to the GBs. The zero-resistance temperature ($T_c^{res}{}_0$), which is mainly determined by the GB transition and the establishment of a percolative path, coincided with $T_c^{mag}{}_{onset}$ in these polycrystalline samples. The E_{BM} dependence of J_c had the maximum value, similar to the E_{BM} dependence of density and T_c^{mag} (Figure 2a). This occurred because J_c is affected by various characteristics, such as density, T_c, crystallinity, and phase purity. A change in the self-field J_c also corresponds to a microstructural change. Electron microscopy observation showed that the current path was considerably restricted due to the presence of coarse voids in low-E_{BM} samples and poor connectivity in high-E_{BM} samples, yielding the highest J_c along

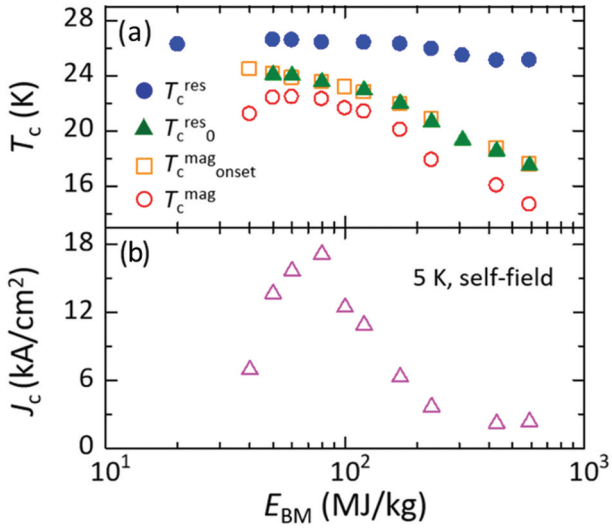

Figure 2. Ball-milling energy (E_{BM}) dependence of (a) magnetic superconducting transition temperature (T_c^{mag}) and onset T_c^{mag} ($T_c^{mag}{}_{onset}$) defined as the temperatures at which the magnetization reached 90% and 99.9% of the transition, respectively, resistive superconducting transition temperature (T_c^{res}) determined based on the 90% of the superconducting transition, and zero-resistance temperature ($T_c^{res}{}_0$) of Ba(Fe, Co)$_2$As$_2$ bulk samples and (b) critical current density (J_c) at 5 K under self-field [106].

with high purity and good intergranular connection at 80 MJ/kg.

On the other hand, the temperature-dependent slope of the upper critical field (H_{c2}) of Co-doped $BaFe_2As_2$ can be artificially tuned by introducing defects through high-energy milling at 100 MJ/kg or more [121]. With an increase in E_{BM} to ~500 MJ/kg, the slope of $H_{c2}(T)$ increased by ~50% (from 4 T/K to 6 T/K) and exceeded those of single crystals and thin films [121]. Nanograins with remarkably high densities of planar defects parallel to (001) were observed in Co-doped $BaFe_2As_2$ bulks processed at E_{BM} ≈100 MJ/kg [207]. STEM revealed that the planar defects had a thickness of ~1 nm and an average spacing of ~5.7 nm, which was several times the superconducting coherence length [207]. Recently, a theoretical model for the effects of nonmagnetic disorder on the H_{c2} slope was proposed by Kogan *et al.* [206,218]. The observed planar defects may contribute to the observed enhancement in H_{c2} as nonmagnetic scattering centers. Excluding ex situ formation via particle irradiation (few examples have been reported), high-energy milling is expected as a new technique for the in situ formation of dense defects during crystal formation for IBSs.

2.4.3. SPS

In SPS, pulsed current is applied to a sample at uniaxial pressure to generate Joule heat within the sample. SPS is also called the field-assisted sintering technique.

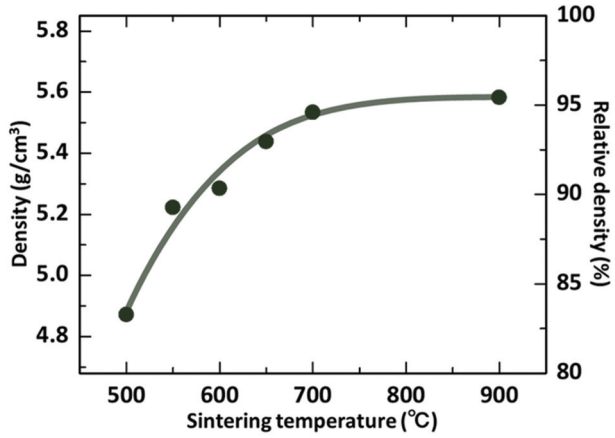

Figure 3. Sintering temperature dependence of density (left axis) and relative density to theoretical density (right axis) of $(Ba,K)Fe_2As_2$ bulk samples [79].

Compared with conventional heat treatment in an electric furnace, SPS has a faster ramp rate, and dense samples can be obtained in a shorter heat treatment period. SPS is therefore used to sinter various ceramic materials [219,220]. In a K-doped Ba122 system, potassium metal with a high equilibrium vapor pressure tends to volatilize during heat treatment. Volatilization of potassium, a carrier dopant, degrades superconducting properties due to the formation of impurity phases, in addition to shifting the doping level from the optimal state. In this sense, fast synthesis via SPS is appropriate for systems containing volatile elements.

Tokuta *et al* reported the synthesis of K-doped Ba122 bulk discs with a diameter of 10 mm using SPS from precursor powders prepared via high-energy ball milling [79]. Figure 3 shows the relative density of the K-doped Ba122 bulks as a function of sintering temperature. The relative density increased asymptotically with the sintering temperature; sintering above 600°C yielded a high relative density of over 90%, which reached 95% during sintering at 900°C. This relative density is comparable with those of previously reported IBS bulks made via SPS, such as $NdFeAsO_{0.75}F_{0.25}$ (96%) [221], $FeSe_{0.5}Te_{0.5}$ (90%) [222], Co-doped Ba122 (~80%) [223], and $CaKFe_4As_4$ (96.2%) [124]. T_c increased monotonically with the sintering temperature from 33.1 K for a sample sintered at 500°C to 37.8 K for a sample sintered at 900°C; which was comparable with that of single crystals [57]. This was due to high crystallinity and the short dwell time of 5 min, which suppressed potassium evaporation and achieved a near-optimal doping level (40%). Samples sintered at 600°C and 650°C showed high J_c values exceeding 10^5 A/cm^2 at 5 K and under self-field [79].

3. Data acquisition

Figure 4 shows the multiscale and multidimensional electron microscopy imaging platform for the present study. How the platform works for the present IBS research will be described below.

3.1. Multiscale observation

The critical current is an important physical property of superconducting materials for practical use. Transport current properties are greatly influenced by the material microstructure, and process conditions must be clarified to control and improve a microstructure. Various mechanisms have a dominant effect on current properties, including flux pinning [224], connectivity [225–227], misorientation [68,69,228], impurity [73], and weak links [229] at GBs. Therefore, various microstructural elements should be considered, such as the macroscopic

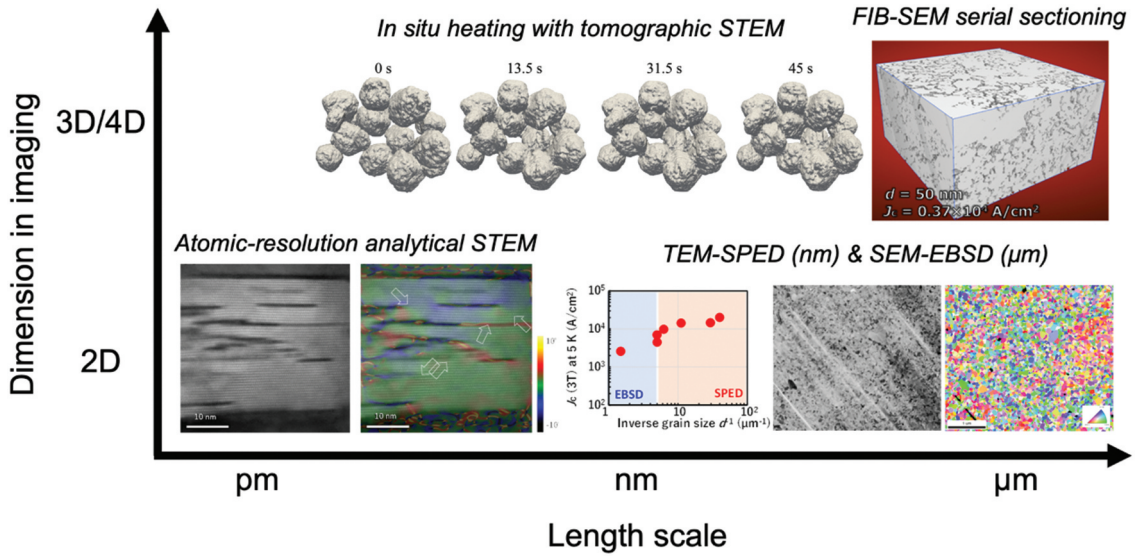

Figure 4. Mutiscale and multidimensional electron microscopy imaging platform for the present study.

packing factor and reproducibility, GBs, and crystal defects at the atomic scale. In particular, in the studied polycrystalline bulk materials, extracting these microstructural elements is challenging due to their complex interactions. Nonetheless, the recent development of electron microscopy has been significant, and various types of microstructural imaging methods are available. Recently, Shimada *et al.* reported multiscale microstructural analysis to quantify the complex structures of polycrystalline superconducting bulks using different electron microscopy techniques [230]. Specifically, scanning electron microscopy (SEM) and scanning TEM (STEM) were used for multiscale imaging. A narrow region of bonding called a neck was seen at the connection between polycrystalline aggregates in a self-sintered Ba122 bulk, as shown in Figure 5 The quantitative analysis of the neck is described in detail in Section 4.2, showing that this analysis elucidates the specific microstructure of this superconducting bulk material. Another specific microstructure of the Ba122 bulk material was the structural defects within grains and at GBs, as shown in Figure 6; as microstructural elements, these defects influenced current properties [207,230]. In particular, the surface defects observed as intragrain structures (a) were three-dimensionally distorted by the defect strain, which was determined by measuring the atomic displacements using geometric phase analysis (GPA) (b). However, high-resolution observation of the GBs of the Ba122 bulk suggested the presence of four major types of structures, as seen in subfigures (c)–(f). Furthermore, a Ba – O-rich amorphous phase (d) formed at the GBs with uniform thickness, suggesting that the liquid phase was involved in the microstructure formation reaction.

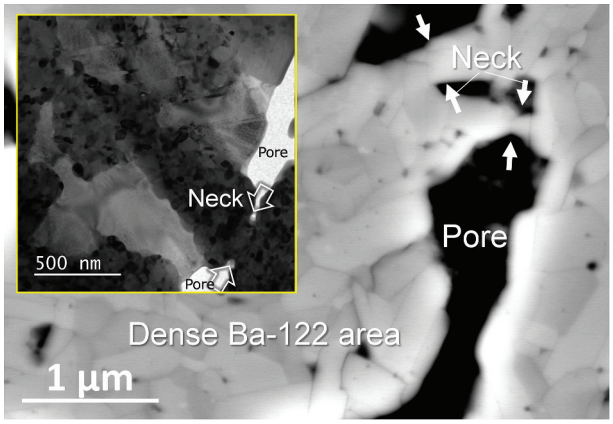

Figure 5. Image in scanning electron microscopy in backscattered electron mode of Co-doped Ba122 bulk fabricated via self-sintering through mechanochemical process [230]. The inset shows a bright-field transmission electron microscopy image of neck area.

Combining high-energy mixing and SPS, as reported by Tokuta *et al.*, dramatically improved the bulk packing ratio and suppressed the neck area, highlighting the need to consider the influence of GBs. Furthermore, considering the fine grains (less than 100 nm) of Ba122 with good transport properties fabricated via mechanochemical ball milling, we developed a multiscale crystal orientation analysis method for quantitative GB analysis. This method combines electron backscatter diffraction using SEM, scanning precession electron diffraction (SPED) using TEM, and the material scale for crystal orientation analysis on scales ranging from submillimeters to a few nanometers. The TEM-SPED method is a well-proven method for metallic materials, and we were the first to apply it to a polycrystalline superconductor [231]. Figure 7 shows an example of TEM-SPED analysis (a) and the misorientation angle of GBs obtained from Co-doped Ba122 bulk (b). Our bulk has a slightly increased frequency of low-angle grain boundaries, which is not an external factor, and is also more randomly oriented than tape wire, as is the case with round wire [80]. Thus, the

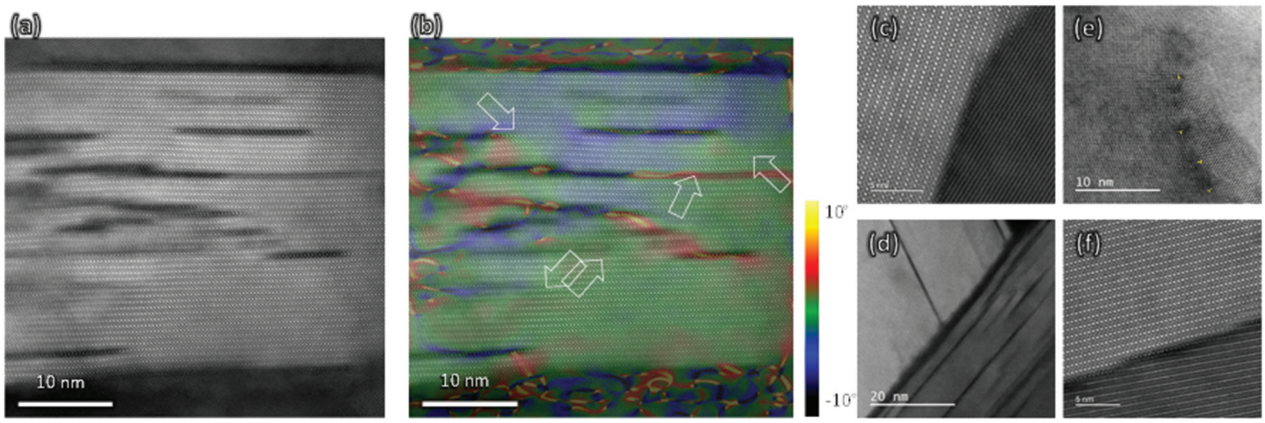

Figure 6. (a) High-angle annular dark-field scanning transmission electron microscopy (HAADF-STEM) image of planar defects in Ba122 bulk and (b) geometric phase analysis. The arrowheads in (b) indicate the strained area due to planar defects. (c)–(f) HAADF-STEM images of grain boundaries: (c) randomly oriented boundary, (d) boundary with amorphous phase, (e) small-misorientation-angle boundary, and (f) *c*-axis-oriented boundary.

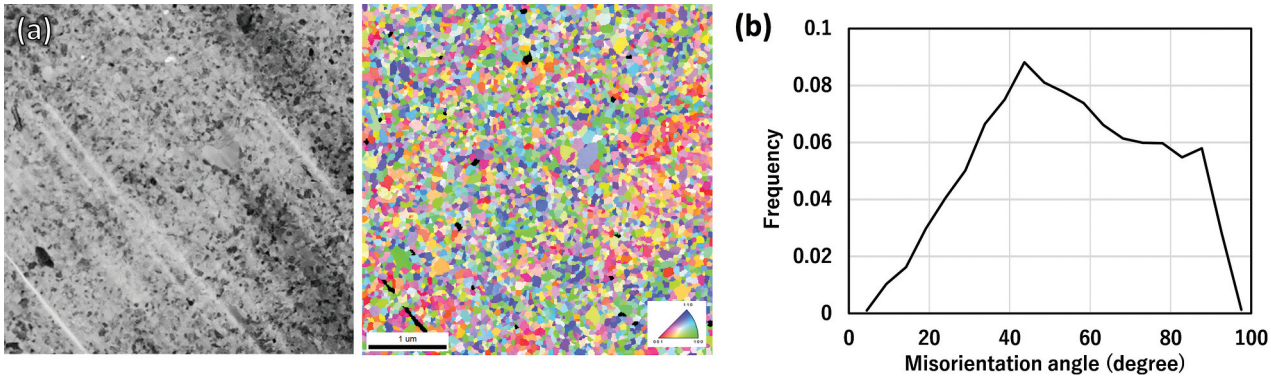

Figure 7. (a) Bright-field scanning transmission electron microscopy image and inverse pole figure map acquired via transmission electron microscopy – scanning precession electron diffraction of Co-doped Ba122 bulk. (b) Misorientation angle of GBs obtained from grain orientation data of (a).

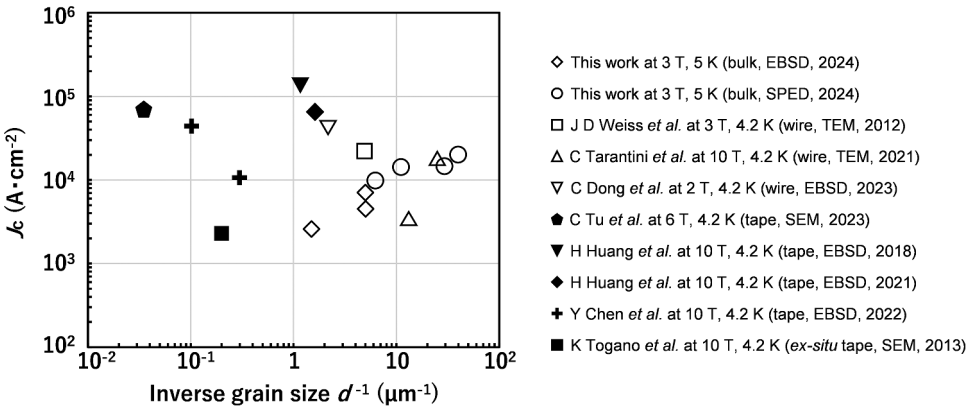

Figure 8. Correlation between J_c and inverse grain size for K-doped Ba122. Open symbols indicate data for randomly oriented bulks/wires [20,79,81,230,232] and closed symbols indicate data for uniaxially oriented tape wires [174,188,233–235]. J_c measurement conditions and grain size measurement methods are shown in each paper [20,38,79,81,174,188,230,232–235].

SPED method can quantify nano-sized grain size as well as the grain boundary characters.

Figure 8 shows the correlation between J_c and the inverse grain size reported previously, including our data. In randomly oriented polycrystals such as bulk and round wire, the grain size is often less than 1 μm, and more recently, less than 100 nm. In the case of randomly orientated bulk and wire, the improvement in J_c with a decrease in grain size proposed by the conventional flux pinning model and the Josephson junction model [184] was consistent down to grain sizes of ~25 nm. Tapes have high J_c even when the grain size is 1 μm or larger, but the correlation with grain size is small, which is due to the high frequency of c-axis orientation. On the other hand, intergranular impurities have been reported in all types of polycrystalline Ba122 [72,228], suggesting that in addition to grain size, control of grain boundary structure is necessary in the future.

3.2. In situ 3D electron microscopy: a case study using Cu nanoparticles (NPs)

In the optimization of process parameters of material fabrication to obtain ideal microstructures, these parameters are difficult to determine from databases, especially in the case of new materials. The present study proposes a method for predicting these process parameters by combining actual microscopic data with computer simulations. Assuming that a Ba122 bulk superconducting material is to be fabricated, the sintering process of powder materials is the subject of research. From the point of view of superconducting properties, the optimal polycrystalline grain size should be fine, ranging from tens of nanometers to submicrons [207]. The formation of such a nanoscale polycrystalline structure during sintering is directly observed under conditions close to those presently used for actual sintering, and the temporal microstructure evolution is acquired as in situ microscopy data. The observed temporal microstructure evolution is reproduced through phase-field (PF) simulation, which is described in detail in the following sections. A microstructure with ideal material properties will be understood by studying the correlation between superconducting properties and microstructures. Once an ideal microstructure is designed, the ideal microstructure will be generated virtually on a computer via the PF simulation, which can reproduce the observed temporal microstructure evolution. From

the simulation results, the sintering parameters are predicted to achieve optimal microstructure control, and these are fed back into the actual sintering process.

In situ 3D electron microscopy [16] is suitable for studying the abovementioned microstructure control process. In situ electron microscopy has developed rapidly in recent years, and it is being used to study various materials, such as batteries and catalysts. One of the reasons for the development of in situ electron microscopy is the possibility of precisely applying various stimuli to a small specimen using a microelectromechanical system (MEMS) on a specimen holder. For example, a MEMS microheater enables rapid specimen heating and cooling [236]. In addition, given a micrometer-to-nanometer-scale sample that can be placed on a MEMS chip, the heat capacity of the sample and the heater can be reduced such that the sample drift during heating experiments is significantly smaller than that in a conventional heating experiment using a millimeter-scale sample; moreover, atomic-resolution observation and electron tomography (ET) observation, which were previously difficult to combine with in situ heating experiments, are now possible [237]. For 3D electron microscopy methods, the development of ET using TEM or STEM has been remarkable, and the spatial resolution of ET can reach the atomic scale. By combining in situ and 3D imaging techniques, four-dimensional (4D; space and time) electron microscopy enables the visualization of nanoscale 3D material dynamics, such as sintering [16].

As an example of obtaining 4D image data of the sintering process using the above approach, in situ heating with ET observation was applied to the sintering of Cu NPs [16]. The in situ heating with ET observation method described here is optimized for the single-component Cu NPs, and further technical development would be required to apply this method to observe the sintering of the multi-component Ba122 materials.

Because Cu NPs can be easily oxidized, each sample must be prepared and inserted into the electron microscope column without contact with air to avoid oxidation. This experimental procedure could be used to observe the sintering process of Ba122 particles, which can be easily oxidized. For in situ heating with ET experiments without air exposure, we developed a dedicated specimen holder equipped with a MEMS stage for specimen heating that can prevent specimen oxidization due to air exposure (Figures 9b,c [16]). The MEMS specimen stage can be stored inside the holder shaft, and it can be inserted into a TEM column without exposing the specimen to air.

Figure 9d shows the heating history of the specimen during ET observation [16]. During the acquisition of tilt-series datasets, the temperature of the MEMS stage, where the specimen was placed, was set to 200°C (T1, T2, etc. in Figure 9d). No sintering progress was observed at this temperature. The temperature was set to 350°C to continue sintering, and the holding time was ~ 5 s in the initial stage of observation. In a later stage, the sample was heated until the shape of the Cu particles changed ('Heating' in Figure 9d). The temperature at which sintering was performed was denoted as the process temperature (PT), and each duration for PT holding is listed in Figure 9d. The temperature control series was implemented within 0.1 s. Such instantaneous temperature control is an advantage of using the MEMS stage. Tilt-series images were recorded at 2° intervals at a specimen tilt angle range of ± 40°, and 18 tilt-series datasets were acquired. The total number of incident electrons and the electron dose were calculated to be 2.69×10^8 e^- and 250 e^- nm^{-2}, respectively. This total number of incident electrons is almost half of the generally accepted ultra-low dose TEM tomography imaging with a direct electron detection camera [238]. However, noise was noticeable because of the extremely low electron dose (and thus insufficient signal volume) in tilt-series acquisition. When 3D reconstruction processing was performed on the acquired tilt-series datasets, the 3D particle shapes were difficult to reproduce due to the influence of noise. Therefore, before 3D reconstruction processing, noise was reduced using the block matching and 3D filtering (BM3D) algorithm [239], which is a noise filter.

Figure 9e shows the 3D reconstruction results obtained through in situ heating and ET observation. The 3D image reconstruction method used was iterative series reconstruction [238] based on a compressed sensing algorithm, which is less affected by information loss due to insufficient specimen tilt angles compared with conventional algorithms, such as filtered back-projection and the simultaneous iterative reconstruction technique [240]. As the distance between Cu particles decreased with heating, necking occurred between particles, which is characteristic of sintering. For comparison, we also observed a specimen that was continuously heated at the same PT, but no significant difference in necking was observed. Therefore, the series of 3D-reconstructed images obtained in this study reproduced the sintering behavior of the Cu NPs in almost real time.

Since the synthesis of Ba122 requires more than three elements (Ba, Fe, As, Co/K, etc.), including the dopant element, and since the raw powders are expected to have different size distributions, it is challenging to synthesize Ba122 uniformly in the small sample space inside an electron microscope and to observe the reaction process using the in situ heating and ET observation method. Therefore, the application of in situ heating and ET observation to Ba122 is currently limited to the sintering process of Ba122

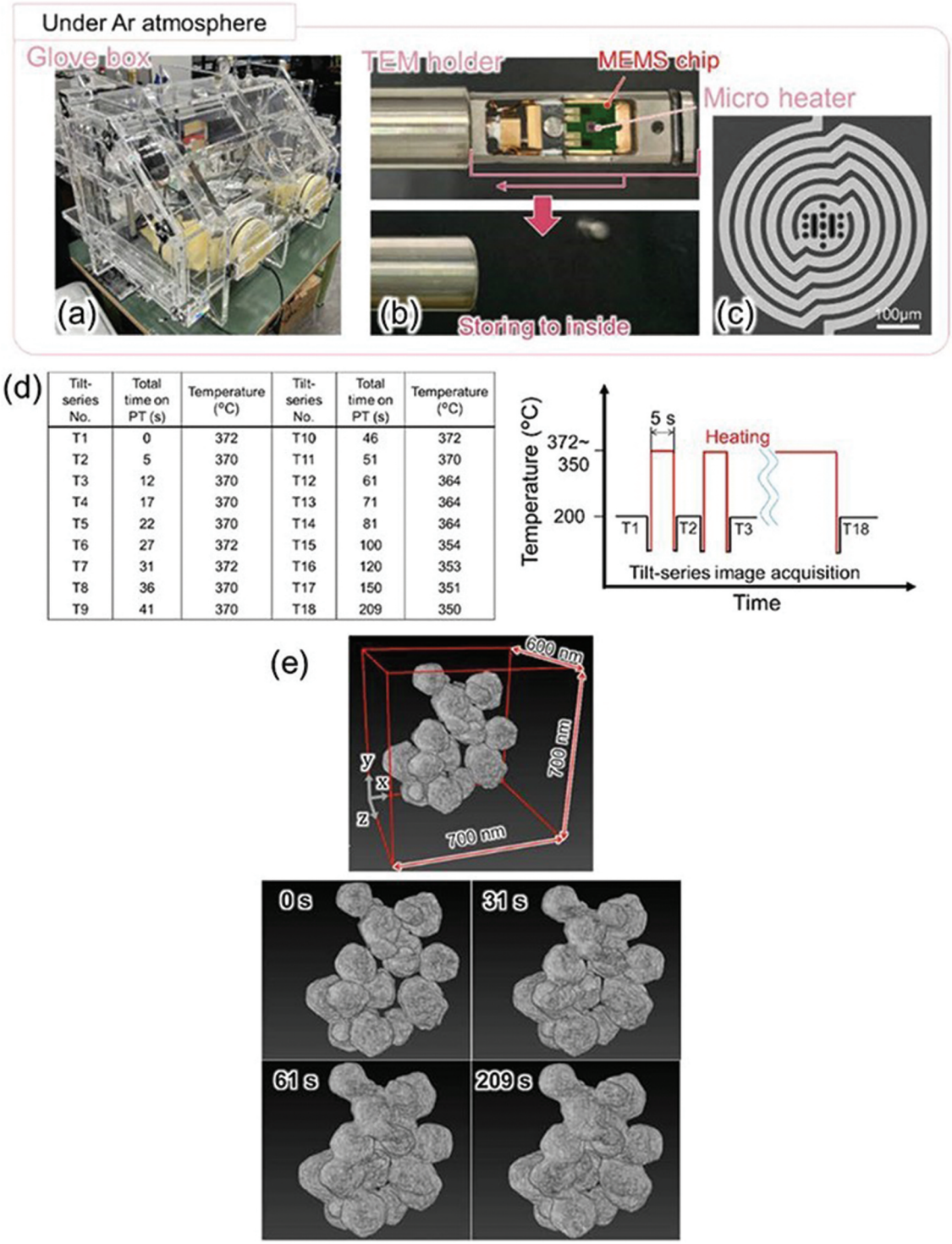

Tilt-series No.	Total time on PT (s)	Temperature (°C)	Tilt-series No.	Total time on PT (s)	Temperature (°C)
T1	0	372	T10	46	372
T2	5	370	T11	51	370
T3	12	370	T12	61	364
T4	17	370	T13	71	364
T5	22	370	T14	81	364
T6	27	372	T15	100	354
T7	31	372	T16	120	353
T8	36	370	T17	150	351
T9	41	370	T18	209	350

Figure 9. Specimen preparation/transfer/heating system for in situ heating with electron tomography observation of nanoparticles (NPs) [16]. (a) Sample preparation processes for transmission electron microscopy (TEM) observation (all performed in Ar-gas-filled glove box). (b) Sample carried by newly designed microelectromechanical system (mems) – based in situ heating holder with maintained air tightness. (c) Cu NPs dispersed on MEMS microheater. (d) Table and schematic diagram showing heating process in TEM. Because the MEMS holder can instantaneously increase or decrease the sample temperature, a tilt-series dataset can be acquired at a standby temperature (200°C) immediately after each heating step. (e) Temporal evolution of 3D morphology of Cu NPs during heating. The obtained data were averaged in the range of $3 \times 3 \times 3$ pixels (30.4 nm^3) for visibility. Reproduced from [16] with permission from the royal society of chemistry.

particles and their coarsening. The authors conducted preliminary in situ heating and STEM observation and confirmed that aggregates of Co-doped Ba122 particles are sintered by heating in the electron microscope. However, it is unclear to what extent the constituent elements of the Ba122 particles were vaporized during the in situ heating experiment.

As described above, this section reviews 3D visualization and evaluation methods for the sintering of Cu NPs [16]. Nanometer-sized particles with a high

surface area ratio exhibit a different sintering behavior compared with coarse powders or bulk materials, and quantitatively predicting this change over time using conventional sintering theory is difficult. The experimental method demonstrated here is one of the few techniques that can efficiently perform statistical measurements, leading to the prediction of sintering behavior at the nanoscale. The 3D nanoscale dynamics images obtained through in situ heating and ET observation can be used for dimensional measurements and a wide range of other applications, such as calculation of the microstructure formation process and even estimation of microstructure control process parameters, by assimilating the data with those from PF simulation, as described in the following sections.

4. Computational approach

4.1. Quantification of 3D structural data using deep learning

As described in the previous sections, microstructures significantly influence the current properties of polycrystalline superconductors. In bulk materials, these microstructural elements are distributed three-dimensionally. This complex 3D microstructure should be modeled (or quantified) in cyberspace to apply process informatics in this framework. Due to developments in recent structural analysis methods, computed tomography methods using X-rays and TEM [241–244] and serial sectioning methods combining focused ion beams and SEM [245] have enabled acquisition of original 3D structural data on a scale ranging from several tens of nanometers to submillimeters. However, because nearly 1000 pieces of data are acquired, the highest accuracy can be achieved if a human performs all image segmentation, requiring considerable time and effort. Furthermore, even with batch image processing, the measurement errors caused by experimental artifacts and noise in the original data are incompatible with conventional methods, such as thresholding, which reduces the accuracy of phase segmentation. Recently, Hirabayashi *et al.* used semantic segmentation based on deep learning using fully convolutional neural networks (FCNs) as a solution to the abovementioned problems [17]. Figure 10 shows an overview of their method. This approach uses U-Net model, whose network is based on the FCN model. The actual experimental data are used as the training data, and measurement errors are introduced into the training data to achieve highly accurate (intersection over union = 94.6%) segmentation. They also generated phase-identified 3.66×10^8 voxel data of the microstructure of a superconducting bulk material. Their phase recognition method, which is based on deep learning, is not limited to two-phase structures, such as superconducting phases and voids. It can be applied to multiphase structures with the addition of impurities and other factors.

Combining 3D observation and semantic segmentation is a useful way to quantify actual microstructural information in complex phase structures, such as bulk superconductivity, by modeling from real space to cyber space.

4.2. The acquisition of novel 3D structures correlated with superconducting property

Connectivity and grain size are important microstructural elements that influence the critical current properties of the polycrystalline superconducting bulk. Connectivity is correlated with the volume fraction of the bulk [225,226], and it can be improved by processes such as diffusion [246,247] and hot pressing [248,249]. As for grain size, the finer the grain size, the better the current properties, as described in Section 3.1. However, in the self-sintered Ba122 bulk with 50 nm grains fabricated in this project, a different correlation was observed: the critical current property decreased with the grain size. Furthermore, the volume fractions of these bulks are comparable, and conventional approaches

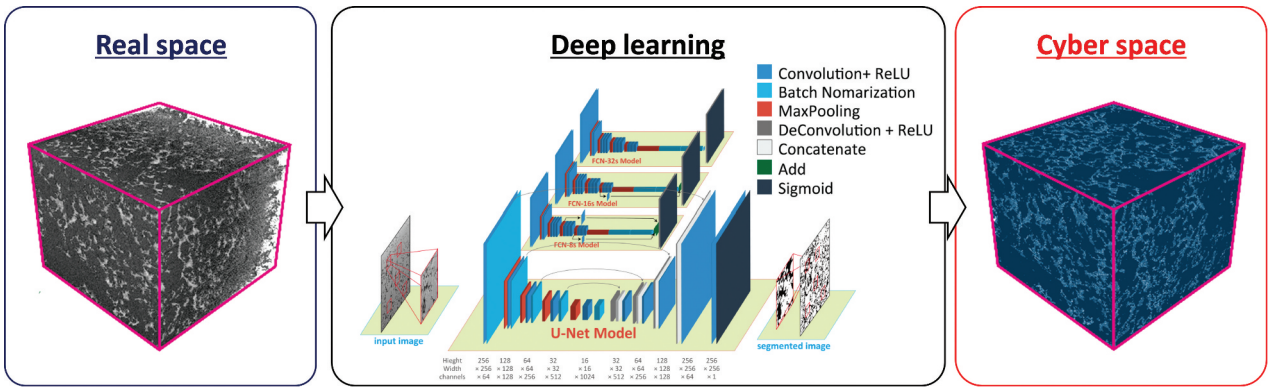

Figure 10. Modeling of 3D microstructures of actual materials via deep learning [17].

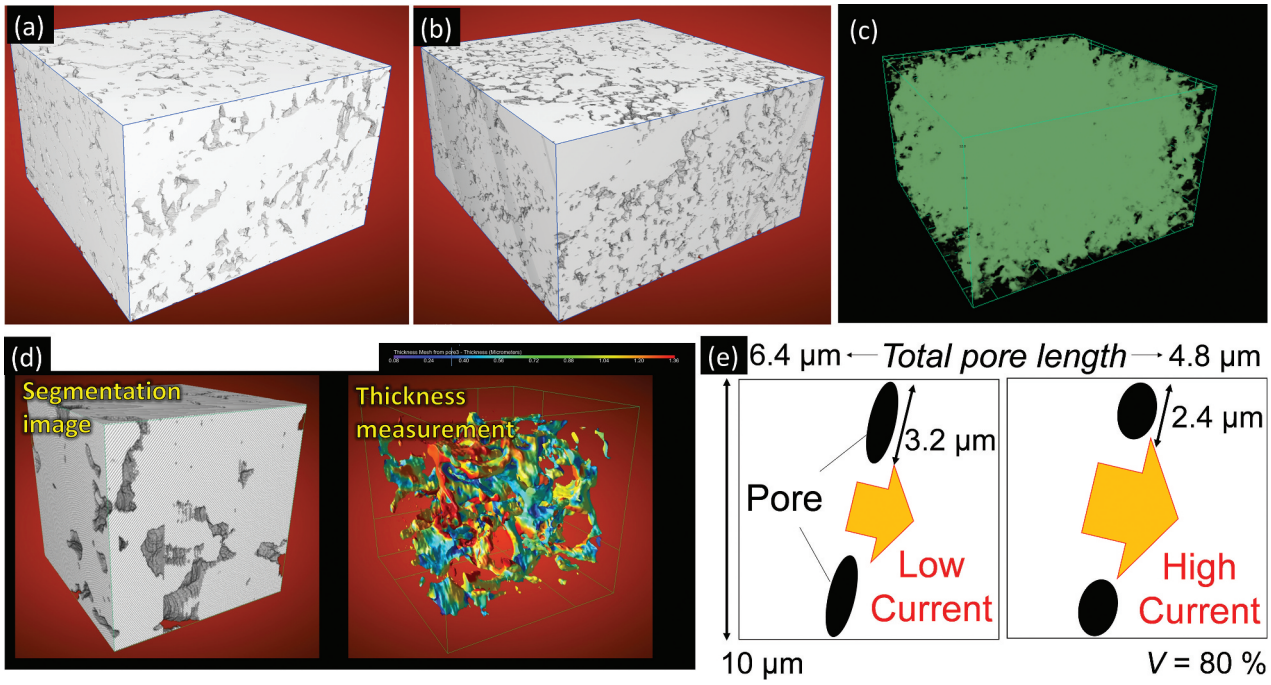

Figure 11. 3D segmentation images of Ba-122 phase of the bulks fabricated with E_{BM} of 80 MJ/kg (a) and 230 MJ/kg (b), and that of pore of the bulk E_{BM} of 80 MJ/kg (c). The J_c obtained at 5 K under self-field and grain size of the bulk fabricated with E_{BM} of 80 MJ/kg and 230 MJ/kg are 1.7×10^4 A/cm^2 and 3.7×10^3 A/cm^2, 140 nm and 50 nm, respectively [15]. The example of method for measurement thickness of 3D-reconstructed image (d). (e) is schematic diagram of relationship between total pore length and local current.

cannot easily elucidate this difference. Therefore, we modeled the 3D microstructure of the actual Ba122 bulk via deep learning, as described in Section 4.1 [15]. The reconstructed images are shown in Figure 11a,b. These quantification of 3D structural data enabled the extraction of information that was previously unavailable for two-dimensional data; this information included the fact that 90% of the volume of the voids in the bulks were connected to each other and reached the bulk surface obtained using the segmentation data of pore as shown in (c). In addition, we quantified the microstructure, focusing on the 3D superconducting phase connections, and proposed two new microstructural parameters that influence current properties, namely, the local superconducting phase thickness and void length (surface area), which both extract the neck structure. The thickness of the local superconducting phase is indicated by the minimum diameter in each voxel of the superconducting phase surface that reaches the other surfaces in the sphere where that point is a contact point. Thickness maps obtained from an actual data set are shown in (d). For these parameters, a bulk with higher transport current properties has a larger local thickness average and shorter void length. Hence, at the same volume fraction, shorter, more discrete voids improve the global transport current of the bulk without causing localized cross-section of current path reductions, such as at the neck as shown in (e). This result is the first quantitative observation of the effect of the cross-sectional area of the macroscopic particle connection area (neck). As for the process, the results suggested that the higher the powder milling energy, the narrower the neck area and the lower the connectivity, resulting in lower transport current. However, because the powder milling energy is positively correlated with inverse grain size, SPS, which is a process improvement strategy that preferentially heats the powder contacting area during sintering, has been used to fabricate bulks with wide necks and achieve excellent critical current properties while maintaining a high milling energy [79].

Thus, a novel approach that incorporates data science into conventional materials experimental methods is being promoted for superconducting materials. Researchers can use artificial intelligence (AI) to 'extract' the structural elements that influence current properties, which have been overlooked in studies on complex microstructural information, leading to faster, more efficient material development.

4.3. Data assimilation of PF simulation and in situ observation for solid-state sintering

Various methods for producing superconducting materials have been proposed. Solid-state sintering is an effective way to produce polycrystalline bulk superconducting materials. During the solid-state sintering, a polycrystalline microstructure forms through particle

bonding, grain growth, and macroscopic densification of the system. However, the sintering mechanism in the production of polycrystalline bulk superconducting materials is largely unknown, so the solid-state sintering process in such materials is difficult to predict. Therefore, integrated studies using both experiments and numerical simulations are needed, as reviewed in this paper.

The PF method (PFM) is a powerful numerical simulation technique that is widely used to simulate polycrystalline microstructure formation in various materials [250]. In existing studies, PFM is often used to simulate the solid-phase sintering and polycrystalline grain growth in metallic materials and ceramics [251–253]. However, PFM requires physical property values and material parameters because it is a phenomenological continuum model. Although these values and parameters are available in studies about basic metallic and ceramic materials, they are largely unknown for superconducting materials.

We propose that the physical property values and material parameters necessary for high-fidelity PFM simulations can be obtained through two major methods. One is data-driven modeling, in which physical property values and material parameters are estimated directly from experimental data. The other is physics-driven modeling, in which physical property values and material parameters are identified via multiscale analysis combining first-principles calculation, molecular dynamics, and PFM. In this section, we present an example of data-driven modeling involving in situ observation of polycrystalline microstructure formation through solid-phase sintering and data obtained from experimental observations. In particular, this section shows the inverse estimation of the physical property values and parameters required for the PF simulation. In this section, we focus on the solid-phase sintering of Cu NPs for a proof-of-concept of our data-driven modeling. We review the data assimilation based on the in situ observation data presented in Section 3.2 using data assimilation based on Bayes' theorem [254,255].

4.3.1. PF model for solid-state sintering

This section describes the PFM for solid-state sintering and the data assimilation method used in this study. The PFM is only briefly discussed, as its detailed formulation is in a previous paper [251].

Polycrystalline microstructure formation during solid-state sintering is simulated by numerically solving the following partial differential equations for the order parameters [256]:

$$\frac{\partial \eta_i}{\partial t} = -M_\eta \frac{\delta F}{\delta \eta_i} - \quad \cdot \left(\eta_i \boldsymbol{v}_i\right), \tag{2}$$

$$\frac{\partial \rho}{\partial t} = \quad \cdot \left(M_\rho \quad \frac{\delta F}{\delta \rho} - \rho \sum_i \boldsymbol{v}_i \right). \tag{3}$$

Here, N is the density field, ρ and η_i ($i = 1, 2, \ldots, N$) is the existing probability of Cu NPs. N is the number of Cu NPs in a system. ρ and η_i changes from 0 to 1 in the interfacial region. $\boldsymbol{v}_i$ denotes the translation velocity of the ith Cu NP and is calculated using the method proposed by Wang [251]. F is the total free energy of the system. M_η is the mobility of η_i, which characterizes the GB mobility. M_η is the mobility of ρ and computed using the following equation:

$$M_\rho = M_{\mathrm{vol}} h(\rho) + M_{\mathrm{vap}}\{1 - h(\rho)\} + M_{\mathrm{surf}} \rho^2 (1-\rho)^2 + \sum_i \sum_{j \neq i} M_{\mathrm{gb}} \eta_i \eta_j, \tag{4}$$

where M_{vol}, M_{vap}, M_{surf}, and M_{gb} are the volume, vapor, surface, and GB diffusion mobilities, respectively. These mobilities are functions of each diffusion coefficient: D_{i} (i = vol, vap, surf, gb). $h(\rho)$ is an interpolation function. The temperature dependency of D_{i} (i = vol, vap, surf, gb) is described using the Arrhenius-type equation $D_{\mathrm{i}} = D_{\mathrm{i}}^{0} \exp(-Qi/(RT))$.

4.3.2. Data assimilation methodology

This section outlines the data assimilation methods used in this study. Additional details are in previous papers [257,258]. Our proposed data assimilation methods are nonsequential data assimilation approaches based on the 4D variational (4DVar) method [259,260]. The 4DVar method minimizes the following cost function, which is derived based on maximum likelihood estimation:

$$J(\mathbf{x}_0) = \frac{1}{2}\left(\mathbf{x}_0 - \mathbf{x}_0^b\right)^T \mathbf{B}^{-1}\left(\mathbf{x}_0 - \mathbf{x}_0^b\right) + \sum_{t=0}^{t_{end}} \frac{1}{2}\left(H_t(\mathbf{x}_t) - \mathbf{y}_t\right)^T \mathbf{R}_t^{-1}\left(H_t(\mathbf{x}_t) - \mathbf{y}_t\right). \tag{5}$$

This cost function represents the time integral of the mismatch between the experimental and numerical simulation data at time t ($t = 0 \sim t_{\mathrm{end}}$) of the in situ observation. In Equation (5), $\boldsymbol{x}_t$ is a state vector, whose components are the state variables and parameters whose time evolution is to be estimated in the numerical simulation, and $\boldsymbol{y}_t$ is an observation vector, whose components are the experimental data. Here, the subscript t denotes time. $\boldsymbol{x}_0^b$ is a background vector representing the initial state and the initially estimated value of the parameter to be estimated. These vectors are stochastic variables. H_t is the observation operator, which is used to compare $\boldsymbol{x}_t$ and $\boldsymbol{y}_t$. T denotes transposition. $\boldsymbol{B}$ and $\boldsymbol{R}_t$ are the background error covariance matrix and the observation error covariance matrix, respectively. These matrices represent the

uncertainties of the initial estimate and the observed data, respectively.

The gradient of the cost function is generally used to minimize the cost function. However, analytically deriving the gradient of the cost function is difficult, especially for nonlinear numerical models, such as the PF model used in this study. The ensemble 4DVar method [256] can minimize the cost function without using its gradient, but it is computationally expensive. Therefore, we developed novel nonsequential data assimilation methods that are named DMC-BO and DMC-TPE methods [257,258]. These data assimilation methods do not need to derive the gradient of the cost function using Bayesian optimization. In the following, we show the inverse estimation results of material parameters for the PF simulation of solid-state sintering from in situ observation data using DMC-TPE.

The particle distribution obtained from the in situ observation of Cu NP sintering, as shown in Section 3.2, was converted into 3D voxel data and utilized as the observation data. The following shows the inverse estimation results of five material parameters. The size of the computational domain used in the PF simulation of sintering was 820 nm × 820 nm × 820 nm. The number of computational grid points was $N_{grid} = 128 \times 128 \times 128$. The number of Cu NPs in the computational domain was $N = 24$. The sintering temperature and time were 350°C and 50 s, respectively. The surface energy was set to $\gamma_{surf} = 1.35$ J m^{-2} [261]. The GB energy was assumed to depend on temperature and was set to $\gamma_{gb} = 0.783 - 1.34 \times 10^{-4}\ T$ J m^{-2} [262]. The parameters related to the advection velocity were $\rho_0 = 0.98$, $c = 0.14$, and $m_{ro} = m_{tr}/100$ [251]. The time increment was $\Delta t = 1 \times 10^{-3}$ s. The volume and vapor diffusivities were $D_{vol} = 1.0 \times 10^{-21}$ m^2 s^{-1} and $D_{vap} = 1.0 \times 10^{-22}$ m^2 s^{-1}, respectively.

The parameters D_{surf}, D_{gb}, m_{tr}, M_η, and k_{st} were estimated via data assimilation based on DMC-TPE. In the iterative calculation performed to minimize the cost function based on the TPE algorithm, the maximum number of iterations was set to 100. The state vector ($\boldsymbol{x}_t$) contains the ordered parameters (ρ and η_i) at all computational grid points and the five parameters to be estimated. Therefore, the dimension of $\boldsymbol{x}_t$ is $N_{grid} + NN_{grid} + N_p$, where N_p is the number of parameters to be estimated and $N_p = 5$. The observation vector $\boldsymbol{y}_t$ includes the variable ψ, which represents the presence of Cu NPs obtained through in situ observation. ψ denotes the voxel data; it equals 1 inside a Cu particle and 0 otherwise. The dimension of $\boldsymbol{y}_t$ is N_{grid}. $\boldsymbol{B}$ and $\boldsymbol{R}_t$ are assumed to be diagonal matrices, and their dimensions are equal to those of $\boldsymbol{x}_t$ and $\boldsymbol{y}_t$, respectively. The mean values and ranges of the initial estimates of the parameters to be estimated are shown in Table 1.

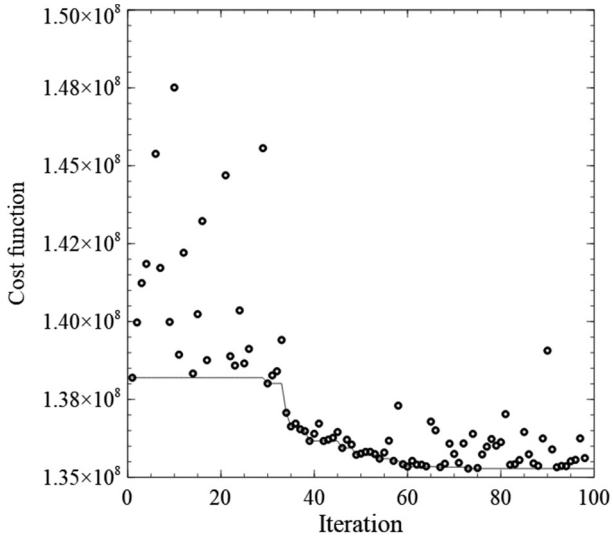

Figure 12. Evolution of cost function calculated through DA using in situ observation data. The solid line shows the evolution of the cost function minimum updated during iterative minimization.

Figure 12 shows the minimization of the cost function with respect to the number of PF simulation iterations. Bayesian optimization based on the TPE algorithm was used in this study, so global and local minimization were performed automatically. Therefore, the value of the cost function did not decrease continuously. After 30 iterations, the cost function was successfully minimized. Among the 100 iterations, the minimum value of the cost function was obtained in the 73rd iteration.

The optimal material parameters for minimizing the cost function were as follows: $D_{surf} = 0.988 \times 10^{-16}$ m^2/s, $D_{gb} = 1.090 \times 10^{-17}$ m^2/s, $m_{tr} = 0.948 \times 10^{-20}$ m^5/(Js), $M_\eta = 0.654 \times 10^{-9}$ m^3/(Js), and $k_{st} = 1.219 \times 10^6$ N/m^2. The estimated D_{surf} was close to a previously reported value [263]. To show that the optimally estimated parameters enables the

Table 1. Means of initially estimated values and searching ranges for five parameters to be estimated using data assimilation based on DMC-TPE method.

Parameter	Mean of initially estimated value	Searching range
Diffusion coefficient of surface, D_{surf} [m^2/s]	1×10^{-16}	$0 \le D_{surf} \le 2 \times 10^{-16}$
Diffusion coefficient of GB, D_{gb} [m^2/s]	1×10^{-17}	$0 \le D_{gb} \le 2 \times 10^{-17}$
Translational mobility, m_{tr} [m^5/(Js)]	0.5×10^{-20}	$0 \le m_{tr} \le 10^{-20}$
Mobility related to GB migration, M_h [m^3/(Js)]	0.5×10^{-9}	$0 \le M_h \le 10^{-9}$
Stiffness constant, k_{st} [N/m^2]	10^7	$10^6 \le k_{st} \le 10^8$

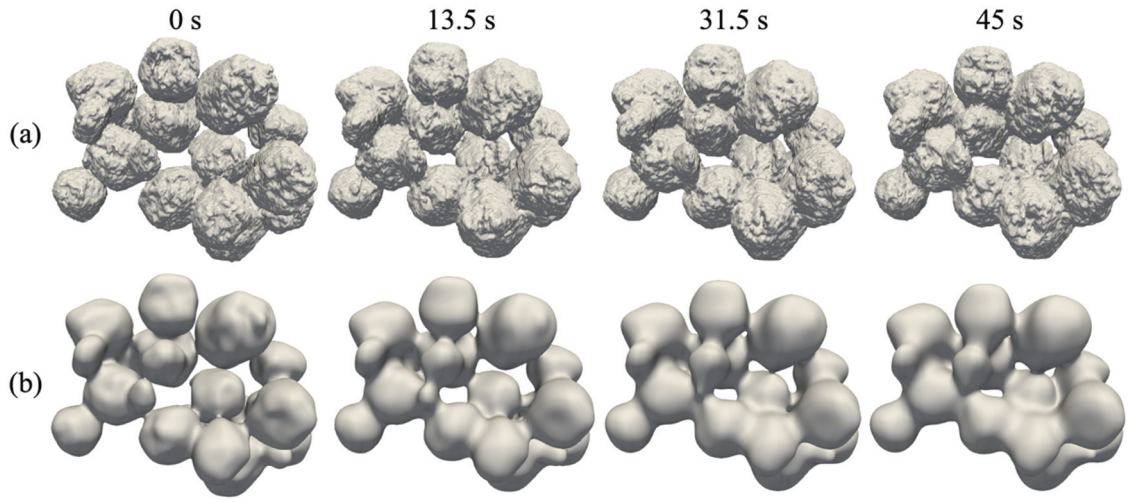

Figure 13. (a) Results of in situ observation of solid-state Cu nanoparticle sintering and (b) predictions obtained using phase-field simulation and optimally estimated parameters. The sintering time for each image (from left to right) are 0, 13.5, 31.5, and 45 s.

reproduction of the sintering behavior of Cu NPs obtained via in situ observation, we performed PF simulations of sintering using the optimally estimated parameters.

Figure 13a shows the 3D reconstruction of Cu NPs obtained via in situ observation (Section 3). The gaps between the NPs shrunk, and the system macroscopically densified. Figure 13b shows the PF simulation results obtained using the parameters optimally estimated through data assimilation. Although the sintering behavior simulated by using the PF model is similar to the experimentally observed one, the quantitative reproduction of necking behavior and particle size observed experimentally is not still realized. Inverse estimation of the material parameters, which are difficult to identify using conventional methods, could be conducted by directly using the time variation of the 3D morphology of Cu NPs obtained via in situ observation. This opens up a new way to clarify the unexplored aspects of the sintering mechanism in the synthesis of high-performance polycrystalline bulk superconducting materials.

4.4. Numerical simulation of solid-state sintering of Ba122 using the first principle calculation and PFM

The previous section shows that the PFM and data assimilation can be used to inversely estimate multiple material parameters included in a PF model from in situ observation results. However, data assimilation requires a time series of experimental observation data, which often necessitates special experimental instruments and advanced techniques. Furthermore, in situ observation of the sintering process of Ba122 superconducting materials has not been conducted because the doping elements in the superconducting material are easily vaporized. On the contrary, first-principles calculation, which is a representative atomistic numerical analysis method, can calculate the electronic state and physical property values of materials with high accuracy without needing experimental data. Therefore, in addition to data-driven modeling, where data assimilation is used, physics-driven modeling (which combines first-principles calculation and PF simulation) is useful. The difficulty of material parameter estimation increases with the number of parameters to be estimated, so the number of parameters to be estimated should be reduced through physics-driven modeling. In this section, we show the calculation results of Ba122's interfacial properties and their anisotropy, which we obtained by combining first-principles calculation and PF simulation. Furthermore, we show the PF simulation results of the solid-state sintering process of Ba122 considering the anisotropic interfacial properties of Ba122, which were obtained through the first-principles calculation.

4.4.1. PF model of solid-state sintering with anisotropic boundary properties

The PF model used here is similar to that described in Section 4.3.1. However, the anisotropic interfacial properties obtained from the first-principles calculation are introduced into the PF model [264]. The surface energy (γ_s) is defined as follows:

$$\gamma_s = \frac{\sum_i \eta_i \gamma_{s,i}(\theta_i, \varphi_i)}{\sum_i \eta_i}, \tag{6}$$

where $\gamma_{s,i}(\theta_i, \varphi_i)$ is the surface energy of the ith particle out of N, with its anisotropy corresponding to the surface orientation of the particle surface. θ_I and φ_i are the angles between the surface-normal direction of

the ith particle and the crystal coordinate system, respectively. The anisotropy of the surface energy is expressed by the following equation:

$$\gamma_{s,i}(\theta_i, \varphi_i) = k_0{}^s - k_1^s\left(n_{w,i}{}^s\right)^2 + k_2{}^s\left\{\left(n_{u,i}{}^s\right)^2 + \left(n_{v,i}{}^s\right)^2\right\}^2 + k_3{}^s\left(n_{u,i}{}^s\right)^2\left(n_{v,i}{}^s\right)^2, \quad (7)$$

where $\boldsymbol{n}_i^s = (n_{u,i}{}^s, n_{v,i}{}^s, n_{w,i}{}^s)$ is the unit vector representing the normal direction of the particle surface. $k_0{}^s$, $k_1{}^s$, $k_2{}^s$, and $k_3{}^s$ are the anisotropy coefficients, which are identified based on the results of the first-principles calculation, as shown in the next section. The GB energy (γ_{gb}) was modeled according to the literature [253,265]. The Read – Shockley equation [266] was used to calculate the dependence of the GB energy on crystallographic misorientation.

4.4.2. Calculation of anisotropic boundary properties of Ba122 using the first principle calculation

In the first-principles calculation, the interfacial properties were calculated using a slab model consisting of a large number of atomic layers and a vacuum region. The surface energy is calculated using the following equation:

$$\gamma = \frac{1}{2A}\left(E_{slab}{}^{relax} - nE_{slab}{}^{bulk}\right), \quad (8)$$

where $E_{\text{slab}}{}^{\text{relax}}$ and $E_{\text{slab}}{}^{\text{bulk}}$ are the total energy of the slab model after structural optimization and the total energy per unit cell of the bulk, respectively. A is the area of the upper and lower surfaces of the slab model, and the denominator 2 is placed because the slab model has two surfaces. n is the number of bulk unit cells in the slab model. Equation (8) represents the difference between the total energy of the slab model and the total energy of the bulk consisting of the same number of atoms as the slab model. For pure metals, surface energy can be obtained with high accuracy using Equation (8) [267,268]. For multisystem materials, such as Ba122, Equation (8) cannot be simply used because the slab model is not stoichiometric. In the following, the calculation method is detailed.

We describe the surface energy calculation for Ba122 using its (001) plane as an example. Figure 14a shows the crystal structure of Ba122, where Ba layers and FeAs layers are stacked alternately in the [001] direction (c-axis direction). Given the small interlayer bonding strength [269], we assumed that the (001) plane was formed by a cleavage between the Ba and FeAs layers. Therefore, the (001) surface was considered to have two kinds of surface structures: 'Ba-t' is terminated by the Ba layer, and 'As-t' is terminated by the As atoms in the FeAs layer. Figures 14b,c show the slab models for Ba-t and As-t.

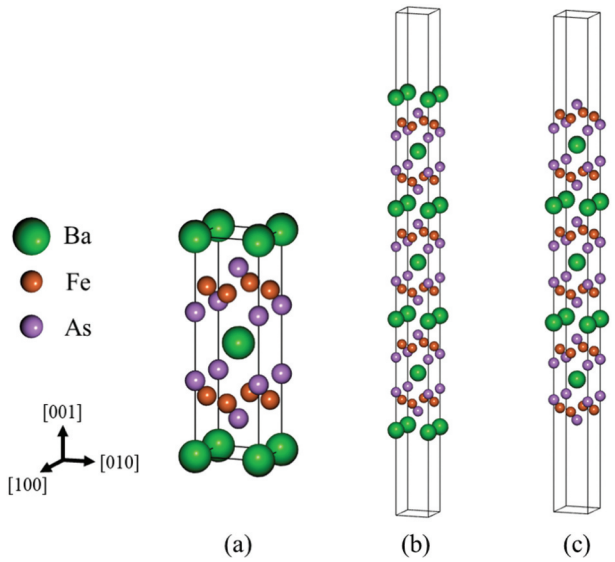

Figure 14. Schematic illustrations of Ba122: (a) unit cell, (b) (001) surface terminated by Ba layer (ba-t), and (c) (001) surface terminated by as layer (As-t) slab models. The green, orange, and purple balls represent Ba, Fe, and as atoms, respectively. The crystal structure of Ba122 consists of alternating Ba and FeAs layers in the [001] direction. These slab models have two equivalent surfaces and are nonstoichiometric.

These slab models have equivalent surface structures at the top and bottom edges and are symmetric with respect to the surface-normal direction. Because these slab models are not stoichiometric, the surface energy could not be calculated using Equation (8). Therefore, when nonstoichiometric slab models are used, the surface energy is calculated using the cleavage energy and the relaxation energy generated by the relaxation of near-surface atoms [270–272]. The cleavage energy is the energy required to cleave the bulk to create two surfaces. Therefore, for the two types of (001) surfaces (Ba-t and As-t), the cleavage energy is expressed by the following equation:

$$\gamma_{cleav} = \frac{1}{2A}\left(E_{slab}{}^{unrelax}(Ba) + E_{slab}{}^{unrelax}(As) - nE_{bulk}\right), \quad (9)$$

where $E_{\text{slab}}{}^{\text{unrelax}}(\alpha)$ is the total energy of the slab model of α-t (α = Ba, As) before structural optimization and n is the number of unit cells in the slab model. With the γ_{cleav} value given by Equation (9), the surface energy of the (001) plane of Ba-t and As-t can be calculated as follows:

$$\gamma_{DFT}(Ba) = \frac{1}{2}\gamma_{cleav} + E_{relax}(Ba), \quad (10)$$

$$\gamma_{DFT}(As) = \frac{1}{2}\gamma_{cleav} + E_{relax}(As). \quad (11)$$

Here, $E_{\text{relax}}(\text{Ba})$ and $E_{\text{relax}}(\text{As})$ represent the relaxation energy, which is calculated as follows:

$$E_{relax}(Ba) = \frac{1}{2A}\left(E_{slab}{}^{relax}(Ba) - E_{slab}{}^{unrelax}(Ba)\right), \tag{12}$$

$$E_{relax}(As) = \frac{1}{2A}\left(E_{slab}{}^{relax}(As) - E_{slab}{}^{unrelax}(As)\right), \tag{13}$$

where $E_{\mathrm{slab}}{}^{\mathrm{relax}}(\alpha)$ is the total energy of the slab model of α-t (α = Ba, As) after structural optimization. $E_{\mathrm{slab}}{}^{\mathrm{relax}}(\alpha)$ is the energy that decreases due to the relaxation of the surface structure after bulk cleavage (therefore, it has a negative value). As shown above, the surface energy can be obtained even for nonstoichiometric slab models using the cleavage and relaxation energies. In this study, we assumed that the GB energy anisotropy depending on inclination was proportional to the surface energy anisotropy.

To calculate the surface energies via first-principles calculation and incorporate them into the PFM model, we computed the surface energies for surfaces with various indices. However, the computational cost of plane-wave-based DFT calculation with a periodic boundary condition significantly increases due to the low symmetry of the atomic arrangement of high-index surfaces. Therefore, obtaining the surface energies of high-index surfaces to reduce computational costs is difficult. In this study, we calculated the surface energies of low-index surfaces: (001), (100), (110), and (011). Figure 15 shows the bulk and surface structures of Ba122 for which we calculated surface energies. In the slab model with the (001) surface, we considered the $\sqrt{2} \times \sqrt{2}$ structure observed in the experiment [273] in addition to systems with Ba-t and As-t structures. The $\sqrt{2} \times \sqrt{2}$ structure formed through the rearrangement of Ba atoms attached to the As-t side when Ba-t and As-t formed through Ba122 bulk cleavage. For the (100), (110), and (011) planes, the surface structures formed by the cleavage were considered, as experimental observations had not been reported. On the (100) surface, two kinds of BaFeAs-t formed through the bulk cleavage; they are denoted as BaFeAs-t(A) and BaFeAs-t(B) in this study. For the (011) surface, three patterns of surface structures were generated depending on the position of the Ba122 bulk cleavage. We denote the cleavage positions as (i), (ii), and (iii). In (iii), only one surface structure is shown because the two surface structures generated by the cleavage are equivalent. For the abovementioned bulk and slab models, structural optimization calculations were performed, and E_{bulk}, $E_{\mathrm{slab}}{}^{\mathrm{unrelax}}(\alpha)$, and $E_{\mathrm{slab}}{}^{\mathrm{relax}}(\alpha)$ (α = Ba, As) were calculated. In the structure optimization calculations for the bulk, the lattice constants were kept constant at the experimental values: $a = 3.9625$ Å and $c = 13.0168$ Å [274]). The coordinates of all atoms were optimized such that the

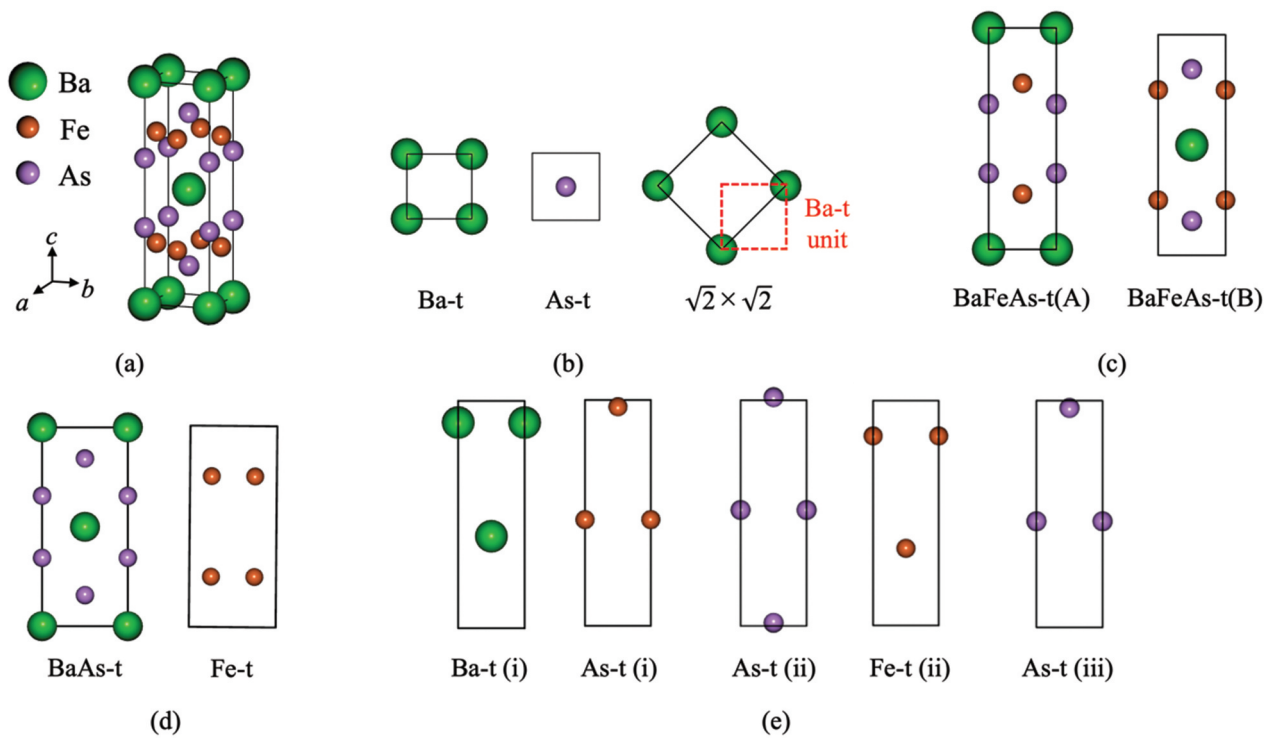

Figure 15. Schematic illustration and top views of Ba122: (a) bulk model and (b) (001), (c) (100), (d) (110), and (e) (011) planes. The green, orange, and purple balls represent Ba, Fe, and as atoms, respectively. The terminated structures of the (001) plane are Ba-t and As-t, resulting from cleavage and the reconstructed $\sqrt{2}\times\sqrt{2}$ structure [270]. In the (100), (110), and (011) planes, only cleavage structures are considered. (i), (ii), and (iii) denote the different cleavage modes.

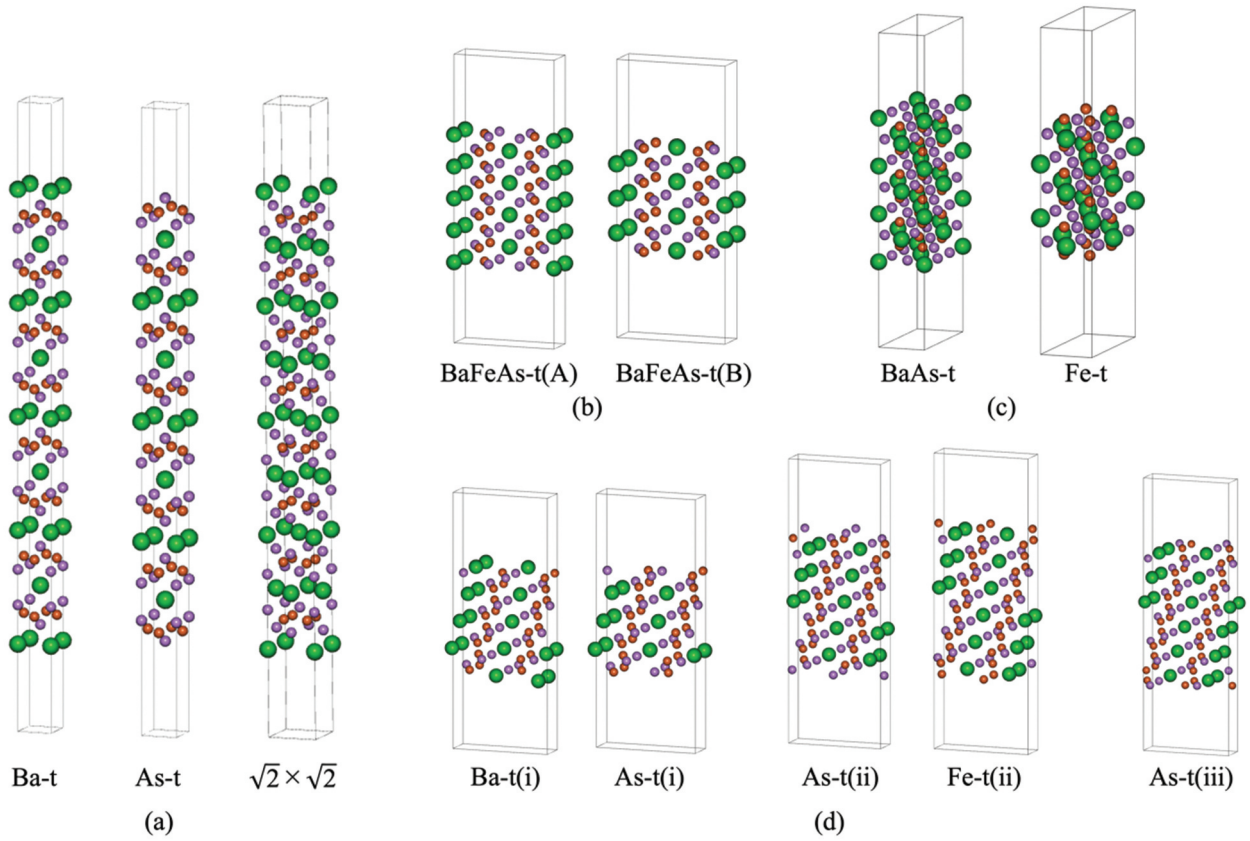

Figure 16. Slab models for (a) (001), (b) (100), (c) (110), and (d) (011) planes corresponding to Figure 15.

forces acting on each atom were less than 0.01 eV/Å^2. Figure 16 shows the slab models for each index surface in this study. These slab models were created using the experimental lattice constants [274] and the atomic coordinates obtained from the bulk structure optimization. The number of atomic layers was determined such that the total energy of the slab model converged with the thickness of the vacuum layer (20 Å). The in-plane atomic coordinates were optimized through the bulk structure optimization calculations, so the out-of-plane atomic coordinates were optimized for the slab model. In this study, we used the plane-wave-based ab initio calculation software VASP. Table 2 shows the computational conditions used in VASP.

Table 3 shows the cleavage energies (γ_{cleav}) and surface energies (γ_{DFT}) calculated via the first-principles calculation. For the (001) surface, the cleavage energy of the $\sqrt{2}\times\sqrt{2}$ surface structure was smaller than those of the Ba-t and As-t structures. This result was consistent with the experimental observation of the $\sqrt{2}\times\sqrt{2}$ structure [269], indicating the validity of the present calculation. Furthermore, this result meant

Table 2. Input parameters and methodologies used for self-consistent-field calculations and structural optimization of bulk and slab models of Ba122, as depicted in Figures 15 and 16. During bulk structural optimization, the atomic coordinates were optimized in all 3D directions. By contrast, for the slab models, the atomic coordinates were exclusively optimized in the out-of-plane direction.

Conditions	Methods and Values
Magnetization	Non-magnetic (non-spin polarization)
Lattice constant, *a* [Å]	3.9625 (= *b*) (57)
Lattice constant, *c* [Å]	13.0168 (57)
Length of vacuum region [Å]	20.0
Sampling k points	(001): $9\times9\times1$
	(100): $9\times3\times1$
	(110): $3\times7\times1$
	(011): $9\times3\times3$
Cutoff energy [eV]	800.0
Threshold energy of SCF [eV]	1.0×10^{-6}
Threshold force of structural optimization [eV/Å^2]	0.01
Smearing method	Methfessel-Paxton (2nd order) (Methfessel1989)
Smearing width [eV]	0.1
Exchange correlation functional	Perdew-Burke- Ernzerhof functional
Pseudopotential	Projector augmented wave potential

Table 3. Cleavage energy per unit area (g_{cleav}) and surface energy per unit area (g_{DFT}) of Ba122 surfaces obtained from first-principles calculation. The surface energy of the (001) plane was the smallest among the minimum values for the mirror indices, consistent with the Ba122 crystal structure. The values marked with asterisks (*) were used to identify the anisotropy function.

Miller index	Type	Cleavage energy, γ_{cleav} [J/m^2]	Surface energy, γ_{DFT} [J/m^2]
(001)	Ba-t	0.994	0.714
	As-t		0.912
	$\sqrt{2}\times\sqrt{2}$	0.783	0.547*
(100)	BaFeAs-t	1.385	1.309*
	BaFeAs-t		1.312
(110)	BaAs-t	1.458	1.421
	Fe-t		1.319*
(011)	Ba-t (i)	1.454	1.357
	Fe-t (i)		1.341
	Fe-t (ii)	2.180	1.859
	As-t (ii)		2.045
	As-t (iii)	1.272	1.213*

that the cleavage planes were more likely to have $\sqrt{2}\times\sqrt{2}$ surface structures than Ba-t and As-t. The minimum cleavage energies of the surface structures were in the following increasing order: (001), (011), (100), and (110). The surface energies were also in the following increasing order: (001), (011), (100), and (110). The difference between the surface energies of the (100) and (110) planes was 0.01 J/m^2. The relationship between the computed surface energies could be explained by the fact that Ba122 has a layered crystal structure stacked in the [001] direction and that the bonding forces between the layers are small.

Figure 17 shows the anisotropy function for the surface energy, $\gamma_i(\theta_{i,i})$, in a polar coordinate, as derived in this study. Here, we used the parameters for Equation (7), which were identified based on the surface energies listed in Table 3: $k_0^s = 0.905$, $k_1^s = 0.358$, $k_2^s = 0.404$, and $k_3^s = 0.004$. The surface plot of the anisotropy function shows the minimum surface energy in the (001) plane and the maximum one in the (110) plane. Furthermore, the surface energy decreased for the planes closer to the (001) surface. This was because the crystal structure of Ba122 is stacked in the [001] direction. Therefore, the physically reasonable anisotropy coefficients could be identified only from the surface energies of the four low-index planes: (001), (011), (100), and (110).

Using the identified anisotropy functions and their parameters, we performed a PF simulation of the polycrystal formation process during the solid-state sintering of Ba122 particles. Figure 18a shows the initial distribution of Ba122 particles using an isosurface of $\rho = 0.5$. The size of the computational domain was 51.2 μm × 51.2 μm × 12.8 μm. Within this computational domain, 732 spherical particles with a radius of 1.6 μm were placed in a hexagonal close-packed configuration. Figure 18b,c show the surface energy distribution in the initial state and the cross-sectional crystal orientation distribution at $z = 6.4$ μm. A random initial crystallographic orientation was set to investigate the crystallographic orientation and grain morphology of Ba122 particles that preferentially grew during the sintering process. The zero Neumann boundary condition was used for all planes. A time increment of 1.0×10^{-3} s was used to simulate 3000 s of the sintering process. As in the previous section, the anisotropy of the surface and GB energies was represented by the identified parameters, and the other parameters were as follows: $M_{vol} = 8.46\times10^{-23}$ m^5 J^{-1} s^{-1}, $M_{vap} = 8.46\times10^{-24}$ m^5 J^{-1} s^{-1}, $M_{surf} = 8.46\times10^{-21}$ m^5 J^{-1} s^{-1}, $M_{gb} = 8.46\times10^{-22}$ m^5 J^{-1} s^{-1}, and $M_\eta = 2.0\times10^{-8}$ m^3 J^{-1} s^{-1}.

Figure 19 shows the morphological changes of the sintered Ba122 particles. As the sintering

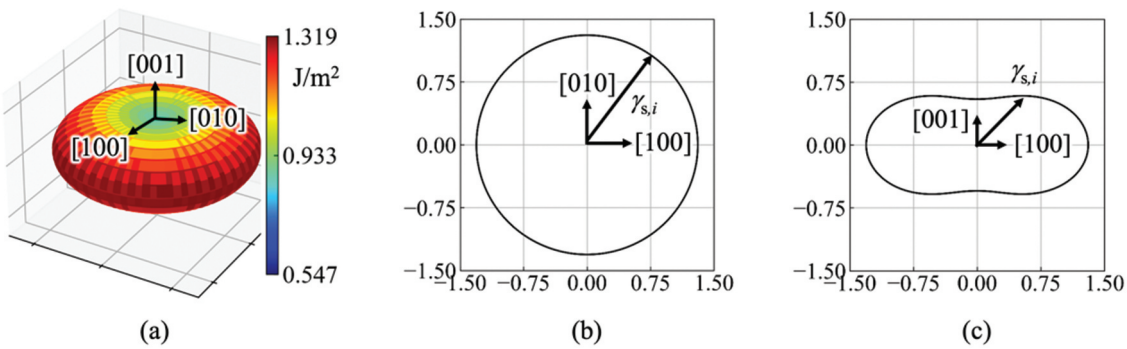

Figure 17. Anisotropy function of surface energy for Ba122 surfaces expressed by Equation (5). The anisotropy coefficients are $k_0^s = 0.905$, $k_1^s = 0.358$, $k_2^s = 0.404$, and $k_3^s = 0.004$.

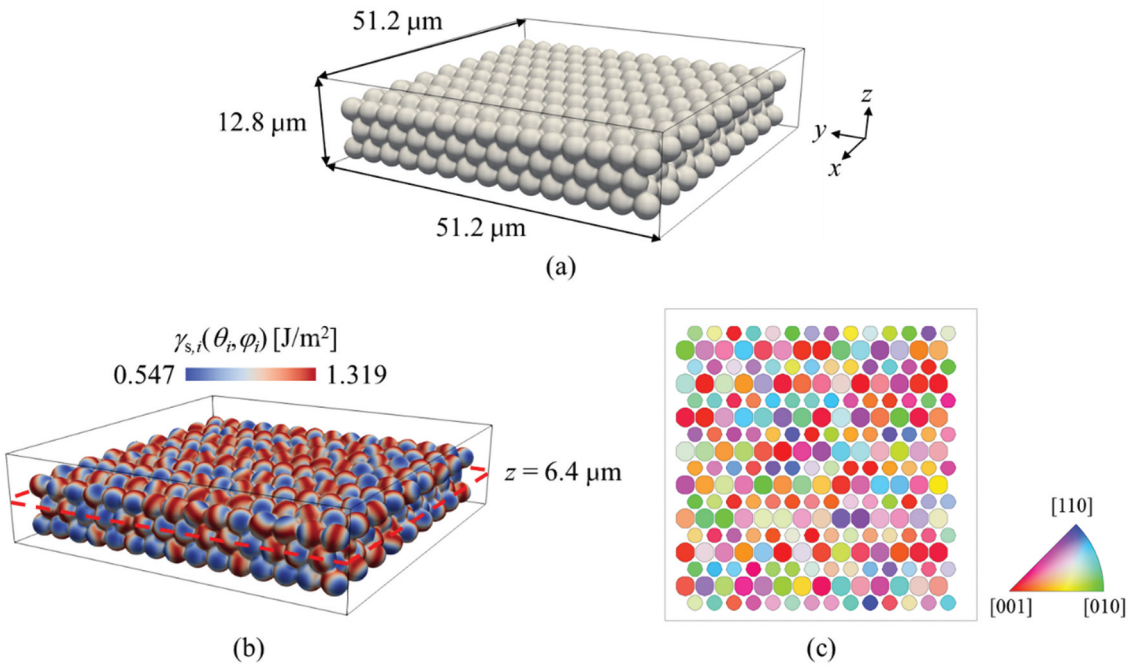

Figure 18. Initial distributions of multi-Ba122 particles: (a) $\rho = 0.5$ isosurface, (b) surface energy distribution, and (c) crystal orientation (electron backscatter diffraction – inverse pole figure map) in $z = 6.4$ μm cross section. The Ba122 particles are in a hexagonal close-packed configuration, and the initial crystal orientations are assigned randomly.

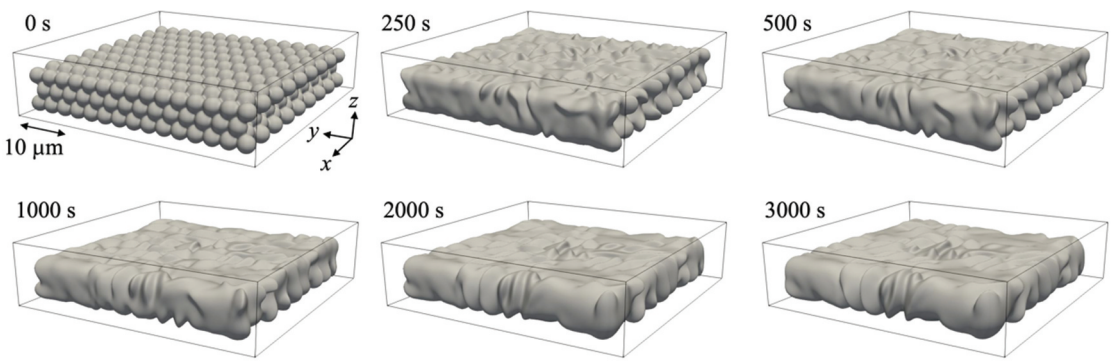

Figure 19. Time evolutions of isosurface $\rho = 0.5$ obtained from phase-field simulation using multi-Ba122 particles.

progresses, the Ba122 particles contact each other and grow, densifying the system. Based on the convex hull method, the volume of the system after the sintering was reduced by about 8.9% compared to the initial volume. Furthermore, the particles form both smooth and convex morphologies. Figure 20a shows the GB distribution and crystallographic orientation at the $z = 6.4$ μm cross section. As the sintering progresses, grains connected and grew, decreasing the number of grains. Figure 20b shows the area distribution of the crystallographic orientation of the Ba122 grains at the $z = 6.4$ μm cross section, elucidating the crystallographic orientation of the preferentially grown Ba122 particles. The Ba122 particles with a crystallographic orientation close to the [001] direction, which were relatively abundant in the initial stage of sintering, gradually disappeared. Thus, the sintering progressed such that the surfaces with large GB energies disappeared.

This section shows the results of solid-state sintering simulations of Ba122 using a PF model that implements the anisotropy of surface and interface energies, which were identified via first-principles

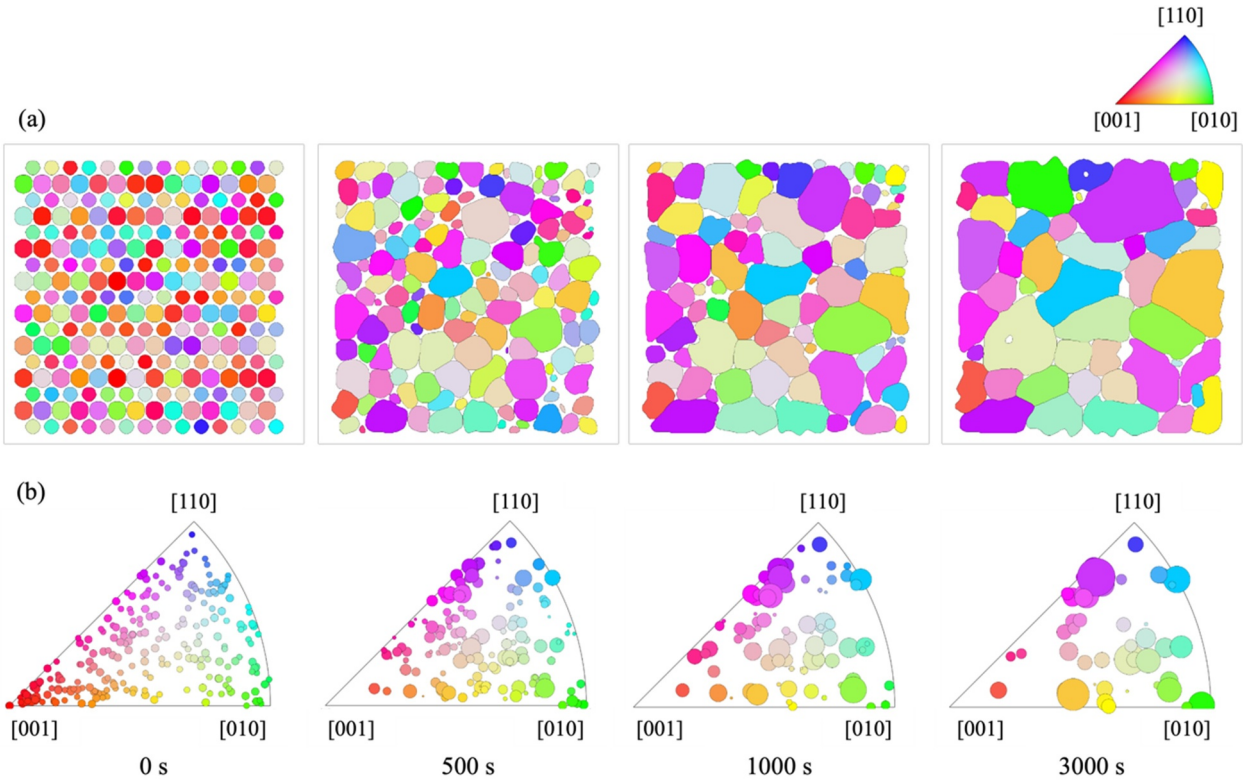

Figure 20. Time evolutions of (a) crystal orientation (electron backscatter diffraction – inverse pole figure [IPF] map) in $z = 6.4$ μm cross section, and (b) distribution of area of grains in IPF color map obtained from phase-field simulation using multi-Ba122 particles.

calculation. Further identification of other parameters, such as GB mobility, is needed to enhance simulation accuracy. In the future, the formation of the polycrystalline structure of Ba122 can be predicted with high accuracy using both data- and physics-driven modeling.

5. Data-driven process design

In recent years, machine learning has been integrated with materials science to solve various problems, such as the modeling of superconductor T_c through database analysis [212,275–284] and the tuning of material properties [20,145,215,285,286]. In addition to advances in data and computational science, these developments have been underpinned by high-quality, large-scale databases, such as the Materials Project [287], which is a component of the Materials Genome Initiative for accelerated materials design, and MDR SuperCon [288], which is a numerical data sheet for superconducting materials made public by the National Institute for Materials Science. Compared with the data-driven search for new materials, the application of machine learning to processes has been somewhat limited. This is partly because process conditions vary according to equipment and environment, and include many parameters and human tacit knowledge. Although attempts are being made to construct databases using advanced methods, such as data mining [289–291], Bayesian optimization [285,292] (Section 5.1) is attracting attention for facilitating data-driven process design from a relatively small number of data.

5.1. Bayesian optimization and software (BOXVIA)

Bayesian optimization is widely used in materials informatics, which aims to discover novel materials using computational materials science [293]. Bayesian optimization is an effective method in process informatics, which aims to optimize the process conditions for creating a desired material [285]. Process informatics using Bayesian optimization aims to maximize or minimize an objective function, which is a function of experimental conditions. In the process design shown in the following section, the objective function is the critical current density (J_c). In practical processes, however, the objective function is often a black-box function, which contains many unknown parameters. Bayesian optimization enables us to find the optimal experimental conditions that minimize or maximize the objective function without defining a specific equation for the function. Bayesian optimization describes the objective function in terms of a Gaussian distribution.

$$f(\boldsymbol{p})\left(\mu(\boldsymbol{p}), \sigma^2(\boldsymbol{p})\right), \tag{14}$$

where $f(\boldsymbol{p})$, $\mu(\boldsymbol{p})$, and $\sigma^2(\boldsymbol{p})$ are the objective function, mean function, and variation, respectively [216]. $\boldsymbol{p}$ is a vector containing the experimental conditions. The optimal experimental conditions were searched by evaluating an acquisition function, which is calculated using $\mu(\boldsymbol{p})$ and $\sigma(\boldsymbol{p})$. In this study, the acquisition function called the expected improvement [294] was adopted. The experimental conditions were optimized using iterative calculation using Gaussian process regression.

Various computational tools have been developed to perform Bayesian optimization, but they require programming techniques. Thus, Bayesian optimization remains challenging for researchers and engineers specializing in experimental studies. Moreover, few dedicated software has been developed for materials and process informatics. Therefore, we developed BOXVIA, a Bayesian optimization software that does not require specialized programming [215]. BOXVIA is available in a GitHub repository (https://yamanaka-lab-tuat.github.io/BOXVIA/) and has manuals and tutorials. In the next section, we show the results of process design using BOXVIA.

5.2. Researcher- and data-driven process design

This section discusses a recent work on synthesis process design that combines researchers' experience, idea-based approach, and AI-based approach using machine learning [20]. According to the framework shown in Figure 21, researchers provide AI with a process search space and initial data through a strategy based on researchers' experience and theory, and AI performs machine learning on the data to predict the synthesis conditions that will result in superior properties. Researchers synthesize samples, performs measurements, and updates the database according to the proposed conditions. The AI approach iterates a data-driven loop, which advances balanced global exploration and local optimization based on Bayesian optimization. Simultaneously, researchers analyze a shared database containing data from the data-driven loop, plan the next process, and synthesize samples (researcher-driven loop). These independent loops work in concert, allowing researchers to remove biases and broaden their horizons easily. For AI, the collaborative framework expands the data to be machine learned so that AI can learn to include high-quality data that has been roughly optimized by researchers to enhance process design efficiency.

This researcher- and data-driven process design was implemented as follows to increase the critical current density of K-doped Ba122 polycrystalline bulks. The researcher-driven approach incorporated previously known theories, information, and experiences, such as knowledge on microscopic current transport at GBs [19,294], deep learning analysis of microstructures [17], and formation process simulations [256–258,264], into the design guidelines. The AI approach used was based on Bayesian optimization and BOXVIA, which was customized for process design. Based on a small number of preliminary data, J_c as the objective parameter was optimized as a function of three synthesis process parameters (ramping rate, maximum temperature, dwell time), and a high J_c of above 10^5 A/cm^2 was obtained for K-doped Ba122 polycrystalline bulks.

6. Magnet property

This section reviews the general feature of the superconducting bulk magnets (Section 6.1) and the performance of the IBS bulk (Section 6.2), which was

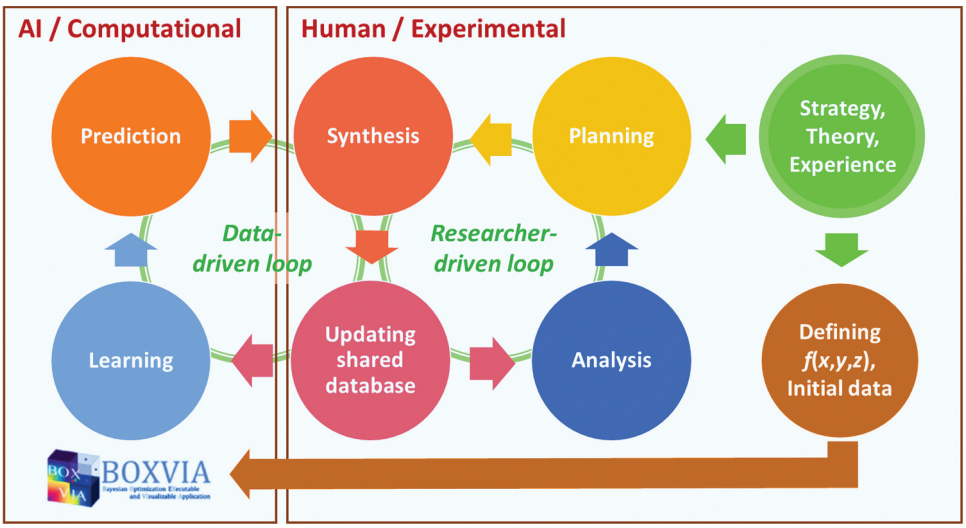

Figure 21. Framework for researchers and artificial intelligence to design processes independently while sharing same experimental data [20].

demonstrated as a proof of concept for the researcher- and data-driven process design.

6.1. Superconducting bulks

The closed superconducting current loop, which can be induced by magnetization, is the origin of the magnetic field in superconducting bulk magnets. Superconducting current does not decay due to the zero resistance, so a superconducting bulk behaves like a permanent magnet under cooling. The energy density of the superconducting current circulating in a superconducting bulk magnet is more than 100 times that of copper, and the irreversible field, which is the upper limit of the trapped magnetic field, is 10 times the saturation magnetization of a ferromagnetic permanent magnet, making it a compact yet powerful magnet. The maximum magnetic field trapped in a cylindrical superconducting bulk magnet is

$$B_{\mathrm{T}} = A\mu_0 J_{\mathrm{c}}^{\mathrm{global}} r \tag{15}$$

and proportional to the product of $J_{\mathrm{c}}^{\mathrm{global}}$, the radius ($r$), and geometrical factor (A).

Research on superconducting bulks has considerably advanced in REBCO since the discovery of high-T_{c} cuprate superconductors. A melt growth process using seed crystals as nuclei has been developed [49–53], and magnetic field trapping of more than 17 T has been achieved in a quasi-single-crystal bulk of several centimeters in size [295]. Recent topics include the improvement of magnetic flux pinning forces [296,297] and mechanical strength [297,298]; joining [299–303]; pulsed-field magnetization [304]; and finite element modeling of electromagnetic, thermal, and mechanical behaviors [305–307]. 'Pseudo-bulks' have also been developed, in which REBCO-coated conductors cut into squares or other shapes are stacked and magnetized to form strong magnets [308–311].

As new types of superconducting bulks, polycrystalline-based superconducting bulk magnets have attracted attention in recent years. Polycrystalline superconducting bulk magnets were developed using MgB_2, and magnetic fields of several tesla can be obtained via cryocooling owing to its 40 K class high-T_{c} [249,312–316]. Being a polycrystalline material, it can be fabricated simply through powder mixing, molding, and heat treatment and is therefore expected to be large in size. In addition, the microstructure of small, randomly oriented grains produces a uniform distribution of the trapped magnetic field and strong flux pinning throughout a sample [312]. Microstructure control [317,318] and flux pinning control [217,319–321] to improve trapped-field strength, levitation characteristics [322], shielding characteristics [323], pulse magnetization [324], and modeling [325–327] are being investigated.

In IBSs, a small size 1 T bulk magnet was fabricated by Weiss *et al* using K-doped Ba122 [128], followed by larger bulks fabricated in Ba122 [20,80,328] and 1144 [182] phases. Recently, prototype coil magnets and magnetic field generation have been actively pursued [80,130,210,329–332]. Ding *et al* reported the fabrication of pancake coils with six stacked, achieving a current of 84 A at 4.2 K in a background field of 20 T [210]. Pyon, Tamegai *et al* fabricated Na-doped Ba122 monocore and K-doped Ba122 seven-core round wires with I_{c} values of 30 and 18 A and magnetic fields of 0.175 and 0.1 T, respectively [80,130,331,332].

6.2. K-doped Ba122 bulk magnets

This section presents the magnet properties of the K-doped Ba122 bulk magnets obtained through the researcher- and data-driven process design described in Section 5.2. The optimal synthesis process conditions were determined by researchers and AI, and two disk-shaped bulk magnets were synthesized under these conditions. After being magnetized externally while being cooled below the transition temperature (38 K) by a compact cryocooler, the bulks had a trapped magnetic field of over 2 T once external field was removed. Figure 22 shows a magnetic hysteresis loop acquired at 5 K after the zero-field cooling of the bulk pair while the external magnetic field was swept at a rate of 4.8 T/h. With an external field of ~ 2.5 T, the flux reached the center of the bulk pair. At 6 T, the hysteresis loop remained open due to the robust flux pinning and high irreversibility field. With

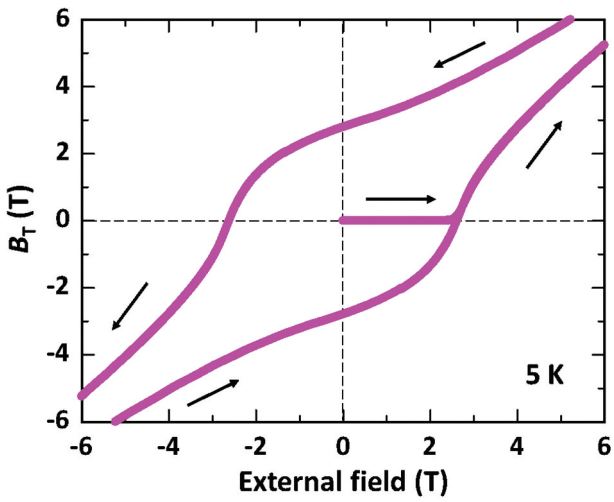

Figure 22. Magnetic hysteresis loop of K-doped Ba122 bulk pair. The hysteresis loop was obtained by cooling the sample down to 5 K under a zero magnetic field, followed by a gradual increase in the external magnetic field from 0 T to 7 T, followed by a decrease from 7 T to – 7 T and another increase from – 7 T to 7 T (indicated by arrows) [20].

decreasing the external magnetic field, the bulk pair trapped ~ 2.8 T under zero field. The measured trapped field is about 2.7 times higher than the previous trapped field record of 1.03 T achieved using iron-based superconducting magnets reported by Weiss *et al.* [128]. From Equation (15), the trapped field of a superconducting bulk depends on its size and current density. Considering the relatively small size of this prototype magnet (3 cm in diameter) and the rather flat J_c-H characteristics of the IBSs, stronger trapped field can be expected for a larger size magnet [328]. In particular, since magnetic fields of more than 1 T are maintained up to ~ 18 K in the bulk pair [20], strong magnet applications in the 10–20 K range can be anticipated. This 10–20 K temperature range can be operated with higher thermal stability using compact cryocoolers compared to lower temperature. As this temperature range is close to the boiling point of liquid hydrogen (about 20 K), liquid hydrogen cooling could be considered for practical iron-based superconducting magnets.

7. Summary and perspectives

Focusing on the grain, grain boundary and microstructure of polycrystalline materials, this review introduced a new style of material development through the fusion of experimentation and computational science, using the development of iron-based high-temperature superconducting polycrystalline magnets as an example. The following topics: advanced processing methods; multidimensional microstructural acquisition using advanced electron microscopy; modelling of microstructural formation using data assimilation; 3D reconstruction and modelling transport properties using deep learning; understanding grain boundary transport by developing artificial single grain boundary; and researchers- and data-driven process design that incorporate these findings were presented. The suite of methods presented in this review utilizes emerging data science techniques, and is applicable not only to the superconducting materials presented in this paper, but also to a wide variety of metallic and ceramic polycrystalline materials. This section summarizes perspectives and key issues for IBSs, processing, characterization, and machine learning integration in polycrystalline materials research.

- **Iron-based superconductors**: The microstructure of the demonstrated K-doped Ba122 superconducting bulk magnet consists of a randomly oriented polycrystalline material, which differs from REBCO high-temperature superconductors. The production of polycrystalline superconductor could be efficiently scaled through conventional ceramic processes, aided by the straightforward predictability and optimization achievable using numerical models. Given that IBSs exhibit small electromagnetic anisotropy and a very high upper critical field well above 50 T, which is more than twice that of conventional Nb-based superconductors, IBSs show great potential as pioneering, next-generation strong magnets suitable for practical applications. This potential extends to challenging environments such as liquid hydrogen cooling (~20 K). Recent progress of machine learning application on IBSs, such as predicting the critical temperature [333–337], imaging superconducting vortices [338], modeling microstructure/defect/chemical composition [17,145,339] and data-driven process design [20,215], would accelerate the future research and development.
- **GBs**: Atomic-scale GB structural observation is necessary to understand the relationship between GBs and superconducting properties. Creating artificial GBs with large misorientation angles in K-doped Ba122 is currently not achieved due to its healing effect. A GB relaxation structure naturally forms near a GB because of the accumulation of small angle shifts. In Fe(Se,Te), a Σ9 GB is formed in the CeO_2 buffer layer for larger GB angles. The orientation along the CeO_2 GB is parallel to the [100] crystal axis of Fe(Se,Te), and no GBs form in Fe(Se,Te). In both cases, the superconducting current at the GBs does not attenuate, which is a positive result. The impact of grain boundaries with large misorientation angles on superconducting currents should be experimentally confirmed for both K-doped Ba122 and Fe(Se,Te).
- **In situ electron microscopy observation**: Limitations hinder the determination of how a microstructure forms during a fabrication process using conventional snapshots of electron microscopy images. By contrast, in situ electron microscopy observation of microstructural evolution can directly answer these questions and is useful for the microstructural design of polycrystalline materials, which may involve grain nucleation and growth, sintering, and phase transformation. In addition, PF modeling and in situ electron microscopy observation data can be assimilated to evaluate the physical properties (e.g. diffusion coefficients in nanostructured materials) required to reproduce microstructure formation. Such assimilation is expected to become an effective tool for clarifying the optimal approach to microstructure control for practical applications of polycrystalline materials. The lack of reports on the application of in situ electron microscopy to Ba122 materials is probably due to experimental difficulties. Possible reasons for the lack of reports

on in situ electron microscopy for Ba122 would be the following: the synthesis of Ba122 requires more than three elements including dopant elements; the high volatility of the constituent elements (such as potassium); the possibility that the raw material powders will react with each other unevenly on the micrometer-to-nanometer-scale. Therefore, it could be a first step to apply in situ electron microscopy to the sintering and coarsening process of Ba122 particles after the synthesis of the Ba122 phase is completed.

- **Microstructural formation modeling**: Significant progress has been achieved in the use of data- and physics-driven modeling approaches to predict polycrystalline microstructural evolution in superconducting materials, especially Ba122 polycrystalline materials. However, many unknown physical properties, material parameters, and sintering mechanisms for superconducting materials remain unknown. Therefore, continuous collection of fundamental data for superconducting materials is expected for the research community.
- **Microstructure driven**: Implementing process informatics based on microstructural data requires collaboration between process, measurement, and data scientists and a multi-angled method for extracting large amounts of quantitative data from a small number of experiments in electron microscopy, which incurs high experimental costs. Furthermore, it requires data scientific assistance that can manage a small amount of data. In the data analysis, it will also be necessary to find complex correlations among microstructures, properties, and processes using machine learning, such as regression analysis, from perspectives that researchers would not have thought of on their own.
- **Process informatics**: The complex, multifaceted landscape of synthesis presents clear challenges that require further exploration and innovation to develop new models and databases, including linkages with equipment and data formats. Human-in-the-loop will be important for ceramic materials research, a field where researchers have an advantage over AI due to their vast amounts of accumulated experience and know-how. Close collaboration and practice between researchers in experiments and machine learning is effective in producing powerful AI models, so fostering such a cooperative environment is crucial. Generative AI can also be an innovative technology, but the means by which this technology can be adopted and utilized will be a challenge.

Acknowledgments

This work was supported by JST CREST (JPMJCR18J4). A. Yamamoto thanks Dr. S. Tokuta, Prof. M. Naito, Dr. D. Qin, Mr. Y. Hirabayashi, Mr. H. Iga, Mr. H. Ogawa of TUAT for fruitful discussion and providing data and JSPS KAKENHI (JP21H01615 and JP18H01699) and the Collaborative Research Projects of Laboratory for Materials and Structures, Institute of Innovative Research, Tokyo Institute of Technology. A. Yamanaka thanks Dr. A. Ishii and Mr. K. Kondo for their sincere cooperation on data assimilation-integrated phase-field modeling and first-principles calculations. K. I. thanks Dr. J. Hänisch, Profs. T. Hatano and H. Ikuta for their invaluable contributions and discussion, and JSPS KAKENHI (JP20H02681). Y. S. thanks Nanotechnology Platform (A-18-TU-0037) of the MEXT, Japan. S. H. thanks Dr. Z. Guo, Mr. K. Muraoka, Mr. T. Harada, Ms. H. Shi, Mr. K. Wada, Mr. Y. Ma, Dr. H. Gao, Dr. C. Wang, Dr. M.R.U.K. Khan, Assist. Prof. S. Ihara, Assoc. Prof. H. Saito and Prof. M. Murayama of Kyushu University for their sincere cooperation on electron microscopy observations and analyses for microstructural characterizations.

Disclosure statement

No potential conflict of interest was reported by the author(s).

Funding

The work was supported by the Japan Science and Technology Corporation [JPMJCR18J4].

ORCID

Akiyasu Yamamoto http://orcid.org/0000-0001-6346-3422
Akinori Yamanaka http://orcid.org/0000-0002-1781-8330
Kazumasa Iida http://orcid.org/0000-0003-1038-9630
Yusuke Shimada http://orcid.org/0000-0003-0348-2765
Satoshi Hata http://orcid.org/0000-0001-6030-8363

Author contributions

A. Yamamoto wrote 2.1, 2.4, 5.2, 6 and abstract. A. Yamanaka wrote 4.3, 4.4 and 5.1. K.I. wrote 2.2 and 2.3. Y.S. wrote 3.1, 4.1 and 4.2. S. H. wrote 1 and 3.2. All authors contributed to 7.

References

[1] Yamakoshi K, Ohno Y, Kutsukake K, et al. Multicrystalline informatics applied to multicrystalline silicon for unraveling the microscopic root cause of dislocation generation. Adv Mater. 2024;36 (8):2308599. doi: 10.1002/adma.202308599
[2] Liu Y, Zhao T, Ju W, et al. Materials discovery and design using machine learning. J Materiomics. 2017;3 (3):159–177. doi: 10.1016/j.jmat.2017.08.002
[3] Mobarak MH, Mimona MA, Islam MA, et al. Scope of machine learning in materials research—a review. Appl Surf Sci Adv. 2023;18:100523. doi: 10.1016/j.apsadv.2023.100523
[4] Ng WL, Goh GL, Goh GD, et al. Progress and opportunities for machine learning in materials and

processes of additive manufacturing. Adv Mater. 2024;36(34):2310006. doi: 10.1002/adma.202310006
[5] Zhichao L, Dong M, Xiongjun L, et al. High-throughput and data-driven machine learning techniques for discovering high-entropy alloys. Commun Mater. 2024;5(1):76. doi: 10.1038/s43246-024-00487-3
[6] Savitzky BH, Zeltmann SE, Hughes LA, et al. py4DSTEM: a software package for four-dimensional scanning transmission electron microscopy data analysis. Microsc Microanal. 2021;27(4):712–743. doi: 10.1017/s1431927621000477
[7] Ghauri H, Tafreshi R, Mansoor B. Toward automated microstructure characterization of stainless steels through machine learning-based analysis of replication micrographs. J Mater Sci: Mater Eng. 2024;19(1):4. doi: 10.1186/s40712-024-00146-y
[8] Fowler JE, Ruggles TJ, Cillessen DE, et al. High-throughput microstructural characterization and process correlation using automated electron backscatter diffraction. Integr Mater Manuf Innov. 2024;3(3):641–655. doi: 10.1007/s40192-024-00366-2
[9] Simons H, Jakobsen AC, Ahl SR, et al. Multiscale 3D characterization with dark-field x-ray microscopy. MRS Bull. 2016;41(6):454–459. doi: 10.1557/mrs.2016.114
[10] Kaira CS, Kantzos C, Williams JJ, et al. Microstructural evolution and deformation behavior of Al-cu alloys: a transmission X-ray microscopy (TXM) and micropillar compression study. Acta Materialia. 2018;144:419–431. doi: 10.1016/j.actamat.2017.11.009
[11] Hata S, Furukawa H, Gondo T, et al. Electron tomography imaging methods with diffraction contrast for materials research. Microscopy. 2020;69(3):141–155. doi: 10.1093/jmicro/dfaa002
[12] Mayer J, Barthel J, Vayyala A, et al. The TOMO project – integrating a fully functional atom probe in an aberration-corrected TEM. Microscopy and Microanal. 2023;29(Supplement_1):593–594. doi: 10.1093/micmic/ozad067.286
[13] Spurgeon SR, Ophus C, Jones L, et al. Towards data-driven next-generation transmission electron microscopy. Nat Mater. 2021;20(3):274–279. doi: 10.1038/s41563-020-00833-z
[14] Hosono H, Yamamoto A, Hiramatsu H, et al. Recent advances in iron-based superconductors toward applications. Mater Today. 2018;21(3):278–302. doi: 10.1016/j.mattod.2017.09.006
[15] Shimada Y, Tokuta S, Yamanaka A, et al. Three-dimensional microstructure and critical current properties of ultrafine grain Ba(Fe,Co)2As2 bulk superconductors. J Alloys And Compd. 2022;923:166358. doi: 10.1016/j.jallcom.2022.166358
[16] Ihara S, Yoshinaga M, Miyazaki H, et al. In situ electron tomography for the thermally activated solid reaction of anaerobic nanoparticles. Nanoscale. 2023;15(23):10133–10140. doi: 10.1039/D3NR00992K
[17] Hirabayashi Y, Iga H, Ogawa H, et al. Deep learning for three-dimensional segmentation of electron microscopy images of complex ceramic materials. Npj Comput Mater. 2024;10(1):46. doi: 10.1038/s41524-024-01226-5
[18] Ishii A, Yamanaka A, Yoshinaga M, et al. High-fidelity phase-field simulation of solid-state sintering enabled by bayesian data assimilation using in situ electron tomography data. Acta Mater. 2024;278:120251. doi: 10.1016/j.actamat.2024.120251
[19] Hatano T, Qin D, Iida K, et al. High tolerance of the superconducting current to large grain boundary angles in potassium-doped BaFe2As2. NPG Asia Mater. 2024;16(1):41. doi: 10.1038/s41427-024-00561-9
[20] Yamamoto A, Tokuta S, Ishii A, et al. Superstrength permanent magnets with iron-based superconductors by data- and researcher-driven process design. NPG Asia Mater. 2024;16(1):29. doi: 10.1038/s41427-024-00549-5
[21] Hilgenkamp H, Mannhart J. Grain boundaries in high-tc superconductors. Rev Mod Phys. 2002;74(2):485–549. doi: 10.1103/RevModPhys.74.485
[22] Goyal A, Norton DP, Budai JD, et al. High critical current density superconducting tapes by epitaxial deposition of YBa2Cu3Ox thick films on biaxially textured metals. Appl Phys Lett. 1996;69(12):1795–1797. doi: 10.1063/1.117489
[23] Iijima Y, Tanabe N, Kohno O, et al. In-plane aligned YBa2Cu3O7−x thin films deposited on polycrystalline metallic substrates. Appl Phys Lett. 1992;60(6):769–771. doi: 10.1063/1.106514
[24] Wang QF, Jiang P, Li M, et al. Temperature dependence of transport critical current density for REBCO superconducting tapes deposited by MOCVD. Superconductor Sci and Technol. 2024;37(1):015006. doi: 10.1088/1361-6668/ad0db5
[25] Barusco P, Giguère J, Lacroix C, et al. A sulfurization method for creating the buffer-layers current flow diverter architecture in REBa2Cu3O7 coated conductors. Supercond Sci Technol. 2023;36(12):125005. doi: 10.1088/1361-6668/ad01ec
[26] Huang RT, Chen J, Liu ZY, et al. Monodisperse BaZrO3 nanocrystals and flux pinning effect on upscaling mod-derived (Y,Dy)Ba2Cu3O7−δ superconducting tapes. Supercond Sci Technol. 2023;36(12):125002. doi: 10.1088/1361-6668/acff25
[27] Walter K, Erbe M, Welle A, et al. Precise determination of oxygen content in SmBa2Cu3O−δ thin film samples using x-ray diffraction. Supercond Sci Technol. 2024;37(7):075002. doi: 10.1088/1361-6668/ad4a30
[28] Paidpilli M, Sandra JS, Sarangi B, et al. High-current, double-sided REBCO tapes by advanced MOCVD. Supercond Sci Technol. 2023;36(9):095016. doi: 10.1088/1361-6668/ace8c8
[29] Wang MQ, Huang DX, Wang TX, et al. Unlocking the performance evolution of GdBCO coated conductors irradiated by deuterium plasma. Supercond Sci Technol. 2024;37(5):055006. doi: 10.1088/1361-6668/ad3c9d
[30] Krkotic P, Traver O, Tagdulang N, et al. Performance of high-temperature superconducting REBCO coated conductors under synchrotron irradiation for future circular colliders. Supercond Sci Technol. 2023;36(10):105009. doi: 10.1088/1361-6668/acf001
[31] Kase J, Morimoto T, Togano K, et al. Preparation of the textured bi-based oxide tapes by partial melting process. IEEE Trans Magn. 1991;27(2):1254–1257. doi: 10.1109/20.133412
[32] Sato K, Hikata T, Mukai H, et al. High-JC silver-sheathed bi-based superconducting wires. IEEE Trans Magn. 1991;27(2):1231–1238. doi: 10.1109/20.133408

[33] Kobayashi S, Kato T, Yamazaki K, et al. Controlled over pressure processing of Bi2223 long length wires. IEEE Trans Appl Supercond. 2005;15(2):2534–2537. doi: 10.1109/tasc.2005.847520
[34] Larbalestier DC, Jiang J, Trociewitz UP, et al. Isotropic round-wire multifilament cuprate superconductor for generation of magnetic fields above 30 T. Nat Mater. 2014;13(4):375–381. doi: 10.1038/nmat3887
[35] Malagoli A, Lee PJ, Ghosh AK, et al. Evidence for length-dependent wire expansion, filament dedensification and consequent degradation of critical current density in Ag-alloy sheathed Bi-2212 wires. Supercond Sci Technol. 2013;26(5):055018. doi: 10.1088/0953-2048/26/5/055018
[36] Shen TM, Fajardo LG, Myers C, et al. Design, fabrication, and characterization of a high-field high-temperature superconducting Bi-2212 accelerator dipole magnet. Phys Rev Accel Beams. 2022;25(12):122401. doi: 10.1103/PhysRevAccelBeams.25.122401
[37] Jiang JY, Hossain SI, Barua S, et al. Performance and microstructure variation with maximum heat treatment temperature for recent Bi-2212 round wires. IEEE Trans Appl Supercond. 2023;33(5):1–5. doi: 10.1109/tasc.2023.3236870
[38] Tarantini C, Oloye TA, Hossain SI, et al. Ac susceptibility studies of intra- and intergrain properties of high-Jc Bi-2212 wires. Phys Rev Mater. 2023;7(1):014802. doi: 10.1103/PhysRevMaterials.7.014802
[39] Xu AX, Jiang JY, Tarantini C, et al. Flux pinning enhancement of Bi-2212 tapes by increasing Sr content. IEEE Trans Appl Supercond. 2024;34(3):1–5. doi: 10.1109/tasc.2023.3345293
[40] Tarantini C, Barua S, Oloye TA, et al. Variation of effective filament diameter, irreversibility field, anisotropy, and pinning efficiency in Bi-2212 round wires. Supercond Sci Technol. 2024;37(1):015021. doi: 10.1088/1361-6668/ad13b2
[41] Ali MA, Karan SM, Roy N, et al. Impact of Co2C nanoparticles on enhancing the critical current density of Bi-2223 superconductor. AIP Adv. 2024;14(3):035110. doi: 10.1063/5.0191262
[42] Hao QB, Jiao GF, Xu XY, et al. Improvement of plastic deformation property and current carrying capacity of Bi2212 wires through low oxygen partial pressure post-annealing of precursor. Surfaces Interface. 2024;49:104463. doi: 10.1016/j.surfin.2024.104463
[43] Liu XQ, Gao Y, Li H, et al. Density dependent constitutive model for Bi-2212 powder compression deformation. Phys Scr. 2024;99(6):065950. doi: 10.1088/1402-4896/ad4686
[44] Traverso A, Leveratto A, Armenio AA, et al. Analysis of the flattening on Bi-2212 wires due to the cabling process and its effect on their performances. IEEE Trans Appl Supercond. 2024;34(3):1–5. doi: 10.1109/tasc.2023.3345290
[45] Yu L, Zhao H, Xu JY, et al. Influence of pre-overpressure heat treatment on micro-structure and related properties of Bi-2212 round wire. Physica C: Supercond Appl. 2024;622:1354521. doi: 10.1016/j.physc.2024.1354521
[46] Zhang ZC, Yu M, Yang DS, et al. Revealing the effect of bridges in the multi-filamentary Bi-2212 wires. Supercond Sci Technol. 2024;37(4):045010. doi: 10.1088/1361-6668/ad2b7a
[47] Takeda Y, Nishijima G, Nakai U, et al. Angular dependence of resistance and critical current of a Bi-2223 superconducting joint. Supercond Sci Technol. 2023;36(12):125010. doi: 10.1088/1361-6668/ad0565
[48] Takeda Y, Nishijima G, Inoue K, et al. The effect of intermediate layer densification on the critical current of a Bi-2223 superconducting joint. Supercond Sci Technol. 2023;36(3):035004. doi: 10.1088/1361-6668/acaccd
[49] Jin S, Tiefel TH, Sherwood RC, et al. Melt-textured growth of polycrystalline YBa2Cu3O7-d with high transport Jc at 77 K. Phys Rev B. 1988;37(13):7850–7853. doi: 10.1103/PhysRevB.37.7850
[50] Sawano K, Morita M, Tanaka M, et al. High magnetic flux trapping by melt-grown YBaCuO superconductors. Jpn J Appl Phys. 1991;30(7A):L1157. doi: 10.1143/JJAP.30.L1157
[51] Cardwell DA. Processing and properties of large grain (RE)BCO. Mater Sci Eng: B. 1998;53(1–2):1–10. doi: 10.1016/s0921-5107(97)00293-6
[52] Vanderbemden P, Bradley AD, Doyle RA, et al. Superconducting properties of natural and artificial grain boundaries in bulk melt-textured YBCO. Physica C: Supercond. 1998;302(4):257–270. doi: 10.1016/s0921-4534(98)00238-x
[53] Shi Y, Babu NH, Cardwell DA. Development of a generic seed crystal for the fabrication of large grain (re)–ba–cu–O bulk superconductors. Supercond Sci Technol. 2005;18(4):L13–L16. doi: 10.1088/0953-2048/18/4/l01
[54] Lee PJ, Larbalestier DC. Development of nanometer scale structures in composites of Nb-Ti and their effect on the superconducting critical current density. Acta Metallurgica. 1987;35(10):2523–2536. doi: 10.1016/0001-6160(87)90149-0
[55] Yamafuji K, Harada N, Mawatari Y, et al. Achievement of high current density in Nb-Ti superconducting multifilamentary wires by introducing designed artificial pins. Cryogenics. 1991;31(6):431–438. doi: 10.1016/0011-2275(91)90203-9
[56] Kamihara Y, Watanabe T, Hirano M, et al. Iron-based layered superconductor LaO1-xFxFeAs (x=0.05-0.12) with Tc = 26 K. J Am Chem Soc. 2008;130(11):3296. doi: 10.1021/ja800073m
[57] Rotter M, Tegel M, Johrendt D. Superconductivity at 38 K in the iron arsenide (Ba 1 − x K x) Fe 2 as 2. Phys Rev Lett. 2008;101(10):107006. doi: 10.1103/PhysRevLett.101.107006
[58] Hsu F-C, Luo J-Y, Yeh K-W, et al. Superconductivity in the PbO-type structure α-FeSe. Proc Natl Acad Sci USA. 2008;105(38):14262–14264. doi: 10.1073/pnas.0807325105
[59] Iyo A, Kawashima K, Kinjo T, et al. New-structure-type Fe-based superconductors: CaAFe4As4 (A = K, Rb, Cs) and SrAFe4As4 (A = Rb, Cs). J Am Chem Soc. 2016;138(10):3410–3415. doi: 10.1021/jacs.5b12571
[60] Fernandes RM, Coldea AI, Ding H, et al. Iron pnictides and chalcogenides: a new paradigm for superconductivity. Nature. 2022;601(7891):35–44. doi: 10.1038/s41586-021-04073-2
[61] Hanzawa K, Matsumoto J, Iimura S, et al. High upper critical field (120 T) with small anisotropy of highly hydrogen-substituted SmFeAsO epitaxial film. Phys Rev Mater. 2022;6(11):L111801. doi: 10.1103/PhysRevMaterials.6.L111801

[62] Baily SA, Kohama Y, Hiramatsu H, et al. Pseudoisotropic upper critical field in cobalt-doped SrFe2As2 epitaxial films. Phys Rev Lett. 2009;102 (11):117004. doi: 10.1103/PhysRevLett.102.117004
[63] Jo YJ, Jaroszynski J, Yamamoto A, et al. High-field phase-diagram of Fe arsenide superconductors. Physica C: Supercond. 2009;469(9–12):566–574. doi: 10.1016/j.physc.2009.03.010
[64] Yamamoto A, Jaroszynski J, Tarantini C, et al. Small anisotropy, weak thermal fluctuations, and high field superconductivity in Co-doped iron pnictide Ba(Fe1 −xCox)2As2. Appl Phys Lett. 2009;94(6):062511. doi: 10.1063/1.3081455
[65] Tarantini C, Gurevich A, Jaroszynski J, et al. Significant enhancement of upper critical fields by doping and strain in iron-based superconductors. Phys Rev B. 2011;84(18):184522. doi: 10.1103/PhysRevB.84.184522
[66] Dong CH, Xu QJ, Ma YW. Towards high-field applications: high-performance, low-cost iron-based superconductors. Natl Sci Rev. 2024;11(11):nwae122. doi: 10.1093/nsr/nwae122
[67] Putti M, Pallecchi I, Bellingeri E, et al. New Fe-based superconductors: properties relevant for applications. Supercond Sci Technol. 2010;23(3):034003. doi: 10.1088/0953-2048/23/3/034003
[68] Lee S, Jiang J, Weiss JD, et al. Weak-link behavior of grain boundaries in superconducting Ba(Fe1−xCox) 2As2 bicrystals. Appl Phys Lett. 2009;95(21):212505. doi: 10.1063/1.3262953
[69] Katase T, Ishimaru Y, Tsukamoto A, et al. Advantageous grain boundaries in iron pnictide superconductors. Nat Commun. 2011;2(1):409. doi: 10.1038/ncomms1419
[70] Xu ZT, Dong CH, Cai CAB, et al. Thickness dependence of structural and superconducting properties of Co-doped BaFe2As2 coated conductors. iScience. 2021;24(8):102922. doi: 10.1016/j.isci.2021.102922
[71] Thomas AA, Shipulin IA, Holleis S, et al. Comparative study of Fe(Se,Te) thin films on flexible coated conductor templates and single-crystal substrates. Supercond Sci Technol. 2021;34 (11):115013. doi: 10.1088/1361-6668/ac2557
[72] Piperno L, Vannozzi A, Augieri A, et al. High-performance Fe(Se,Te) films on chemical CeO2-based buffer layers. Sci Rep. 2023;13(1):569. doi: 10.1038/s41598-022-24044-5
[73] Kametani F, Su Y, Tarantini C, et al. On the mechanisms of Jc increment and degradation in high-Jc Ba122 tapes made by different processing methods. Appl Phys Express. 2024;17(1):013004. doi: 10.35848/1882-0786/ad1891
[74] Gao ZS, Togano K, Matsumoto A, et al. Achievement of practical level critical current densities in Ba1 −xKxFe2As2/Ag tapes by conventional cold mechanical deformation. Sci Rep. 2014;4(1):4065. doi: 10.1038/srep04065
[75] Gao ZS, Togano K, Matsumoto A, et al. High transport jc in magnetic fields up to 28T of stainless steel/Ag double sheathed Ba122 tapes fabricated by scalable rolling process. Supercond Sci Technol. 2015;28 (1):012001. doi: 10.1088/0953-2048/28/1/012001
[76] Dong Q, Tian B, Hong W, et al. Critical currents of 100-m class Ag-sheathed Sr0.6K0.4Fe2As2 tape under various temperatures, magnetic fields, and angles. IEEE Trans Appl Supercond. 2019;29(5):1–5. doi: 10.1109/tasc.2019.2907263
[77] Dong CH, Yao C, Zhang XP, et al. Transport critical current density in single-core composite Ba122 superconducting tapes. IEEE Trans Appl Supercond. 2019;29(5):1–4. doi: 10.1109/tasc.2019.2901378
[78] Liu C, Zhang XP, Dong CH, et al. High transport jc in 7-filament Cu/Ag sheathed Ba0.6K0.4Fe2As2 tapes manufactured by ambient pressure sintering. J Alloys And Compd. 2023;966:171592. doi: 10.1016/j.jallcom.2023.171592
[79] Tokuta S, Hasegawa Y, Shimada Y, et al. Enhanced critical current density in K-doped Ba122 polycrystalline bulk superconductors via fast densification. iScience. 2022;25(4):103992. doi: 10.1016/j.isci.2022.103992
[80] Tamegai T, Wu WX, Yu C, et al. Bulk 122-type iron-based superconductors sintered under high pressure. IEEE Trans Appl Supercond. 2024;34 (3):1–5. doi: 10.1109/tasc.2023.3347683
[81] Weiss JD, Tarantini C, Jiang J, et al. High intergrain critical current density in fine-grain (Ba0.6K0.4) Fe2As2 wires and bulks. Nat Mater. 2012;11 (8):682–685. doi: 10.1038/nmat3333
[82] Pyon S, Ito T, Sasaki T, et al. Record-high critical current density in (Ba,Na)Fe2As2 round wire suitable for high-field applications. Physica C: Supercond Appl. 2023;615:1354354. doi: 10.1016/j.physc.2023.1354354
[83] Fu CD, Dong CH, Tu C, et al. High critical current density in low-cost iron-based superconducting round wires annealed at ambient pressure. Supercond Sci Technol. 2024;37(3):035015. doi: 10.1088/1361-6668/ad20ff
[84] Masi A, Armenio AA, Augieri A, et al. Development of Ca/K-1144 IBS wires with composite Cu/Ta sheaths. IEEE Trans Appl Supercond. 2024;34 (3):1–5. doi: 10.1109/tasc.2024.3371402
[85] Nagamatsu J, Nakagawa N, Muranaka T, et al. Superconductivity at 39 K in magnesium diboride. Nature. 2001;410(6824):63–64. doi: 10.1038/35065039
[86] Larbalestier DC, Cooley LD, Rikel MO, et al. Strongly linked current flow in polycrystalline forms of the superconductor MgB2. Nature. 2001;410 (6825):186–189. doi: 10.1038/35065559
[87] Kawaguchi T, Uemura H, Ohno T, et al. Epitaxial growth of NdFeAsO thin films by molecular beam epitaxy. Appl Phys Express. 2009;2(9):093002. doi: 10.1143/APEX.2.093002
[88] Kawaguchi T, Uemura H, Ohno T, et al. In situ growth of superconducting NdFeAs(O,F) thin films by molecular beam epitaxy. Appl Phys Lett. 2010;97 (4):042509. doi: 10.1063/1.3464171
[89] Matsumoto J, Hanzawa K, Sasase M, et al. Superconductivity at 48 K of heavily hydrogen-doped SmFeAsO epitaxial films grown by topotactic chemical reaction using CaH2. Phys Rev Mater. 2019;3(10):103401. doi: 10.1103/PhysRevMaterials.3.103401
[90] Kondo K, Motoki S, Hatano T, et al. NdFeAs(O,H) epitaxial thin films with high critical current density. Supercond Sci Technol. 2020;33(9):09LT01. doi: 10.1088/1361-6668/aba353
[91] Iida K, Hänisch J, Kondo K, et al. High jc and low anisotropy of hydrogen doped NdFeAsO superconducting thin film. Sci Rep. 2021;11(1):5636. doi: 10.1038/s41598-021-85216-3

[92] Kauffmann-Weiss S, Iida K, Tarantini C, et al. Microscopic origin of highly enhanced current carrying capabilities of thin NdFeAs(O,F) films. Nanoscale Adv. 2019;1(8):3036–3048. doi: 10.1039/c9na00147f
[93] Iimura S, Okanishi H, Matsuishi S, et al. Large-moment antiferromagnetic order in overdoped high- T c superconductor 154SmFeAsO1-xDx. Proc Natl Acad Sci USA. 2017;114(22):E4354–E4359. doi: 10.1073/pnas.1703295114
[94] Iida K, Hänisch J, Hata S, et al. Recent progress on epitaxial growth of Fe-based superconducting thin films. Supercond Sci Technol. 2023;36(6):063001. doi: 10.1088/1361-6668/acccb2
[95] Hatano T, Kawaguchi T, Fujimoto R, et al. Thin film growth of CaFe2As2 by molecular beam epitaxy. Supercond Sci Technol. 2016;29(1):015013. doi: 10.1088/0953-2048/29/1/015013
[96] Qin D, Iida K, Hatano T, et al. Realization of epitaxial thin films of the superconductor K-doped BaFe2As2. Phys Rev Mater. 2021;5(1):014801. doi: 10.1103/PhysRevMaterials.5.014801
[97] Iida K, Qin D, Tarantini C, et al. Approaching the ultimate superconducting properties of (Ba,K)Fe2As2 by naturally formed low-angle grain boundary networks. NPG Asia Mater. 2021;13(1):68. doi: 10.1038/s41427-021-00337-5
[98] Fang L, Jia Y, Chaparro C, et al. High, magnetic field independent critical currents in (Ba,K)Fe2As2 crystals. Appl Phys Lett. 2012;101(1):012601. doi: 10.1063/1.4731204
[99] Qin D, Iida K, Guo Z, et al. K-doped Ba122 epitaxial thin film on MgO substrate by buffer engineering. Supercond Sci Technol. 2022;35(9):09LT01. doi: 10.1088/1361-6668/ac8025
[100] Tsukada I, Hanawa M, Akiike T, et al. Epitaxial growth of FeSe0.5Te0.5 thin films on CaF2 substrates with high critical current density. Appl Phys Express. 2011;4(5):053101. doi: 10.1143/APEX.4.053101
[101] Kurth F, Reich E, Hänisch J, et al. Versatile fluoride substrates for Fe-based superconducting thin films. Appl Phys Lett. 2013;102(14):142601. doi: 10.1063/1.4801312
[102] Uemura H, Kawaguchi T, Ohno T, et al. Substrate dependence of the superconducting properties of NdFeAs(O,F) thin films. Solid State Commun. 2012;152(8):735–739. doi: 10.1016/j.ssc.2012.01.037
[103] Ueda S, Takeda S, Takano S, et al. High-Tc and high-Jc SmFeAs(O,F) films on fluoride substrates grown by molecular beam epitaxy. Appl Phys Lett. 2011;99(23):232505. doi: 10.1063/1.3664632
[104] Si W, Han SJ, Shi X, et al. High current superconductivity in FeSe0.5Te0.5-coated conductors at 30 tesla. Nat Commun. 2013;4(1):1347. doi: 10.1038/ncomms2337
[105] Ozaki T, Wu L, Zhang C, et al. A route for a strong increase of critical current in nanostrained iron-based superconductors. Nat Commun. 2016;7(1):13036. doi: 10.1038/ncomms13036
[106] Tokuta S, Shimada Y, Yamamoto A. Evolution of intergranular microstructure and critical current properties of polycrystalline Co-doped BaFe 2 as 2 through high-energy milling. Supercond Sci Technol. 2020;33(9):094010. doi: 10.1088/1361-6668/aba545
[107] Iida K, Yamauchi Y, Hatano T, et al. Structural analysis and transport properties of [010]-tilt grain boundaries in Fe(Se,Te). Sci Technol Adv Mater. 2024;25:2384829. doi: 10.1080/14686996.2024.2384829
[108] Iida K, Omura T, Matsumoto T, et al. Grain boundary characteristics of oxypnictide NdFeAs(O,F) superconductors. Supercond Sci Technol. 2019;32(7):074003. doi: 10.1088/1361-6668/ab1660
[109] Durrell JH, Eom CB, Gurevich A, et al. The behavior of grain boundaries in the Fe-based superconductors. Rep Prog Phys. 2011;74(12):124511. doi: 10.1088/0034-4885/74/12/124511
[110] Hänisch J, Iida K. Grain boundaries in Fe-based superconductors. In: Mele P, Prassides K Tarantini C, eds. Superconductivity: from materials science to practical applications. Cham: Springer International Publishing; 2020. p. 269–302.
[111] Iida K, Hänisch J, Yamamoto A. Grain boundary characteristics of Fe-based superconductors. Supercond Sci Technol. 2020;33(4):043001. doi: 10.1088/1361-6668/ab73ef
[112] Si W, Zhang C, Shi X, et al. Grain boundary junctions of FeSe0.5Te0.5 thin films on SrTiO3 bi-crystal substrates. Appl Phys Lett. 2015;106(3):032602. doi: 10.1063/1.4906429
[113] Sarnelli E, Nappi C, Camerlingo C, et al. Properties of Fe(Se, Te) bicrystal grain boundary junctions, SQUIDs, and Nanostrips. IEEE Trans Appl Supercond. 2017;27(4):1–4. doi: 10.1109/TASC.2016.2636248
[114] Budai JD, Yang W, Tamura N, et al. X-ray microdiffraction study of growth modes and crystallographic tilts in oxide films on metal substrates. Nat Mater. 2003;2(7):487–492. doi: 10.1038/nmat916
[115] Katase T, Ishimaru Y, Tsukamoto A, et al. DC superconducting quantum interference devices fabricated using bicrystal grain boundary junctions in Co-doped BaFe2As2 epitaxial films. Supercond Sci Technol. 2010;23(8):082001. doi: 10.1088/0953-2048/23/8/082001
[116] Sarnelli E, Nappi C, Leveratto A, et al. Fe(Se,Te) superconducting quantum interference devices. Supercond Sci Technol. 2017;30(6):065003. doi: 10.1088/1361-6668/aa6a84
[117] Pagano S, Martucciello N, Enrico E, et al. Iron-based superconducting nanowires: electric transport and voltage-noise properties. Nanomater. 2020 [cited 862 p.];10(5):862. doi: 10.3390/nano10050862
[118] Tsuji Y, Hatano T, Kondo K, et al. Microfabrication of NdFeAs(O,F) thin films and evaluation of the transport properties. Supercond Sci Technol. 2020;33(7):074001. doi: 10.1088/1361-6668/ab8619
[119] Yoshikawa A, Hatano T, Hibino H, et al. Fabrication of microstrips of iron-based superconductor NdFeAs(O,H). Supercond Sci Technol. 2024;37(8):085008. doi: 10.1088/1361-6668/ad5b24
[120] Singh SJ, Bristow M, Meier WR, et al. Ultrahigh critical current densities, the vortex phase diagram, and the effect of granularity of the stoichiometric high-tc superconductor CaKFe4As4. Phys Rev Mater. 2018;2(7):074802. doi: 10.1103/PhysRevMaterials.2.074802
[121] Tokuta S, Yamamoto A. Enhanced upper critical field in Co-doped Ba122 superconductors by lattice defect tuning. APL Mater. 2019;7(11):111107. doi: 10.1063/1.5098057
[122] Pak C, Su YF, Collantes Y, et al. Synthesis routes to eliminate oxide impurity segregation and their influence on intergrain connectivity in K-doped BaFe2As2

polycrystalline bulks. Supercond Sci Technol. 2020;33 (8):084010. doi: 10.1088/1361-6668/aba01a
[123] Masi A, Armenio AA, Celentano G, et al. The role of chemical composition in the synthesis of Ca/K-1144 iron based superconductors. J Alloys And Compd. 2021;869:159202. doi: 10.1016/j.jallcom.2021.159202
[124] Ishida S, Naik SPK, Tsuchiya Y, et al. Synthesis of CaKFe4As4 bulk samples with high critical current density using a spark plasma sintering technique. Supercond Sci Technol. 2020;33(9):094005. doi: 10.1088/1361-6668/aba019
[125] Pervakov KS, Vlasenko VA. Synthesis of electron- and hole-doped bulk BaFe2As2 superconductors by mechanical alloying. Ceram Int. 2020;46 (7):8625–8630. doi: 10.1016/j.ceramint.2019.12.095
[126] Masi A, Armenio AA, Augieri A, et al. Mechanochemically assisted synthesis of Ca/K 1144-type iron pnictides. IEEE Trans Appl Supercond. 2021;31(5):1–5. doi: 10.1109/tasc.2021.3059220
[127] Tarantini C, Pak C, Su YF, et al. Effect of heat treatments on superconducting properties and connectivity in K-doped BaFe2As2. Sci Rep. 2021;11(1):3143. doi: 10.1038/s41598-021-82325-x
[128] Weiss JD, Yamamoto A, Polyanskii AA, et al. Demonstration of an iron-pnictide bulk superconducting magnet capable of trapping over 1T. Supercond Sci Technol. 2015;28(11):112001. doi: 10.1088/0953-2048/28/11/112001
[129] Guo WW, Yao C, Huang H, et al. Enhancement of transport Jc in (Ba, K)Fe2As2 HIP processed round wires. Supercond Sci Technol. 2021;34(9):094001. doi: 10.1088/1361-6668/ac1952
[130] Pyon S, Ito T, Sakagami R, et al. Fabrication of multi-filament(Ba,A)Fe2As2 (A: Na, K) HIP round wires and a small superconducting coil. Supercond Sci Technol. 2023;36(1):015009. doi: 10.1088/1361-6668/aca726
[131] Manasa M, Azam M, Zajarniuk T, et al. Enhancement of superconducting properties of polycrystalline CaKFe4As4 by high-pressure growth. IEEE Trans Appl Supercond. 2024;34(3):1–5. doi: 10.1109/tasc.2023.3345821
[132] Ishida S, Song D, Ogino H, et al. Doping-dependent critical current properties in K, Co, and P-doped BaFe2As2 single crystals. Phys Rev B. 2017;95 (1):014517. doi: 10.1103/PhysRevB.95.014517
[133] Sundar S, Salem-Sugui S, Lovell E, et al. Doping dependence of the second magnetization peak, critical current density, and pinning mechanism in BaFe2-xNixAs2 pnictide superconductors. ACS Appl Electron Mater. 2019;1(2):179–188. doi: 10.1021/acsaelm.8b00014
[134] Sundar S, Salem-Sugui S, Alvarenga AD, et al. Strong pinning in the hole-doped pnictide superconductor La0.34Na0.66Fe2As2. J Appl Phys. 2019;125 (12):123902. doi: 10.1063/1.5088823
[135] Van Gennep D, Hassan A, Luo HQ, et al. Sharp peak of the critical current density in BaFe 2 − x Ni x as 2 at optimal composition. Phys Rev B. 2020;101 (23):235163. doi: 10.1103/PhysRevB.101.235163
[136] Kawachi S, Yamaura J, Kuramoto Y, et al. Distinctive doping dependence of upper critical field in iron-based superconductor LaFeAsO 1 − x H x. Phys Rev B. 2023;108(10):L100503. doi: 10.1103/PhysRevB.108.L100503
[137] Ma QS, Lan F, Qiu WB, et al. Enhancement of superconductivity in FeNbxSe0.95 by hole carrier doping. J Mater Chem C. 2019;7(32):10019–10027. doi: 10.1039/c9tc02664a
[138] Liu JX, Zhang SN, Li M, et al. Boosting superconducting properties of Fe(Se, Te) via dual-oscillation phenomena induced by fluorine doping. ACS Appl Mater Interfaces. 2019;11(20):18825–18832. doi: 10.1021/acsami.9b02469
[139] Li D, Yuan J, Shen PP, et al. Giant enhancement of critical current density at high field in superconducting (Li,fe)ohfese films by Mn doping. Supercond Sci Technol. 2019;32(12):12lt01. doi: 10.1088/1361-6668/ab4e7c
[140] Haberkorn N, Xu M, Meier WR, et al. Effect of Ni doping on vortex pinning in CaK (F e 1 − x N i x) 4 a s 4 single crystals. Phys Rev B. 2019;100(6):064524. doi: 10.1103/PhysRevB.100.064524
[141] Singh SJ, Diduszko R, Iwanowski P, et al. Effect of Pb addition on microstructure, transport properties, and the critical current density in a polycrystalline FeSe0.5Te0.5. Appl Phys A. 2022;128(6):476. doi: 10.1007/s00339-022-05588-9
[142] Masi A, Duchenko A, Celentano G, et al. Tailoring the critical temperature of Ca/K-1144 superconductors: the effect of aliovalent substitution on tetragonality. Supercond Sci Technol. 2022;35 (6):065015. doi: 10.1088/1361-6668/ac6630
[143] Masi A, Duchenko A, Armenio AA, et al. Aliovalent substitution in 1144 iron based superconductors: effect on structure and superconducting properties. IEEE Trans Appl Supercond. 2022;32(4):1–5. doi: 10.1109/tasc.2021.3138955
[144] Zhang J, Hänisch J, Yang XS, et al. Effect of carbon doping on magnetic flux pinning and superconducting performance in FeSe0.5Te0.5 single crystals. Supercond Sci Technol. 2023;36(2):025008. doi: 10.1088/1361-6668/acadb5
[145] Zou Q, Oli BD, Zhang H, et al. Deciphering alloy composition in superconducting single-layer FeSe1–xSx on SrTiO3(001) substrates by machine learning of STM/S data. ACS Appl Mater Interfaces. 2023;15 (18):22644–22650. doi: 10.1021/acsami.2c23324
[146] Aouelela MHA, Taha M, El-Dek SI, et al. Synthesis and characterization of molybdenum- and sulfur-doped FeSe. ACS Omega. 2023;8 (39):36553–36561. doi: 10.1021/acsomega.3c05684
[147] Rusakov VA, Volkov MP. Effect of partial substitution of iron for group IV elements on the structure and superconducting properties of the Fe(Se0.2Te0.8) 0.82Compound. Tech Phys. 2023;68(12):758–765. doi: 10.1134/s1063784223080315
[148] Bud'ko SL, Xu MY, Canfield PC. Trapped flux in pure and Mn-substituted CaKFe4As4 and MgB2 superconducting single crystals. Supercond Sci Technol. 2023;36(11):115001. doi: 10.1088/1361-6668/acf413
[149] Augieri A, Duchenko A, De Marzi G, et al. Pinning properties of 1144 polycrystalline samples with aliovalent doping. IEEE Trans Appl Supercond. 2024;34 (3):1–5. doi: 10.1109/tasc.2023.3348433
[150] Manasa M, Azam M, Zajarniuk T, et al. Comparison of Gd addition effect on the superconducting properties of FeSe0.5Te0.5 bulks under ambient and high-pressure conditions. Ceram Int. 2024;50 (1):714–725. doi: 10.1016/j.ceramint.2023.10.150
[151] Cheng Z, Dong CH, Huang H, et al. Chemical stability and superconductivity in Ag-sheathed

CaKFe4As4 superconducting tapes. Supercond Sci Technol. 2019;32(1):015008. doi: 10.1088/1361-6668/aaedff
[152] Wang CL, He T, Han QQ, et al. Flux pinning and the vortex phase diagram in optimized CaKFe4As4 single crystals fabricated by a one-step method. Supercond Sci Technol. 2020;33(4):045011. doi: 10.1088/1361-6668/ab75aa
[153] Singh SJ, Cassidy SJ, Bristow M, et al. Optimization of superconducting properties of the stoichiometric CaKFe4As4. Supercond Sci Technol. 2020;33(2):025003. doi: 10.1088/1361-6668/ab58be
[154] Liu JX, Zhang SN, Sang LN, et al. Enhancement of superconducting properties in polycrystalline Fe(Se, Te) via a dual coordination effect. Scr Materialia. 2019;169:19–22. doi: 10.1016/j.scriptamat.2019.04.029
[155] Cheng Z, Liu SF, Dong CH, et al. Effects of core density and impurities on the critical current density of CaKFe4As4 superconducting tapes. Supercond Sci Technol. 2019;32(10):105014. doi: 10.1088/1361-6668/ab3a87
[156] Rendenbach B, Hohl T, Harm S, et al. Electrochemical synthesis and crystal structure of the organic ion intercalated superconductor (TMA)0.5Fe2Se2 with Tc=43 K. J Am Chem Soc. 2021;143(8):3043–3048. doi: 10.1021/jacs.0c13396
[157] Xiao Y, Jin H, Pan XF, et al. Fabrication and superconducting properties of 19-filamentary Sr0.6K0.4Fe2As2/Ag/monel composite wires and tapes. J Supercond Nov Magn. 2022;35(3):697–703. doi: 10.1007/s10948-021-06137-w
[158] Sánchez-Zacate FE, Conde-Gallardo A. The particle size effect on the irreversible magnetization and critical current density in low fields for polycrystalline SmFeAsO0.91F0.09 superconductors. J Supercond Nov Magn. 2021;34(12):3141–3149. doi: 10.1007/s10948-021-06048-w
[159] Liu SF, Yao C, Huang H, et al. High-performance Ba1-xKxfe2as2 superconducting tapes with grain texture engineered via a scalable fabrication. Sci China-Mater. 2021;64(10):2530–2540. doi: 10.1007/s40843-020-1643-1
[160] Yao C, Guo WW, Zhu YC, et al. Interface effects on the current transport properties of multi-layered (Ba, K)Fe2As2 superconducting wires. J Mater Chem C. 2023;11(4):1470–1482. doi: 10.1039/d2tc04111a
[161] Xu XC, Wan F, Sung ZH. A bi-layer barrier design for 122-type iron-based superconducting wires and tapes. Cryogen. 2022;128:103598. doi: 10.1016/j.cryogenics.2022.103598
[162] Xia X, Zhu YC, Zhu CD, et al. Constitutive behaviour study of Ba1-xKxFe2As2 iron-based superconducting powder. Supercond Sci Technol. 2023;36(4):045016. doi: 10.1088/1361-6668/acbe73
[163] Vlasenko VA, Degtyarenko AY, Shilov AI, et al. Phase formation of iron-based superconductors during mechanical alloying. Mater. 2022;15(23):8438. doi: 10.3390/ma15238438
[164] Jin H, Xiao Y, Nong XY, et al. Superconducting properties and intergranular coupling of high-strength Sr1-xKxfe2as2/ag/nb/cu composite conductors. Ceram Int. 2023;49(7):11680–11688. doi: 10.1016/j.ceramint.2022.12.018
[165] Han M, Yao C, Zhang XP, et al. Mechanical properties and densification mechanism of powder-in-tube Ba x K 1–x Fe 2 as 2 superconductors. Supercond Sci Technol. 2022;35(5):055006. doi: 10.1088/1361-6668/ac4ba0
[166] Azam M, Manasa M, Zajarniuk T, et al. Optimization of synthesis parameters and superconducting properties of GdFeAsOF. IEEE Trans Appl Supercond. 2024;34(3):1–5. doi: 10.1109/tasc.2023.3341858
[167] Tu C, Dong CH, Huang H, et al. Chemical durability of BaK122 superconducting cores under different environmental conditions. IEEE Trans Appl Supercond. 2024;34(3):1–5. doi: 10.1109/tasc.2023.3341892
[168] Yao C, Ma YW. Recent breakthrough development in iron-based superconducting wires for practical applications. Supercond Sci Technol. 2019;32(2):023002. doi: 10.1088/1361-6668/aaf351
[169] Pyon S, Suwa T, Tamegai T, et al. Improvements of fabrication processes and enhancement of critical current densities in (Ba,K)Fe2As2 hIP wires and tapes. Supercond Sci Technol. 2018;31(5):055016. doi: 10.1088/1361-6668/aab8c3
[170] Liu SF, Cheng Z, Yao C, et al. High critical current density in Cu/Ag composited sheathed Ba0.6K0.4Fe2As2 tapes prepared via hot isostatic pressing. Supercond Sci Technol. 2019;32(4):044007. doi: 10.1088/1361-6668/aaff27
[171] Imai S, Itou S, Ishida S, et al. Highly c-axis orientated superconducting core and large critical current density in Ba0.6Na0.4Fe2As2 powder-in-tube tape. Sci Rep. 2019;9(1):13064. doi: 10.1038/s41598-019-49363-y
[172] Koblischka MR, Koblischka-Veneva A, Schmauch J, et al. Microstructure and flux pinning of reacted-and-pressed, polycrystalline Ba0.6K0.4Fe2As2 powders. Mater. 2019;12(13):2173. doi: 10.3390/ma12132173
[173] Liu X, Shi Y, Liu F, et al. Critical current degradation behavior of 7-filamentary Ba 1−x K x Fe 2 as 2 tapes under uniaxial strain. Supercond Sci Technol. 2023;36(1):015004. doi: 10.1088/1361-6668/aca4a7
[174] Huang H, Yao C, Li L, et al. Effects of heat treatment temperature on the superconducting properties of Ba1−xKxFe2As2 tapes. Supercond Sci Technol. 2019;32(2):025007. doi: 10.1088/1361-6668/aaf486
[175] Masi A, Alvani C, Armenio AA, et al. Fe(Se,Te) system crystallized in molten chlorides flux: the obtained materials and their characterization. J Cryst Growth. 2019;528:125268. doi: 10.1016/j.jcrysgro.2019.125268
[176] Fan LL, Cheng PY, Han J, et al. Annealing effects on the structural, surface, and superconducting properties of FeTe0.55Se0.45 single crystals. J Supercond Nov Magn. 2021;34(7):1739–1744. doi: 10.1007/s10948-020-05727-4
[177] Tokuta S, Yamamoto A. Thermal response of the iron-based Ba122 superconductor to in situ and ex situ processes. Supercond Sci Technol. 2021;34(3):034004. doi: 10.1088/1361-6668/abda5e
[178] Pyon S, Miyawaki D, Veshchunov I, et al. Fabrication and characterization of CaKFe4As4 round wires sintered at high pressure. Appl Phys Express. 2018;11(12):123101. doi: 10.7567/apex.11.123101
[179] Pyon S, Miyawaki D, Tamegai T, et al. Enhancement of critical current density in (Ba,Na)Fe2As2 round wires using high-pressure sintering. Supercond Sci Technol. 2020;33(6):065001. doi: 10.1088/1361-6668/ab804c
[180] Singh SJ, Sturza MI. Bulk and single crystal growth progress of iron-based superconductors (FBS): 1111

and 1144. Cryst. 2022;12(1):20. doi: 10.3390/cryst12010020
[181] Sang LN, Li Z, Yang GS, et al. Pressure effects on iron-based superconductor families: superconductivity, flux pinning and vortex dynamics. Mater Today Phys. 2021;19:100414. doi: 10.1016/j.mtphys.2021.100414
[182] Ishida S, Kamiya Y, Tsuchiya Y, et al. Synthesis of c-axis textured CaKFe4As4 superconducting bulk via spark plasma texturing technique. J Alloys And Compd. 2023;961:171093. doi: 10.1016/j.jallcom.2023.171093
[183] Lin H, Yao C, Zhang XP, et al. Hot pressing to enhance the transport jc of Sr0.6K0.4Fe2As2 superconducting tapes. Sci Rep. 2014;4(1):6944. doi: 10.1038/srep06944
[184] Hecher J, Baumgartner T, Weiss JD, et al. Small grains: a key to high-field applications of granular Ba-122 superconductors? Supercond Sci Technol. 2016;29(2):025004. doi: 10.1088/0953-2048/29/2/025004
[185] Kim YJ, Weiss JD, Hellstrom EE, et al. Evidence for composition variations and impurity segregation at grain boundaries in high current-density polycrystalline K- and Co-doped BaFe2As2 superconductors. Appl Phys Lett. 2014;105(16):162604. doi: 10.1063/1.4898191
[186] Kametani F, Su YF, Collantes Y, et al. Chemically degraded grain boundaries in fine-grain Ba0.6K0.4Fe2As2 polycrystalline bulks. Appl Phys Express. 2020;13(11):113002. doi: 10.35848/1882-0786/abbfdf
[187] Dong CH, Huang H, Ma YW. Slow vortex creep induced by strong grain boundary pinning in advanced Ba122 superconducting tapes. Chin Phys Lett. 2019;36(6):067401. doi: 10.1088/0256-307x/36/6/067401
[188] Huang H, Yao C, Dong CH, et al. Visualization of the grain structure in high-performance Ba 1−x K x Fe 2 as 2 superconducting tapes. Supercond Sci Technol. 2021;34(4):045017. doi: 10.1088/1361-6668/abe7ad
[189] Liu JX, Shao BT, Liu XQ, et al. Improving superconducting performance of Fe(Se, Te) with in situ formed grain-boundary strengthening and flux pinning centers. ACS Appl Mater Interfaces. 2022;14(1):2246–2254. doi: 10.1021/acsami.1c18906
[190] Llovo IF, Mosqueira J, Hu D, et al. Enhancement of the critical current by surface irregularities in Fe-based superconductors. Supercond Sci Technol. 2024;37(7):075018. doi: 10.1088/1361-6668/ad5114
[191] Xu ZT, Zhang QH, Fan F, et al. C-axis superconducting performance enhancement in Co-doped Ba122 thin films by an artificial pinning center design. Supercond Sci Technol. 2019;32(12):125014. doi: 10.1088/1361-6668/ab4f44
[192] Wang CL, He T, Han QQ, et al. Vortex pinning and the mechanism in CaKFe4As4 revealed by dynamical magnetization relaxation. J Supercond Nov Magn. 2020;33(7):1979–1986. doi: 10.1007/s10948-020-05482-6
[193] Galluzzi A, Buchkov K, Nazarova E, et al. Pinning energy and anisotropy properties of a Fe(Se,Te) iron based superconductor. Nanotechnology. 2019;30(25):254001. doi: 10.1088/1361-6528/ab0c23
[194] Nakamura R, Tokuda M, Watanabe M, et al. Thickness-induced crossover from strong to weak collective pinning in exfoliated FeTe0.6Se0.4 thin films at 1 T. Phys Rev B. 2021;104(16):165412. doi: 10.1103/PhysRevB.104.165412
[195] Llovo IF, Sóñora D, Mosqueira J, et al. Vortex dynamics and second magnetization peak in the iron-pnictide superconductor Ca0.82La0.18Fe0.96Ni0.04As2. Supercond Sci Technol. 2021;34(11):115010. doi: 10.1088/1361-6668/ac2556
[196] Galluzzi A, Leo A, Masi A, et al. Critical current and pinning features of a CaKFe4As4 polycrystalline sample. Mater. 2021;14(21):6611. doi: 10.3390/ma14216611
[197] Tang MH, Dong CH, Xu ZT, et al. Transition of vortex pinning behaviour induced by an artificial microstructure design in Ba(Fe0.94Co0.06)2As2 pnictide superconductor. Mater Today Phys. 2022;27:100783. doi: 10.1016/j.mtphys.2022.100783
[198] Degtyarenko AY, Vlasenko VA, Kuzmicheva TE, et al. Anisotropy of the critical current and abrikosov vortex pinning in magnetic superconductor EuCsFe4As4. Jetp Lett. 2023;118(11):855–860. doi: 10.1134/s002136402360338x
[199] Lopes PV, Sundar S, Salem-Sugui S, et al. Second magnetization peak, anomalous field penetration, and Josephson vortices in KCa$_2$Fe$_4$As$_4$F$_2$ bilayer pnictide superconductor. Sci Rep. 2022;12(1):20359. doi: 10.1038/s41598-022-24012-z
[200] Bud'ko SL, Huyan SY, Xu MY, et al. Trapped flux in a small crystal of CaKFe4As4 at ambient pressure and in a diamond anvil pressure cell. Supercond Sci Technol. 2024;37(6):065010. doi: 10.1088/1361-6668/ad45c7
[201] Strickland NM, Chong S, Dong CH, et al. Low field anomaly in the critical current of Ba 1− x K x Fe 2 as 2 tapes. Supercond Sci Technol. 2024;37(7):075017. doi: 10.1088/1361-6668/ad4f5d
[202] Meng Y, Sun Y, Xing XZ, et al. Anomalously small magnetic relaxation rate of Ca 10 (pt 3 as 8)(fe 2−x Pt x as 2) 5 superconductor. Supercond Sci Technol. 2023;36(8):085022. doi: 10.1088/1361-6668/ace21d
[203] Sato H, Hiramatsu H, Kamiya T, et al. Strain engineering at heterointerfaces: application to an iron pnictide superconductor, cobalt-doped BaFe2As2. ACS Appl Mater Interfaces. 2020;12(44):50096–50104. doi: 10.1021/acsami.0c12080
[204] Seo S, Noh H, Li N, et al. Artificially engineered nanostrain in FeSexTe1-x superconductor thin films for supercurrent enhancement. NPG Asia Mater. 2020;12(1):7. doi: 10.1038/s41427-019-0186-y
[205] Ishida S, Iyo A, Ogino H, et al. Unique defect structure and advantageous vortex pinning properties in superconducting CaKFe4As4. Npj Quantum Mater. 2019;4(1):27. doi: 10.1038/s41535-019-0165-0
[206] Kogan VG, Prozorov R. Disorder-dependent slopes of the upper critical field in nodal and nodeless superconductors. Phys Rev B. 2023;108(6):064502. doi: 10.1103/PhysRevB.108.064502
[207] Guo ZM, Muraoka K, Gao HY, et al. Planar defects and strain distributions in polycrystalline BaFe2As2 superconductors synthesized by mechanochemical methods. Acta Materialia. 2024;266:119648. doi: 10.1016/j.actamat.2024.119648
[208] Ozaki T, Jaroszynski J, Li Q. Two-fold reduction of *J c anisotropy in FeSe 0.5 Te 0.5 films using low-energy proton irradiation*. IEEE Trans Appl Supercond. 2019;29(5):1–3. doi: 10.1109/tasc.2019.2900615
[209] Haberkorn N, Xu M, Meier WR, et al. Enhancement of critical current density in CaKFe4As4 single crystals through 3 MeV proton irradiation. Supercond Sci Technol. 2020;33(2):025008. doi: 10.1088/1361-6668/ab5f4b

[210] Ding HW, Zhao H, Huang PC, et al. Development of the first tesla class iron-based superconducting coil for high field application. Supercond Sci Technol. 2023;36(11):11lt01. doi: 10.1088/1361-6668/acfa29
[211] Li CY, Zhou J, Zhu YC, et al. Development of metal-insulated iron-based superconducting coils and charging tests under high magnetic fields up to 32 T. Supercond Sci Technol. 2024;37(1):015001. doi: 10.1088/1361-6668/ad0b95
[212] Yazdani-Asrami M. Artificial intelligence, machine learning, deep learning, and big data techniques for the advancements of superconducting technology: a road to smarter and intelligent superconductivity. Supercond Sci Technol. 2023;36(8):084001. doi: 10.1088/1361-6668/ace385
[213] Taheri A, Ebrahimnezhad H, Sedaaghi MH. Prediction of the critical temperature of superconducting materials using image regression and ensemble deep learning. Mater Today Commun. 2022;33:104743. doi: 10.1016/j.mtcomm.2022.104743
[214] Song JN, Xu ZT, Xiong XM, et al. Critical role played by interface engineering in weakening thickness dependence of superconducting and structural properties of FeSe0.5Te0.5-coated conductors. ACS Appl Mater Interfaces. 2023;15(21):26215–26224. doi: 10.1021/acsami.3c04531
[215] Ishii A, Kikuchi S, Yamanaka A, et al. Application of Bayesian optimization to the synthesis process of BaFe2(As,P)2 polycrystalline bulk superconducting materials. J Alloys And Compd. 2023;966:171613. doi: 10.1016/j.jallcom.2023.171613
[216] Hässler W, Hermann H, Herrmann M, et al. Influence of the milling energy transferred to the precursor powder on the microstructure and the superconducting properties of MgB2 wires. Supercond Sci Technol. 2013;26(2):025005. doi: 10.1088/0953-2048/26/2/025005
[217] Sugino S, Yamamoto A, Shimoyama J-I, et al. Enhanced trapped field in MgB2 bulk magnets by tuning grain boundary pinning through milling. Supercond Sci Technol. 2015;28(5):055016. doi: 10.1088/0953-2048/28/5/055016
[218] Prozorov R, Kogan VG, Konczykowski M, et al. Slope of the upper critical field at T c in two-band superconductors with nonmagnetic disorder: s + + superconductivity in Ba 1 − x K x Fe 2 as 2. Phys Rev B. 2024;109(2):024506. doi: 10.1103/PhysRevB.109.024506
[219] Grasso S, Sakka Y, Maizza G. Electric current activated/assisted sintering (ECAS): a review of patents 1906–2008. Sci Technol Adv Mater. 2009;10(5):053001. doi: 10.1088/1468-6996/10/5/053001
[220] Guillon O, Gonzalez-Julian J, Dargatz B, et al. Field-assisted sintering technology/spark plasma sintering: mechanisms, materials, and technology developments. Adv Eng Mater. 2014;16(7):830–849. doi: 10.1002/adem.201300409
[221] Kursumovic A, Durrell JH, Chen SK, et al. Ambient/Low pressure synthesis and fast densification to achieve 55 K Tc superconductivity in NdFeAsO0.75F0.25. Supercond Sci Technol. 2010;23(2):025022. doi: 10.1088/0953-2048/23/2/025022
[222] Puneet P, Podila R, He J, et al. Synthesis and superconductivity in spark plasma sintered pristine and graphene-doped FeSe0.5Te0.5. Nanotechnol Rev. 2015;4(5):411–417. doi: 10.1515/ntrev-2015-0018
[223] Zaikina JV, Kwong MY, Baccam B, et al. Superconductor-in-an-hour: spark plasma synthesis of Co- and Ni-doped BaFe2As2. Chem Mater. 2018;30(24):8883–8890. doi: 10.1021/acs.chemmater.8b04039
[224] Yetter WE, Thomas DA, Kramer EJ. Grain-boundary flux pinning by the electron-scattering mechanism. Philos Mag B. 1982;46(5):523–537. doi: 10.1080/01418638208224026
[225] Yamamoto A, Shimoyama J-I, Kishio K, et al. Limiting factors of normal-state conductivity in superconducting MgB2: an application of mean-field theory for a site percolation problem. Supercond Sci Technol. 2007;20(7):658–666. doi: 10.1088/0953-2048/20/7/012
[226] Matsushita T, Kiuchi M, Yamamoto A, et al. Essential factors for the critical current density in superconducting MgB2: connectivity and flux pinning by grain boundaries. Supercond Sci Technol. 2008;21(1):015008. doi: 10.1088/0953-2048/21/01/015008
[227] Obara T, Yamamoto A. Quantitative analysis of meandering and dimensional crossover of conduction path in 3D disordered media by percolation modeling. Supercond Sci Technol. 2020;33(7):074004. doi: 10.1088/1361-6668/ab8ffc
[228] Eisterer M. Predicting critical currents in grain-boundary limited superconductors. Phys Rev B. 2019;99(9):094501. doi: 10.1103/PhysRevB.99.094501
[229] Dimos D, Chaudhari P, Mannhart J, et al. Orientation dependence of grain-boundary critical currents in Y Ba 2 Cu 3 O 7 − δ bicrystals. Phys Rev Lett. 1988;61(2):219–222. doi: 10.1103/PhysRevLett.61.219
[230] Shimada Y, Yamamoto A, Hayashi Y, et al. The formation of defects and their influence on inter- and intra-granular current in sintered polycrystalline 122 phase Fe-based superconductors. Supercond Sci Technol. 2019;32(8):084003. doi: 10.1088/1361-6668/ab0eb6
[231] Guo ZM, Gao HY, Kondo K, et al. Nanoscale texture and microstructure in a NdFeAs(O,F)/IBAD-MgO superconducting thin film with superior critical current properties. ACS Appl Electron Mater. 2021;3(7):3158–3166. doi: 10.1021/acsaelm.1c00364
[232] Dong C, Han M, Guo W, et al. Modulation of superconducting grain structure to achieve high critical current in Ba0.6K0.4Fe2As2 multifilament round wires. J Alloys And Compd. 2023;932:167674. doi: 10.1016/j.jallcom.2022.167674
[233] Tu C, Dong C, Fu C, et al. Origin and elimination of excess iron particles in off-stoichiometric Ba0.6K0.5-βFe2As2+δ superconductors. Scr Materialia. 2023;235:115595. doi: 10.1016/j.scriptamat.2023.115595
[234] Chen Y, Li W, Liu C, et al. Effects of precursor powder particle size on the powder-in-tube Ba1−xKxFe2As2 superconducting tapes. Supercond Sci Technol. 2022;35(5):055008. doi: 10.1088/1361-6668/ac5aa7
[235] Togano K, Gao Z, Matsumoto A, et al. Enhancement in transport critical current density of ex situ PIT Ag/(Ba, K)Fe2As2 tapes achieved by applying a combined process of flat rolling and uniaxial pressing. Supercond Sci Technol. 2013;26(11):115007. doi: 10.1088/0953-2048/26/11/115007
[236] Spruit RG, van Omme JT, Ghatkesar MK, et al. A review on development and optimization of

microheaters for high-temperature *in situ studies*. J Microelectromech Syst. 2017;26(6):1165–1182. doi: 10.1109/JMEMS.2017.2757402
[237] Skorikov A, Albrecht W, Bladt E, et al. Quantitative 3D characterization of elemental diffusion dynamics in individual Ag@Au nanoparticles with different shapes. ACS Nano. 2019;13(11):13421–13429. doi: 10.1021/acsnano.9b06848
[238] Kamo K, Horii N, Furukawa H, et al. B11-P-14 ISER, a new, compressed sensing based reconstruction algorithm for reducing image acquisition time. Microscopy (Tokyo). 2015;64(suppl 1):i84.2–i84. doi: 10.1093/jmicro/dfv218
[239] Mäkinen Y, Azzari L, Foi A. Collaborative filtering of correlated noise: exact transform-domain variance for improved shrinkage and patch matching. IEEE Trans On Image Process. 2020;29:8339–8354. doi: 10.1109/TIP.2020.3014721
[240] Baba N, Hata S, Saito H, et al. Three-dimensional electron tomography and recent expansion of its applications in materials science. Microscopy. 2022;72(2):111–134. doi: 10.1093/jmicro/dfac071
[241] Müller S, Sauter C, Shunmugasundaram R, et al. Deep learning-based segmentation of lithium-ion battery microstructures enhanced by artificially generated electrodes. Nat Commun. 2021;12(1):6205. doi: 10.1038/s41467-021-26480-9
[242] Bagni T, Bovone G, Rack A, et al. Machine learning applied to X-ray tomography as a new tool to analyze the voids in RRP Nb3Sn wires. Sci Rep. 2021;11(1):7767. doi: 10.1038/s41598-021-87475-6
[243] Midgley PA, Weyland M. 3D electron microscopy in the physical sciences: the development of Z-contrast and EFTEM tomography. Ultramicroscopy. 2003;96(3–4):413–431. doi: 10.1016/S0304-3991(03)00105-0
[244] Huang Y, Perlmutter D, Su AFH, et al. Detecting lithium plating dynamics in a solid-state battery with operando X-ray computed tomography using machine learning. Npj Comput Mater. 2023;9(1):93. doi: 10.1038/s41524-023-01039-y
[245] Hagita K, Higuchi T, Jinnai H. Super-resolution for asymmetric resolution of FIB-SEM 3D imaging using AI with deep learning. Sci Rep. 2018;8(1):5877. doi: 10.1038/s41598-018-24330-1
[246] Togano K, Hur JM, Matsumoto A, et al. Fabrication of seven-core multi-filamentary MgB2 wires with high critical current density by an internal Mg diffusion process. Supercond Sci Technol. 2009;22(1):015003. doi: 10.1088/0953-2048/22/1/015003
[247] Ueda S, Shimoyama J, Iwayama I, et al. High critical current properties of MgB2 bulks prepared by a diffusion method. Appl Phys Lett. 2005;86(22):222502. doi: 10.1063/1.1939071
[248] Dancer CEJ, Prabhakaran D, Başoğlu M, et al. Fabrication and properties of dense ex situ magnesium diboride bulk material synthesized using spark plasma sintering. Supercond Sci Technol. 2009;22(9):095003. doi: 10.1088/0953-2048/22/9/095003
[249] Durrell JH, Dancer CEJ, Dennis A, et al. A trapped field of > 3 T in bulk MgB2 fabricated by uniaxial hot pressing. Supercond Sci Technol. 2012;25(11):112002. doi: 10.1088/0953-2048/25/11/112002
[250] Steinbach I. Phase-field model for microstructure evolution at the mesoscopic scale. Annu. Rev. Mater. Res. 2013;43:89–107. doi: 10.1146/annurev-matsci-071312-121703
[251] Wang YU. Computer modeling and simulation of solid-state sintering: a phase field approach. Acta Materialia. 2006;54(4):953–961. doi: 10.1016/j.actamat.2005.10.032
[252] Biswas S, Schwen D, Tomar V. Implementation of a phase field model for simulating evolution of two powder particles representing microstructural changes during sintering. J Mater Sci. 2018;53(8):5799–5825. doi: 10.1007/s10853-017-1846-3
[253] Biswas S, Schwen D, Wang H, et al. Phase field modeling of sintering: role of grain orientation and anisotropic properties. Comput Mater Sci. 2018;148:307–319. doi: 10.1016/j.commatsci.2018.02.057
[254] Sasaki K, Yamanaka A, Ito S, et al. Data assimilation for phase-field models based on the ensemble Kalman filter. Comput Mater Sci. 2018;141:141–152. doi: 10.1016/j.commatsci.2017.09.025
[255] Yamanaka A, Maeda Y, Sasaki K. Ensemble Kalman filter-based data assimilation for three-dimensional multi-phase-field model: estimation of anisotropic grain boundary properties. Mater & Des. 2019;165:107577. doi: 10.1016/j.matdes.2018.107577
[256] Ishii A, Yamanaka A, Miyoshi E, et al. Estimation of solid-state sintering and material parameters using phase-field modeling and ensemble four-dimensional variational method. Modell Simul Mater Sci Eng. 2021;29(6):065012. doi: 10.1088/1361-651X/ac13cd
[257] Ishii A, Yamanaka A, Miyoshi E, et al. Efficient estimation of material parameters using DMC-BO: application to phase-field simulation of solid-state sintering. Mater Today Commun. 2022;30:103089. doi: 10.1016/j.mtcomm.2021.103089
[258] Ishii A, Yamamoto A, Yamanaka A. DMC-TPE: tree-structured parzen estimator-based efficient data assimilation method for phase-field simulation of solid-state sintering. Sci Technol Of Adv Mater: Methods. 2023;3(1):2239133. doi: 10.1080/27660400.2023.2239133
[259] Rabier F, Järvinen H, Klinker E, et al. The ECMWF operational implementation of four-dimensional variational assimilation. I: experimental results with simplified physics. Quart J R Meteoro Soc. 2000;126(564):1143–1170. doi: 10.1002/qj.49712656415
[260] Tsuyuki T, Miyoshi T. Recent progress of data assimilation methods in meteorology. J Meteorolog Soc Of Jpn. 2007;85B(8):331–361. doi: 10.2151/jmsj.85B.331
[261] Kamiya H, Gotoh K, Shimada M. Characteristics and behavior of nanoparticles and its dispersion systems. In: KN MH, Naito M Yokoyama T, editors. Nanoparticle technology handbook. second ed. Amsterdam: Elsevier Science; 2012;113–176. doi: 10.1016/B978-044453122-3.50006-4
[262] Surholt T, Herzig C. Grain boundary self-diffusion in Cu polycrystals of different purity. Acta Mater. 1997;45(9):3817–3823. doi: 10.1016/s1359-6454(97)00037-2
[263] Bowden HG, Balluffi RW. Measurements of self-diffusion coefficients in copper from the annealing of voids. The Phil Mag: A J Theor Exp And Appl Phys. 1969;19(161):1001–1014. doi: 10.1080/14786436908225865
[264] Ishii A, Kondo K, Yamamoto A, et al. Phase-field modeling of solid-state sintering with interfacial anisotropy. Mater Today Commun. 2023;35:106061. doi: 10.1016/j.mtcomm.2023.106061
[265] Moelans N, Blanpain B, Wollants P. Quantitative analysis of grain boundary properties in

a generalized phase field model for grain growth in anisotropic systems. Phys Rev B. 2008;78(2):024113. doi: 10.1103/PhysRevB.78.024113
[266] Read WT, Shockley W. Dislocation models of crystal grain boundaries. Phys Rev. 1950;78(3):275–289. doi: 10.1103/PhysRev.78.275
[267] Tran R, Xu Z, Radhakrishnan B, et al. Surface energies of elemental crystals. Sci Data. 2016;3(1):160080. doi: 10.1038/sdata.2016.80
[268] Lee JY, Punkkinen MPJ, Schönecker S, et al. The surface energy and stress of metals. Surf Sci. 2018;674:51–68. doi: 10.1016/j.susc.2018.03.008
[269] Gao M, Ma F, Lu Z-Y, et al. Surface structures of ternary iron arsenides AFe2As2 (A=ba, Sr, or Ca). Phys Rev B. 2010;81(19):193409. doi: 10.1103/PhysRevB.81.193409
[270] Heifets E, Eglitis RI, Kotomin EA, et al. Ab initio modeling of surface structure for SrTiO3 perovskite crystals. Phys Rev B. 2001;64(23):235417. doi: 10.1103/PhysRevB.64.235417
[271] Piskunov S, Kotomin EA, Heifets E, et al. Hybrid DFT calculations of the atomic and electronic structure for ABO3 perovskite (001) surfaces. Surf Sci. 2005;575(1–2):75–88. doi: 10.1016/j.susc.2004.11.008
[272] Wang Y, Zhang Z, Wang Y, et al. First-principles investigation of structural, electronic, and energetic properties of BaSnO3 (001) surfaces. Vacuum. 2023;212:111977. doi: 10.1016/j.vacuum.2023.111977
[273] Nascimento VB, Li A, Jayasundara DR, et al. Surface geometric and electronic structures of BaFe2As2 (001). Phys Rev Lett. 2009;103(7):076104. doi: 10.1103/PhysRevLett.103.076104
[274] Rotter M, Tegel M, Johrendt D, et al. Spin-density-wave anomaly at 140 K in the ternary iron arsenide BaFe2As2. Phys Rev B. 2008;78(2):020503. doi: 10.1103/PhysRevB.78.020503
[275] Stanev V, Oses C, Kusne AG, et al. Machine learning modeling of superconducting critical temperature. Npj Comput Mater. 2018;4(1):29. doi: 10.1038/s41524-018-0085-8
[276] Matsumoto K, Horide T. An acceleration search method of higher Tc superconductors by a machine learning algorithm. Appl Phys Express. 2019;12(7):073003. doi: 10.7567/1882-0786/ab2922
[277] Liu Z-L, Kang P, Zhu Y, et al. Material informatics for layered high-Tc superconductors. APL Mater. 2020;8(6):061104. doi: 10.1063/5.0004641
[278] Konno T, Kurokawa H, Nabeshima F, et al. Deep learning model for finding new superconductors. Phys Rev B. 2021;103(1):014509. doi: 10.1103/PhysRevB.103.014509
[279] Zhang JZ, Zhu ZX, Xiang XD, et al. Machine learning prediction of superconducting critical temperature through the structural descriptor. J Phys Chem C. 2022;126(20):8922–8927. doi: 10.1021/acs.jpcc.2c01904
[280] Lee D, You D, Lee D, et al. Machine-learning-guided prediction models of critical temperature of cuprates. J Phys Chem Lett. 2021;12(26):6211–6217. doi: 10.1021/acs.jpclett.1c01442
[281] Zhong C, Zhang J, Lu X, et al. Deep generative model for inverse design of high-temperature superconductor compositions with predicted Tc > 77 K. ACS Appl Mater Interfaces. 2023;15(25):30029–30038. doi: 10.1021/acsami.3c00593
[282] Ido K, Motoyama Y, Yoshimi K, et al. Data analysis of ab initio effective hamiltonians in iron-based superconductors — construction of predictors for superconducting critical temperature. J Phys Soc Jpn. 2023;92(6):064702. doi: 10.7566/jpsj.92.064702
[283] Metni H, Takeuchi I, Stanev V. Predicting the superconducting critical temperature in transition metal carbides and nitrides using machine learning. Physica C: Supercond Appl. 2023;605:1354209. doi: 10.1016/j.physc.2023.1354209
[284] Al-Ruqaishi Z, Ooi CHR. Multilayer neural network models for critical temperature of cuprate superconductors. Comput Mater Sci. 2024;241:113018. doi: 10.1016/j.commatsci.2024.113018
[285] Liang Q, Gongora AE, Ren Z, et al. Benchmarking the performance of Bayesian optimization across multiple experimental materials science domains. Npj Comput Mater. 2021;7(1):188. doi: 10.1038/s41524-021-00656-9
[286] Matera D, Bonura M, Černý R, et al. High-field superconductivity in C-doped MgB2 bulk samples prepared by a rapid synthesis route. Sci Rep. 2020;10(1):17656. doi: 10.1038/s41598-020-74300-9
[287] Jain A, Ong SP, Hautier G, et al. Commentary: the materials project: a materials genome approach to accelerating materials innovation. APL Mater. 2013;1(1):011002. doi: 10.1063/1.4812323
[288] Materials Database Group, National Institute for Materials Science. The superconducting material database (SuperCon). 2022. doi: 10.48505/nims.3739
[289] Katsura Y, Kumagai M, Kodani T, et al. Data-driven analysis of electron relaxation times in PbTe-type thermoelectric materials. Sci Technol Adv Mater. 2019;20(1):511–520. doi: 10.1080/14686996.2019.1603885
[290] Court CJ, Cole JM. Magnetic and superconducting phase diagrams and transition temperatures predicted using text mining and machine learning. Npj Comput Mater. 2020;6(1):18. doi: 10.1038/s41524-020-0287-8
[291] Foppiano L, Dieb S, Suzuki A, et al. SuperMat: construction of a linked annotated dataset from superconductors-related publications. Sci Technol Of Adv Mater: Methods. 2021;1(1):34–44. doi: 10.1080/27660400.2021.1918396
[292] Rasmussen CE, Williams CKI. Gaussian processes for machine learning. Cambridge, Massachusetts: The MIT Press; 2005.
[293] Shahriari B, Swersky K, Wang ZY, et al. Taking the human out of the loop: a review of bayesian optimization. Proc IEEE. 2016;104(1):148–175. doi: 10.1109/jproc.2015.2494218
[294] Hatano T, Iida DQ, Gao Z, et al. High tolerance of the superconducting current to large grain boundary angles in potassium-doped BaFe2As2. NPG Asia Mater. 2024;in press;16(1). doi: 10.1038/s41427-024-00561-9
[295] Durrell JH, Dennis AR, Jaroszynski J, et al. A trapped field of 17.6T in melt-processed, bulk Gd-ba-cu-O reinforced with shrink-fit steel. Supercond Sci Technol. 2014;27(8):082001. doi: 10.1088/0953-2048/27/8/082001
[296] Cui YL, Yang WM. Enhanced performance of GdBCO bulk superconductors by doping a new kind of YGdBa4CuNbOy nanoparticles. Supercond Sci Technol. 2024;37(3):035002. doi: 10.1088/1361-6668/ad1e32
[297] Baumann J, Shi YH, Dennis AR, et al. The influence of porosity on the superconducting properties of Y–

ba–cu–O single grains. Supercond Sci Technol. 2023;36(8):085020. doi: 10.1088/1361-6668/ace480
[298] Huang CG, Song ZY, Wang SZ, et al. Thermomagnetic instability and accompanied stress intensity factor jumps in type-ii superconducting bulks under various magnetization processes. Supercond Sci Technol. 2023;36(1):015008. doi: 10.1088/1361-6668/aca62e
[299] Tutt N, Congreve J, Shi Y, et al. Fabrication of high-quality joints between Gd-Ba-Cu-O bulk superconductors. Supercond Sci Technol. 2023;36(8):085004. doi: 10.1088/1361-6668/acdc5c
[300] Congreve JVJ, Shi Y, Tutt NC,et al. A route to fabricate low resistance joints between Eu-Ba-Cu-O bulk, single grain superconductors. Supercond Sci Technol. 2024;37(6):065019. doi: 10.1088/1361-6668/ad44ea
[301] Abulaiti A, Wan-Min Y. A novel interior seed addition to improve the levitation force and the trapped field of multi-seeded YBCO bulk superconductors. Supercond Sci Technol. 2023;36(11):115010. doi: 10.1088/1361-6668/acf88c
[302] Shi YH, Ainslie MD, Dennis AR, et al. Optimisation of stacked, bulk high temperature superconductors for trapped-field magnet applications. Supercond Sci Technol. 2023;36(8):085018. doi: 10.1088/1361-6668/ace2ef
[303] Abulaiti A, Yang WM, Wu TT, et al. The effect of pre-sintering and high-temperature infiltration on the properties of single-domain YBCO bulk superconductors by the Y+011 top-seeded infiltration growth process. Supercond Sci Technol. 2023;36(2):025005. doi: 10.1088/1361-6668/acaa65
[304] Wang YC, Ainslie MD, Zhou DF, et al. Pulsed field magnetization of a rectangular Y-Ba-Cu-O bulk, single grain superconductor assembly. Supercond Sci Technol. 2023;36(7):075006. doi: 10.1088/1361-6668/acd421
[305] Cientanni V, Ainslie MD. Modelling and mitigating flux jumps in bulk high-temperature superconductors during quasi-static, high-field magnetisation. Supercond Sci Technol. 2023;36(2):025007. doi: 10.1088/1361-6668/acaa06
[306] Hu JT, Yang WJ, Zhou DF, et al. Analysis of critical current inhomogeneity in r–z plane of GdBCO superconducting bulk and simulation of flux jumps during pulsed field magnetization. Supercond Sci Technol. 2023;36(5):055004. doi: 10.1088/1361-6668/acbe72
[307] Houbart M, Fagnard JF, Dular J, et al. How to overcome the demagnetization of superconducting Halbach arrays? Supercond Sci Technol. 2023;36(11):115012. doi: 10.1088/1361-6668/acf904
[308] Hahn S, Voccio J, Park DK, et al. A stack of YBCO annuli, thin plate and bulk, for micro-nmr spectroscopy. IEEE Trans Appl Supercond. 2012;22(3):4302204. doi: 10.1109/tasc.2011.2178969
[309] Suyama M, Pyon S, Iijima Y, et al. Trapping a magnetic field of 17.89 T in stacked coated conductors by suppression of flux jumps. Supercond Sci Technol. 2022;35(2):02lt01. doi: 10.1088/1361-6668/ac4560
[310] Patel A, Hopkins SC, Glowacki BA. Trapped fields up to 2 T in a 12 mm square stack of commercial superconducting tape using pulsed field magnetization. Supercond Sci Technol. 2013;26(3):032001. doi: 10.1088/0953-2048/26/3/032001
[311] Patel A, Filar K, Nizhankovskii VI, et al. Trapped fields greater than 7 T in a 12 mm square stack of commercial high-temperature superconducting tape. Appl Phys Lett. 2013;102(10):102601. doi: 10.1063/1.4795016
[312] Yamamoto A, Ishihara A, Tomita M, et al. Permanent magnet with MgB2 bulk superconductor. Appl Phys Lett. 2014;105(3):032601. doi: 10.1063/1.4890724
[313] Noudem JG, Aburras M, Bernstein P, et al. Development in processing of MgB2 cryo-magnet superconductors. J Appl Phys. 2014;116(16):163916. doi: 10.1063/1.4900725
[314] Naito T, Sasaki T, Fujishiro H. Trapped magnetic field and vortex pinning properties of MgB2 superconducting bulk fabricated by a capsule method. Supercond Sci Technol. 2012;25(9):095012. doi: 10.1088/0953-2048/25/9/095012
[315] Giunchi G. Superconductive inserts: products between bulks and wires. IEEE Trans Appl Supercond. 2011;21(3):1564–1567. doi: 10.1109/tasc.2010.2092739
[316] Bhagurkar AG, Yamamoto A, Babu NH, et al. Synthesis of dense bulk MgB2 by an infiltration and growth process. Supercond Sci Technol. 2015;28(1):015012. doi: 10.1088/0953-2048/28/1/015012
[317] Gao ZL, Grovenor CRM, Speller SC. Correlation between microstructure and superconducting properties of MgB2 bulk samples with Mg addition and Mg/hBN co-additions. Supercond Sci Technol. 2023;36(9):094001. doi: 10.1088/1361-6668/ace662
[318] Xing Y, Bernstein P, Muralidhar M, et al. Overview of spark plasma synthesis and sintering of MgB2 superconductor. Supercond Sci Technol. 2023;36(11):115005. doi: 10.1088/1361-6668/acf738
[319] Da Silva LBS, Serquis A, Hellstrom EE, et al. The effect of AlB2 addition on MgB2 superconducting bulks. Supercond Sci Technol. 2023;36(4):045013. doi: 10.1088/1361-6668/acbe22
[320] Cui GG, Cai Q, Li YM, et al. Confinement of self-generated Mg(BH4)2 particles for simultaneously enhanced flux pinning and grain connectivity in polycrystalline H-doped MgB2. Supercond Sci Technol. 2023;36(3):035002. doi: 10.1088/1361-6668/acb2fb
[321] Aldica G, Burdusel M, Badica P. Trapped magnetic field in a (NdFeB)–(MgB2) pair-type bulk magnet. Physica C: Supercond Appl. 2014;505:18–23. doi: 10.1016/j.physc.2014.07.001
[322] Xing YT, Russo G, Ribani PL, et al. Very strong levitation force and stability achieved with a large MgB2 superconductor disc. Supercond Sci Technol. 2024;37(2):02lt01. doi: 10.1088/1361-6668/ad1aea
[323] Fracasso M, Gömöry F, Solovyov M, et al. Numerical study on flux-jump occurrence in a cup-shaped MgB2 bulk for magnetic shielding applications. Supercond Sci Technol. 2023;36(4):044001. doi: 10.1088/1361-6668/acbac5
[324] Fujishiro H, Tamura T, Arayashiki T, et al. Pulsed field magnetization of large MgB2 bulk fabricated by reactive liquid Mg infiltration. Jpn J Appl Phys. 2012;51(10R):103005. doi: 10.1143/jjap.51.103005
[325] Ainslie MD, Yamamoto A. Thickness dependence of trapped magnetic fields in machined bulk MgB2 superconductors. IEEE Trans Appl Supercond. 2022;32(4):1–4. doi: 10.1109/tasc.2022.3147140
[326] Ikeda N, Ainslie M, Tanaka R, et al. A comparative study of experimental and simulated trapped magnetic field of MgB2 bulks prepared by the magnesium vapor transport process. IEEE trans appl supercond. 2023;33(5):1–5. doi: 10.1109/tasc.2023.3253070
[327] Zou J, Ainslie MD, Fujishiro H, et al. Numerical modelling and comparison of MgB2 bulks fabricated by HIP and infiltration growth. Supercond Sci Technol. 2015;28(7):075009. doi: 10.1088/0953-2048/28/7/075009

[328] Ainslie MD, Yamamoto A, Fujishiro H, et al. Numerical modelling of iron-pnictide bulk superconductor magnetization. Supercond Sci Technol. 2017;30(10):105009. doi: 10.1088/1361-6668/aa841f
[329] Wang DL, Zhang Z, Zhang XP, et al. First performance test of a 30mm iron-based superconductor single pancake coil under a 24T background field. Supercond Sci Technol. 2019;32(4):04lt01. doi: 10.1088/1361-6668/ab09a4
[330] Zhang Y. Successful development of an iron-based coated conductor magnet. Supercond Sci Technol. 2024;37(4):040501. doi: 10.1088/1361-6668/ad2e10
[331] Pyon S, Mori H, Tamegai T, et al. Fabrication of small superconducting coils using (Ba,A)Fe2As2 (A: Na, K) round wires with large critical current densities. Supercond Sci Technol. 2021;34(10):105008. doi: 10.1088/1361-6668/ac0cca
[332] Tamegai T. Iron-based superconductors have joined the practical high-field magnet family. Supercond Sci Technol. 2024;37(1):010501. doi: 10.1088/1361-6668/ad09e8
[333] Hu Z, Dhaka MS. Fe-based superconducting transition temperature modeling by machine learning: a computer science method. PLOS ONE. 2021;16(8):e0255823. doi: 10.1371/journal.pone.0255823
[334] Gashmard H, Shakeripour H, Alaei M. Predicting superconducting transition temperature through advanced machine learning and innovative feature engineering. Sci Rep. 2024;14(1):3965. doi: 10.1038/s41598-024-54440-y
[335] Bai Z, Bhullar M, Akinpelu A, et al. Unveiling future superconductors through machine learning. Mater Today Phys. 2024;43:101384. doi: 10.1016/j.mtphys.2024.101384
[336] Jung SG, Jung G, Cole JM. Machine-learning predictions of critical temperatures from chemical compositions of superconductors. J Chem Inf Model. 2024;64(19):7349–7375. doi: 10.1021/acs.jcim.4c01137
[337] Díaz Carral Á, Roitegui M, Fyta M. Interpretably learning the critical temperature of superconductors: electron concentration and feature dimensionality reduction. APL Mater. 2024;12(4). doi: 10.1063/5.0189714
[338] Guo Y, Miao H, Zou Q, et al. Towards revealing intrinsic vortex-core states in Fe-based superconductors through statistical discovery. 2D Mater. 2024;11(4):045004. doi: 10.1088/2053-1583/ad5e92
[339] Oli BD, Zou Q, Li X, et al. Atomic-scale electronic inhomogeneity in single-layer iron chalcogenide alloys revealed by machine learning of STM/S data. AIP Adv. 2023;13(10):105224. doi: 10.1063/5.0156695